UNIVERSITÀ DEGLI STUDI DI CATANIA
Scuola Superiore di Catania
Dipartimento di Fisica e Astronomia
International PhD in Nuclear and Particle Astrophysics

Giovanni Luca Guardo

Initial state fluctuations and anisotropic flows of the Quark-Gluon Plasma created in ultra-relativistic heavy-ion collisions

Ph.D. Thesis

Ph.D. Coordinator:
Chiar.mo Prof. Stefano Romano

Tutor:
Chiar.mo Prof. Vincenzo Greco
Dott. Salvatore Plumari
Dott. Marco Ruggieri

Ciclo XXVII 2011/2014

If the facts don't fit the theory, change the facts.

A. Einstein

I am now convinced that theoretical physics is actually philosophy.

M. Born

CONTENTS

ABSTRACT

The fundamental theory of strong interactions is the so called Quantum Chromo Dynamics (QCD) that is a quantum field theory with an extremely rich dynamical content. The main features of this theory are the asymptotic freedom and confinement. The study of QCD, under extreme conditions of temperature and density has been one of the most difficult problem in physics during the last decades, capturing increasing experimental and theoretical attention also in connection with its relation to the Early Universe physics.

In this work of thesis it is extensively discussed the effect of the primordial QCD phase transition during the first part of the evolution of our Universe: the Big Bang nucleosynthesis.

On the other hand, the Relativistic Heavy Ion Collider (RHIC) and Large Hadron Collider (LHC) programs have been used to probe the properties of nuclear matter under such extreme condition. In the light of the experimental results accumulated in these years in these ultra relativistic heavy ion collisions, the main purpose of this thesis is to study the dynamical evolution of the Quark Gluon Plasma (QGP) in the framework of kinetic theory.

In particular, recent experimental data show that the momentum anisotropy

of the emitted particles is an observable that encodes information about the transport properties of the matter created in these HIC and also that it is an observable sensitive to the shear viscosity to entropy density ratio η/s. Hence, in this work we have investigated within an event-by-event transport approach at fixed viscosity this elliptic flow v_2 and high order harmonics v_n.

The principal results presented in this thesis concern the different sensitivity to the $\eta/s(T)$ at different energies (RHIC and LHC) for both ultra-central and mid-peripheral collisions, especially in the cross over region of the transition. Moreover we highlighted the effect of the inclusion in our simulation code of a realistic kinetic freeze out. Finally, we discussed the correlation between the initial spatial anisotropies ϵ_n and flow coefficients v_n.

INTRODUCTION

Within the framework of Standard Model, the fundamental theory that governs the dynamics of strongly interacting particles is the Quantum Chromodynamics (QCD). The degrees of freedom of such a theory are quarks and gluons which play the role of intermediary of the interaction. QCD is formulated as a gauge theory analogously with Quantum Electrodynamics (QED).

However the different symmetries owned by the strong interaction with respect to electromagnetic interaction implies that QCD is a non abelian gauge theory with properties quite different from QED.

Moreover, this theory have two important and characterizing features, that are the colour confinement and the asymptotic freedom. The first one implies that quarks and gluons can only exist as confined objects inside hadrons. The second one is directly related to its non Abelian nature and consists in the decrease of interaction strength with the decreasing of interaction distance.

The asymtotic freedom opens the way to the possibility of studying the strong interaction in a perturbative regime for sufficiently high energy processes, and implies that under particular condition of temperature or density the strong interaction that confines quarks and gluons becomes

smaller enough to release them.

Hence a new state of matter can exist in which the colour charges are deconfined in a Quark Gluon Plasma (QGP), the predictions of Lattice Quantum Chromodynamics indicate that the critical temperature in which the nuclear matter experiences a phase transition is $T_C \approx 160\,MeV \approx 10^{12}\,K$.

This phase of the matter should have existed in the early stage of Universe life up to a time of about $10^{-5}\,sec$ after the Big Bang and in this work we also studied the role of this phase transition and its effect during the Big Bang Nucleosynthesis (BBN). More precisely in this thesis we present some novel results about the propagation of sound waves in the QGP of interest for evolution of the first stage of the Early Universe.

The studies of the matter under such extreme conditions can be done performing Heavy Ion Collisions (HIC) at ultrarelativistic energy (above $10\,AGeV$). Signatures of a Quark Gluon Plasma formation became manifest in the experiment with energies up to $200 AGeV$ performed at Relativistic Heavy Ion Collider (RHIC) at Brookhaven National Laboratory. Further confirmations as well as new discoveries have been coming from the experiments at Large Hadron Collider (LHC) started in 2010 where it is possible to reach energies up to $5.5 TeV$.

A clear understanding of the features of the Quark Gluon Plasma (QGP) created in such heavy ion collision is yet a theoretical challenge. This is due first of all to the complex nature of the Quantum Cromodynamics, expecially in the non-perturbative regime, that makes difficults to have a full understanding of the dynamics of partons which compose the QGP. However in the recent years a wide development of lattice QCD has occured allowing to have more and more knowledge about the thermodynamical properties of the matter at the high temperatures as those reached in ultra-relativistic heavy ion collision. In particular, we have a safe computation of the energy density and pressure of the Quark Gluon

Plasma and of the transition temperature from the QGP to the hadronic phase while it is becoming possible to compute in medium particle correlations and transport properties.
Secondly, but not less important, the observables experimentally accesible are hadrons and consequently the study of the partonic behaviour is partially veiled by the hadronization process that is yet not completely understood. Nevertheless there are a lot of observables that permit to identify the formation and the properties of the QGP. Such observables are influenced by the different phase of the evolution of the QGP, therefore it is important to identify observables that are able to probe one particular phase of the system without being influenced by the other phase. In this way it is possible to have information about a particular phase of the evolution.
One of the strongest pieces of evidence for the formation of the QGP in ultra-relativistic nucleus-nucleus collisions stems from the strong anisotropic collective flow which is a measure of the azimuthal asymmetry in momentum space. This is an observable that encodes information about the transport properties of the matter created in HIC and the equation of state and it is an observable sensitive to the shear viscosity to entropy density ratio η/s. Experimentally, the particle azimuthal distribution measured with respect to the so-called reaction plane is not isotropic. Moreover, the reaction plane cannot be directly measured in high energy nuclear collisions, but can be estimated from the azimuthal distribution event-by-event.
The presence of strong collective flow in the Quark Gluon Plasma emerging in the experiments of heavy ion collision have suggested that the evolution of QGP can be treated using hydrodynamics. This model do not need a detailed description of the microscopic dynamics since it deals with collective properties of the plasma.
Hydrodynamical models supplies a good description of the QGP observ-

abels in the low p_T region, there it is conceivable to have a local kinetic equilibrium as assumed by hydrodynamics. In particular it is able to correctly predict the experimental data relative to the elliptic flow v_2, a measure of the pressure and the viscosity of the created matter. However hydrodynamics fails to reproduce experimental data relative to v_2 and higher harmonics v_n in the intermediate and high p_T region. Moreover it is necessary to include viscosity effects which lead to the developments of a viscous hydrodynamics that has a limited range of validity in momentum space especially at increasing viscosity like the one that could be present in the cross-over region of transition or at very large temperatures.

The work presented in this thesis is based on a study of the dinamical evolution of the quark gluon plasma in the framework of kinetic theory. In such an approach the dynamical evolutions of the system is studied solving the equation of motion for the one-body phase space distribution $f(x, p)$, i.e. solving the Boltzmann-Vlasov equation. At variance with hydrodinamics this is a microscopic approach to study the dynamics of the system. Indeed, our model describes the dynamics of QGP considering both the collision term, that accounts for the short range interaction between partons, and the mean field, that instead accounts for the long range physics.

We have developed a numerical code to implement a solution of the relativistic Boltzmann equation for the parton distribution function tuned at a fixed shear viscosity to entropy density ratio η/s. This approach provides a tool to estimate the viscosity of the plasma valid in a wider range of η/s and p_T. Finally, in order to generate an initial profile that change event by event we use the Monte-Carlo Glauber model to obtain the initial density distribution for each event. In this way, we can study the initial collisional geometry fluctuations and investigate how they evolve through different stages of the fireball history and translate

into final particle momentum anisotropies.
First of all, in order to get stable results, we have tested the good sampling of the initial geometry. So we have checked the convergency of our model for v_2, v_3 and v_4 with the lattice spacing of the calculation grid and the total number of test particles N_{test}.
The main goal of the present thesis is therefore to study the build up of elliptic flow v_2 and high order harmonics v_n within a transport approach at fixed shear viscosity to entropy density ratio η/s and with initial state fluctuations. In particular we study the effect of a temperature dependent η/s for two different beam energies: RHIC for $Au+Au$ at $\sqrt{s} = 200\,GeV$ and LHC for $Pb+Pb$ at $\sqrt{s} = 2.76\,TeV$. We find that for the two different beam energies considered the suppression of the elliptic flow and of higher harmonics $v_3(p_T)$ and $v_4(p_T)$ due to the viscosity of the medium have different contributions coming from the cross over transition or QGP phase. Moreover, we discuss the correlation between the initial spatial anisotropies ϵ_n and flow coefficients v_n. We observe that the elliptic flow v_2 is strongly correlated with initial eccentricity ϵ_2. While higher harmonics v_3 and v_4 are weakly correlated to their asymmetry measure in coordinate space ϵ_3 and ϵ_4. However we pointed that at LHC energy for ultra-central collisions the correlation remains very high also for (v_4,ϵ_4) and also the sensitivity to $\eta/s(T)$ in significantly larger than in mid-peripheral collisions that have been more intensively studied till now.
The thesis is divided in five chapter:
In the first chapter we will present the general features and the peculiarity of Quantum CromoDynamics. Moreover the theoretical approaches that allow its study will be discussed. In addiction, an overview of our results about the conseguence of the QCD transition in the first stage of Early Universe it will be also presented. Finally at the end of the chapter the phase diagram of the nuclear matter will be described.
In chapter 2, we will give a primer of the ultra-relativistic heavy ion colli-

sions and the main probes and observables of the formation of the Quark Gluon Plasma. A particular attention will be alight on the anisotropic collective flows and their experimental operative definitions and results.
In chapter 3, we will introduce the numerical simulation code developed in this work based on an effective kinetic transport theory approach that permits to study a system evolving dynamically. In particular it will be discussed the solution of the relativistic Boltzmann equation. Finally at the end of this chapter will be described the implementation of a kinetic theory in which it is possible to fix the value fo the shear viscosity η/s.
In chapter 4, the potentiality of studying the initial collision geometry fluctuations and the final particle momentum anisotropies with a transport approach that change event by event will be analized. Moreover, we will show our test of convergency for v_n with the lattice spacing grid and total number of test particles.
Finally, in chapter 5, the results obtained perfoming simulations of the heavy ion collisions at RHIC and LHC will be shown and commented. In particular we will describe the effect of a temperature dependent shear viscosity to entropy density ratio in the evolution of anisotropic flow v_n. Moreover, we will investigate within our event-by-event transport approach the correlation between the initial spatial anisotropies ϵ_n and flow coefficients v_n.

CHAPTER 1

QUANTUM CHROMO DYNAMICS

Contents

In this chapter the main features of the Quark Gluon Plasma created in ultra-relativistic heavy ion collisions will be discussed with the purpose of contextualizing the work presented in this thesis. In the first part of the chapter a primer of the theory that describes the strong interaction

will be treated along with the theoretical approach that permit to deal with its non-perturbative aspects: lattice QCD (lQCD). The information collected from lQCD will be summarized showing the phase diagram of the strong interacting matter, which will lead to the second chapter in which it will be described the ultra-relativistic heavy ion collisions as the unique tool to probe such a phase diagram at high temperature.

1.1 Introduction to QCD

The modern physics aim is to describe the elementary building blocks of matter and the forces that rule on them. As we know, at the present moment the Standard Model is the most comprehensive physical theory ever developed, that has been experimentally tested with high accuracy [1]. In the Standard Model, gauge bosons are defined as force carriers that mediate the strong, weak, and electromagnetic fundamental interactions. The different type of gauge bosons, all with spin 1, are the *photons* γ that mediate the electromagnetic force, $W_{\uparrow}$, $W_{\downarrow}$, Z^0 that mediate weak interactions and *gluons* g that are the carriers of strong interaction between color charged particles.

The Standard Model includes 12 elementary particles of spin $\frac{1}{2}$, known as fermions. Each fermion has a corresponding antiparticle. The fermions of the Standard Model are classified according to how they interact (or equivalently, by what charges they carry).

There are six quarks (up, down, charm, strange, top, bottom), and six leptons (electron, electron neutrino, muon, muon neutrino, tau, tau neutrino). These particles are considered as point particles. All the other particles that have been discovered over the years, the hadrons, are composite particles consisting of three or two quarks, respectively. The quarks are fermions having not only the flavour degrees of freedom (up, down, strange, charm, bottom, top), but also color degrees of freedom (red, blue and green).

An isolated color has never been observed experimentally, which indicates that quarks are always bound together to form color-white composite objects. Baryons (proton, neutron, Λ, Σ,...) comprise three valence quarks, and mesons (π, ρ, K, J/Ψ, ...) comprise a quark-antiquark pair. They are the simplest color-white constructions of hadrons, but possible multiquark systems (like tetraquarks, pentaquarks and esaquarks) may exist and have been subject of increasing interest especially in the last decade.

The concept of color, as well as the quantum dynamics of color, was first proposed by Nambu [2] and this theory is now called "Quantum Chromodynamics" (QCD). This is a generalization of Quantum Electrodynamics (QED), which is a quantum theory of charged particles and the electromagnetic field. QCD (respectively QED) has gluons (the photon) as spin-1 gauge bosons that mediate the force between quarks (charged particles). Although QCD and QED look similar, there is a crucial difference: whereas the photon is electrically neutral and therefore transfers no charge, the gluons are not neutral in color. The fact that gluons themselves carry color is related to the fundamental concept of non-Abelian or Yang-Mills gauge theory [3]. The term "non Abelian" or "non commutative" is realized in the color SU(3) algebra in QCD but not in the U(1) algebra in QED, being the last an Abelian group.
QCD provides us with two important characteristics of quark-gluon dynamics. At high energies the interaction becomes small and quarks and gluons interact weakly which is called "asymptotic freedom" [4, 5], while at low energy the interaction becomes strong and leads to the confinement of color. The asymptotic freedom, which is a unique aspect of non-Abelian gauge theory, is related to the anti-screening of color charge. Because the gauge fields themselves have color, a bare color charge centered at the origin is diluited away in space by the gluons. Therefore, as one tries to find the bare charge by going through the cloud of gluons, one finds a smaller and smaller portion of the charge. This is in sharp contrast to the case of QED, where the screening of a bare charge takes place due to the cloud of, for example, electron-positron pairs surrounding the charge. As the typical length scale decreases, or the energy scale increases, the coupling strength decreases in QCD. This is why we can expect a QGP phase at high temperature, for which the typical thermal energies of the quark and gluons are large while the interactions become weak.

The interaction in QCD becomes stronger at long distances or at low energies. This is a signature of the confinement of color. Indeed, the phenomenological potential between a quark and an anti-quark at large separation increase linearly. Consequently, even if we try to separate the quark and the anti-quark beyond some critical distance the potential energy becomes large enough such that a new quark-antiquark pair pops up from the vacuum. Then, the original quark-antiquark pair becomes two pairs. In this way, quarks are always confined inside hadrons and can never be isolated in QCD.
Because the QCD coupling strength, α_S, becomes large at long distances, which means low energies, we encounter a technical difficulty: Λ_{QCD} defines a typical energy scale of the strong interaction and the coupling α_S perturbatively is $\propto \ln^{-1}\left(\frac{Q^*}{\Lambda_{QCD}}\right)$ and therefore the scale is about 250 GeV that correspond to a distance scale $r \approx 0.8\, fm$ which tell us that the physics of the scale of a proton size is infinitely non-perturbative, so that we can adopt a perturbative method only for $E \geq 10\Lambda_{QCD} \approx 2 - 3GeV$. Wilsons lattice gauge theory may be used to circumvent this problem [6]. It treats fourdimensional space-time not as a continuum, but as a lattice, just as in crystals, in which quarks occupy lattice points while the gauge field occupies lattice links. By this lattice discretization, one may solve QCD utilizing Monte Carlo numerical simulations. Results confirm that the potential energy is indeed proportional to the length of the string as well as that nuclear matter undergoes a transition at temperature $T \approx 200MeV$.

1.2 Classical QCD action

In order to better discuss how the different interactions between particle physics are treated in the standard model is useful to treat the theory that describes the electromagnetic interaction between particles, i.e the Quantum ElectroDynamics (QED) [7]. In fact it represent the prototype

of the modern description of the interaction.
One considers a simple physical system described by a free Dirac field Ψ, with the Lagrangian:

$$\mathcal{L} = \bar{\Psi}(x)(i\gamma^\mu \partial_\nu - m)\Psi(x) \tag{1.1}$$

where x are the space-time coordinates. Starting from this Lagrangian and making use of the Eulero-Lagrange equations one obtains the Dirac equation, which describes the dynamic of this simple system:

$$(i\gamma^\mu \partial_\nu - m)\Psi(x) = 0. \tag{1.2}$$

The Lagrangian 1.1 is invariant under global U(1) transformations, i.e. $\Psi \to e^{iQ\theta}\Psi$, but, if such transformation is promoted from global to local, $\Psi \to e^{iQ\theta(x)}\Psi$, the lagrangian is no more invariant. This means that a system of non interacting particles does not satisfy the U(1) gauge transformation. On the other hand we know that such a symmetry is owned by the electromagnetic interaction and already present in the Maxwell equations. In fact it is possible to show that if one modifies the Lagrangian 1.1 introducing the minimal interaction required to make it invariant under the local transformation, automatically arises the electromagnetic force between particles. One obtains, in this way, the correct equation of motion for charged particles interacting with an electromagnetic field.
This approach to derive the interaction is called gauge principle. In practice the interaction is introduced with one gauge vector boson field $A_\mu(x)$, which interacts with the fermionic field and transforms in such way to make the Lagrangian invariant under the U(1) gauge transformation. Usually the way to build this gauge invariant Lagrangian is to replace the derivative ∂_μ by the so-called covariant derivative D_μ:

$$D_\mu \Psi \equiv (\partial_\mu - ieQA_\mu)\Psi \tag{1.3}$$

which, under the local U(1) transformations, transforms as for the non-interacting field

$$D_\mu \Psi \to e^{iQ\theta(x)} D_\mu \Psi \tag{1.4}$$

therefore preserving gauge invariance also when the interaction is included.

The last step is to include the propagation of the photon field $A_\mu(x)$ adding the kinetic term $1/4F_{\mu\nu}F^{\mu\nu}$, which is known to be also gauge invariant already from the classical covariant Maxwell equations, where $F_{\mu\nu} = \partial_\mu A_\nu - \partial_\nu A_\mu$.

At this point we can write the Lagrangian of QED as

$$\mathcal{L}_{QED} = \bar{\Psi}(x)(i\gamma^\mu D_\mu - m)\Psi(x) - \frac{1}{4}F_{\mu\nu}(x)F^{\mu\nu}(x). \tag{1.5}$$

This procedure that bring us to the $\mathcal{L}_{QED}$ can be generalized and summarized in this way: once the properties of the symmetries of a kind of interaction are known it is possible to build the Lagrangian of a system, whose particle interact through such interaction, starting from the Lagrangian of a free system and exploiting the symmetries of the interaction. In such way automatically arise the gauge fields, which act as force carriers, and whose number is the same of the number of the generator of the symmetric group relative to the interactions under consideration. Therefore the characteristic of the interactions are strongly related to its symmetries.

With this idea, the way to proceed in order to derive the Lagrangian for a system of particles interacting via strong interaction is the same followed in QED. The difference is due to the fact that strong interaction has different symmetries with respect to the electromagnetic interaction. In particular, while for the QED there is only one charge (and an anticharge), in the case of quarks starting from the Gell-Mann model one look for an interaction with three charges (and anticharges). Therefore, the symmetry owned by the strong interaction generates a non abelian group $SU(3)_C$, where C refers to colors and 3 refers to the three possible color states of the quarks, which are assumed to be in the fundamental representation.

Applying the gauge principle we can obtain the Lagrangian of QCD:

$$\mathcal{L}_{QCD} = \bar{q}_i^{\alpha}(x)(i\gamma^{\mu}D_{\mu} - \hat{m})_{ij}^{\alpha\beta}q_j^{\beta}(x) - \frac{1}{4}F_{\mu\nu}^{\alpha}(x)F_{\alpha}^{\mu\nu}(x), \qquad (1.6)$$

where $q_i^{\alpha}(x)$ denotes the quark field of color i=1,2,3 and flavor α=1,2,3..6; while $\hat{m}$ is the mass matrix that is color independent and diagonal in the flavor space $\hat{m} = diag_f(m_u, m_d, ..., m_t)$. The covariant derivative D_{μ} is in this case defined as

$$(D_{\mu})_{\alpha\beta} \equiv \delta_{\alpha\beta}\partial_{\mu} - ig_s\left(\frac{\lambda_{\alpha}}{2}\right)_{\alpha\beta}A_{\mu}^{\alpha} \qquad (1.7)$$

where A_{μ}^{α} is the gluon field with α=1,...,N_c^2-1=8, g is the bare coupling constant (equivalent to the electron charge e in the e.m.) and λ_{α} denotes the generators of the gauge SU(3)$_C$ group, whose main representation is given by the Gell-Mann matrices. The gluon field strength is:

$$F_{\mu\nu}^{\alpha}(x) = \partial_{\mu}A_{\nu}^{\alpha}(x) - \partial_{\nu}A_{\mu}^{\alpha}(x) + g_s f^{\alpha\beta\gamma}A_{\mu\beta}A_{\nu\gamma} \qquad (1.8)$$

and contains a bilinear term in the gluon fields $A_{\mu\beta}A_{\nu\gamma}$, due to the non-abelian character of the SU(3) group. The term $f^{\alpha\beta\gamma}$ is a totally antisymmetric tensor and its elements are the structure constants of the group. Like in the QED the interaction among quarks and gluons are contained in the term $\bar{q}i\gamma^{\mu}D_{\mu}q$. The key difference with QED is the fact that, due to the bilinear term in the gluon fields, the kinetic terms $F_{\mu\nu}^{\alpha}F_{\alpha}^{\mu\nu}$ contains a three and a four gluon terms that are responsible for the self interaction between gluons. This self-interaction has important implications:

1.2.1 Asymptotic freedom

One of the most important feature of QCD is the asymptotic freedom. It has been demonstrated in the 70s that asymptotic freedom is a specific features possible for non-Abelian gauge theories [8, 9].
This phenomenon can be investigated analyzing the renormalization of

a quantum field theory. In field theories, the quantum correction calculated with the perturbation theory have ultraviolet divergences which are originated from the states with high momenta. In the case of QCD and QED, that are renormalizable field theories, these divergences can always be absorbed in renormalized parameters. The energy scale at which the divergences are renormalized is named "renormalization point", and this is a function of the momentum tranfer Q. The physical observables do not depend on the renormalization point but the coupling $\alpha = g^2/4\pi$ depends on it and therefore α depends on the momentum transfer. It is possible to show that, for $N_f \leq 16$, α is a decreasing function of the renormalization point and therefore, in the case of QCD, with $N_f = 6$, α is a decreasing function of the momentum transfer, as indicated in the formula at the leading order [4, 5]:

$$\alpha_s(Q^2) = \frac{4\pi}{(11 - \frac{2}{3}N_f)\ln\left(Q^2/\Lambda^2_{QCD}\right)} \tag{1.9}$$

where $\Lambda_{QCD} \leq 220 - 260MeV$ is an intrinsic energy scale for the strong interactions. The momentum transfer dependence of the strong coupling is also shown in Fig. 1.1 along with extrapolation from several experimental data.

Qualitatively, asymptotic freedom can be described in terms of vacuum polarization. This phenomenon is present also in QED and is due to the fact that electric charges emits and absorbs continuatively photon that can temporarily transforms in couple $e^- - e^+$. This mechanism has the effect to screen the original charge with a consequent decreasing of the electric coupling at large distance (low momentum transfer). In QCD is present the same mechanism but, due to the non abelianan nature of QCD, the emitted gluons can generate both quark-antiquark and gluon-gluon pairs. So there are both screening and anti-screening effect and the anti-screening effect, caused by the coloured gluon clouds, prevails causing at low distance (high momentum transfer) a decreasing of the

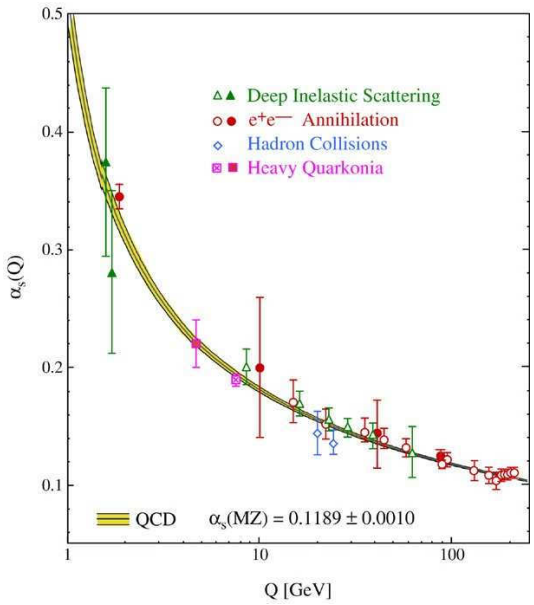

Figure 1.1: Running coupling as a function of the transfer momenta. The graphic have been obtained performing measure at various energy scales.

coupling.

The asymptotic freedom of the strong interaction permits to study perturbatively the strong interaction for high momenta transfer, while for energy comparable with $\Lambda_{QCD} = 200MeV$ the coupling becames very large and the perturbative treatment is completely inadequate.

1.2.2 Confinement

An important non-perturbative feature of the QCD is the colour confinement. The hypothesis of confinement says that hadrons can only exist in states with zero colour charge and quarks can only exist confined within hadrons. This hypothesis is supported by experimental results, in fact free quarks or gluons have never been observed in experiments, but until now there is no an analytical description of confinement.

Qualitatively, in the limit of massive quarks ($m_q > \Lambda_{QCD}$), it can be

described by a potential between a quark and an antiquark, as:

$$V(r) = -a \cdot \frac{1}{r} + b \cdot r \tag{1.10}$$

where a and b are real constants.
The first term is Coulomb-like while the second term, named "string potential", increases with the distance and is responsible for confinement. Beyond some critical distance the potential energy between the couple of quarks becomes so large that a new quark-antiquark pair pops up from the vacuum and the original quark-antiquark pair becomes two confined pairs (two mesons). However also in this case quarks are always confined inside hadrons.

1.2.3 Symmetries on QCD

In this paragraph will be discussed two global symmetries of QCD that are the chiral symmetry and the dilatational symmetry.

- **Chiral Symmetry**: We first introduce the right- and left-handed $q_{R,L} = 1/2(1 \pm \gamma_5)q$ quark fields. They are eigenstates of the chirality operator γ_5 with eigenvalues ± 1, in the case of free quarks with zero masses the chirality is equivalent to the helicity $\sigma \cdot \hat{p}$.
  This chiral symmetry leave the QCD Lagrangian density invariant under the global $SU(N_f)_L \times SU(N_f)_R$ transformations that are given by:

$$\begin{aligned} SU(N_f)_R : q_R \rightarrow e^{i\theta_a^R \frac{\tau_a}{2}} q_R \\ SU(N_f)_L : q_L \rightarrow e^{i\theta_a^L \frac{\tau_a}{2}} q_L \end{aligned} \tag{1.11}$$

  where τ_a are the generator of the $SU(N_f)$ group. This symmetry is equivalent to the symmetry that leave the Lagrangian invariant under global vector and axial vector transformations, $SU(N_f)_V \otimes SU(N_f)_A = SU(N_f)_R \otimes SU(N_f)_L$.
  In the so called chiral limit (m$\rightarrow$0) this symmetry is exact but, from

the analysis of hadrons spectra, there are no evidence of chiral symmetry and therefore one should conclude that chiral symmetry is not realized in the ground state (vacuum) of QCD.
However this is not in contradiction with the QCD classical lagrangian that would predict a nearly exact chiral symmetry. In fact even if the lagrangian has a symmetry it can happen that it is not realized in the ground state, in other words it is spontaneously broken (more precisely is the $SU(N_f)_V$ symmetry that is spontaneously broken). The mechanism responsible for such spontaneous symmetry broken is of nonperturbative origin and it is related to the existence of a quark condensate different from zero $\langle q\bar{q}\rangle = -(240MeV)^3$ [10]. An important consequence of the spontaneous breaking of exact continuous global symmetries is the existence of a massless mode, the so called "Goldstone boson", which, in the case of chiral symmetry, can be identified with pions. If chiral symmetry was a perfect symmetry of QCD the pions should be massless. However chiral symmetry for QCD is not exact since quarks have small, but non zero masses. Hence we expect that pions have a finite mass that has to be, however, small compared to the masses of all other hadrons, in fact the mass of pions is about 140 MeV, quite smaller than the proton mass, for example, that is 940 MeV.

- **Dilatational Symmetry**: Another feature of the Lagrangian of QCD in the case $m_q = 0$ is the invariance under the following scale transformation:

$$\begin{aligned} x_\mu &\to \epsilon^{-1} x_\mu; \\ q(x) &\to \epsilon^{3/2} q(\epsilon^{-1} x); \\ A^a_\mu(x) &\to \epsilon A^a_\mu(\epsilon^{-1} x). \end{aligned} \tag{1.12}$$

This symmetry of the QCD Lagrangian is called dilatational sym-

metry and the current associated to such symmetry is

$$\left\langle T^{\mu}_{\mu} \right\rangle = \epsilon - 3P = (\alpha_s/12\pi) \left\langle F^{\mu\nu} F_{\mu\nu} \right\rangle + m \left\langle \bar{\psi}\psi \right\rangle \tag{1.13}$$

that is the trace of the energy momentum tensor T^{μ}_{ν}. The increasing of the strong coupling breaks the dilatational symmetry, leading to a trace different from zero for the energy momentum tensor (trace anomaly).

1.3 Perturbative QCD

As already mentioned the most important consequence of asymptotic freedom is the possibility to use the method of perturbation theory to describe various QCD processes that happen at short distances (large momentum transfer). A rigourous description of perturbation theory could be done in the framework of path integral formulation [11]. In such paragrah we want anyway describe the main features of perturbation theory applied to QCD.

In perturbation theory interaction can be seen as a perturbation of the free theory. Obviously this way to proceed works as better as small the coupling α_S is, that is at increasing energy. In order to discuss about perturbation theory applied to quantum chromodynamics is useful to rewrite the QCD Lagrangian separing the part responsible for the interaction $\mathcal{L}_{int}$ from the free Lagrangian $\mathcal{L}_0$ [11]:

$$\mathcal{L} = \mathcal{L}_0 + g A^a_\lambda \bar{\psi} \gamma^\lambda t^a \psi - g f^{abc} (\partial_k A^a_\lambda) A^{kb} A^{\lambda c} - \frac{1}{4} g^2 (f^{eab} A^a_k A^b_\lambda)(f^{ecd} A^{kc} A^{\lambda d}). \tag{1.14}$$

In $\mathcal{L}_0$ are englobed the free propagation term for the quark fields and for the gluon fields; while the second term indicates the interaction between quark and gluons, similar to lepton-photon interaction in QED, and the other two terms indicate the self-interaction between gluons.

In order to describe scattering between QCD particles (quarks and gluons), one have to deal with a basic quantity of all collision processes:

the scattering matrix S which relates the fields before the interaction ϕ_{in} with those after the interaction ϕ_{out}. The S-Matrix encodes all information about the scattering process, thus is strongly related to $\mathcal{L}_{int}$, more precisely it is possible to show that the transition probability is related to $\mathcal{L}_{int}$ through the relation:

$$\left\langle \phi_{out} \left| \hat{S} \right| \phi_{in} \right\rangle = \left\langle \phi_{out} \left| T e^{i \int d^4x \mathcal{L}_{int}} \right| \phi_{in} \right\rangle \tag{1.15}$$

where T is the ordered-time operator.
If the coupling costant g is small enough this expression can be expandend in power series of g and this series can be turn out in a very simple structure using the Feynman diagrams and the Feynman rules. Before describe how to calculate the cross section from the S-matrix is useful to make some consideration regarding the scattering matrix. It is defined in such a way that no interaction correspond to the unit matrix. Therefore it can be write as a sum of a unit matrix plus the interaction part encoded now in the T-matrix defined as following $S = I + iT$. Moreover the matrix elements of $\left\langle \phi_{out} \left| \hat{S} \right| \phi_{in} \right\rangle$ contains a kinematical term reflecting the energy and momentum conservation $(2\pi)^4 \delta^4(p_f - p_i)$ and is not directly linked to the specific dynamics of the interaction. It is useful to introduce a quantity, linked to the S-matrix, that is free from such a term. This quantity is the invariant matrix element $\mathcal{M}$ defined as:

$$\left\langle \phi_{out} \left| \hat{S} \right| \phi_{in} \right\rangle = \left\langle \phi_{out} \left| I + i\hat{T} \right| \phi_{in} \right\rangle = \langle \phi_{out} | \phi_{in} \rangle + (2\pi)^4 \delta^4(p_f - p_i) \cdot \mathcal{M}_{oi}. \tag{1.16}$$

From the invariant matrix elements it is possible to calculate the transition probability per unit time and per unit volume that is equal to $(2\pi)^4 \delta^4(p_f - p_i) |\mathcal{M}_{oi}|^2$. Multiplying this last quantity for the number of final states and dividing from the initial flux one obtain the cross sections of the process that in case of a two body process can be written as:

$$\frac{d\sigma}{dt} = \frac{1}{64\pi s} \frac{1}{|\vec{p}_{1_{cm}}|^2} |\mathcal{M}|^2 \tag{1.17}$$

where $\vec{p}_{1_{cm}}$ is the momenta of one of the incoming particles and s,t are the Mandelstmann variables.

The results of perturbative QCD (pQCD) are in good agreement with experimental data for collisions at energies $\sqrt{s} \geq 1\,TeV$ and for high momenta particles $p_T \geq 10\,GeV$. Unfortunately, due to the colour confinement, in experiments the initial and final state observed are hadrons. This implies that in order to have a description of the collision it is necessary to consider both the hard scattering between partons of the different colliding hadrons, that can be treated perturbatively, and also the dynamics of hadronization involving a long range interaction and therefore cannot be treated pertubatively.

This issue is solved by the factorization theory, that consists to factorize the cross section in two parts: the short distance part which can be calculated in the framework of pQCD, and the long range part that involves hadronic wave functions and/or fragmentation function and cannot be calculate within pQCD [12, 13]. These last non-perturbative quantities have however important scaling properties that allows to determine their evolution with energy and momentum transfer. The first of this property permits to calculate the matrix element for any momentum transfer scale Q^2, once they are known for a particular Q_0^2, towards the Doskshitzer-Gribov-Lipatov-Altarelli-Parisi (DGLAP) equations [14–16]. The second property is their universality i.e. they are at least in certain mathematical region independent from the specific process. This means that if they are measured in one process (usually e^+e^- collisions) can be applied to another process. The perturbative QCD parton model is based on this factorization picture of hard process.

1.4 Phenomenological approach to non perturbative QCD

The perturbative QCD permits to give a good description of all phenomena whose energy scale is large compared to the energy scale of the strong interaction $\Lambda_{QCD} \approx 250MeV$ ($\Lambda_{QCD}^{-1} \approx 0.8fm$). Unfortunately there are many interesting process of QCD matter that involve low energy and therefore cannot be treaded perturbatively, it is sufficent to think for example at the confinement or at the process of phase transition of QCD matter. In order to study these non-perturbative process various model have been proposed, such as the *bag model* and the *Nambu-Jona-Lasino model* (NJL) that we mention because in this thesis we present some novel results about the propagation of sound waves in the QGP of interest for evolution of the first stage of the Early Universe.

1.4.1 MIT Bag model

In the Bag Model hadrons are considered as bags embedded in a non perturbative QCD vacuum. There are various version of Bag Model, here will be described the MIT bag model [17]. In such model quarks are treated as particles with zero mass inside a bag of finite dimension. The confinement in the bag model is due to a balancement of two "forces": the bag pressure, which is directed inward and the pressure arising from the kinetic energy of the quarks directs outward. The bag pressure is a phenomenological quantity that permits to take into account non-perturbative effects and in particulat the trivial QCD vacuum.

One way to estimate the bag pressure is to consider massless free quarks in a spherical cavity of radius R [18]. In practice, one solves the Dirac equations for a massless quark inside the cavity and, in order to consider confinement, one impose that the scalar density of the quarks $\bar{\psi}\psi$, where

ψ is the solution of Dirac equation, vanishes at the bag surface. From this constraint emerges an equation that permits to calculate the kinetic energy of one quark as a function of the radius of the sphere and such an equation is satisfied for [18]

$$E = \frac{2.04}{R} \tag{1.18}$$

which can be read as an effect of the indetermination principle $E \cdot t \approx \hbar$ hence massless quarks moves at the speed of light: $t = R$.
Multiplying this kinetic energy for the number of quarks N inside the sphere and adding the energy arising from the Bag pressure B, it is possible to calculate the total energy E as a function of R and of B:

$$E = \frac{2.04N}{R} + B\frac{4}{3}\pi R^3. \tag{1.19}$$

At this point the equilibrium radius of the system is determinated by the equation $dE/dR = 0$ which allows, knowing the radius R, to calculate B. If we consider a system of three quarks in a hadrons of radius $R = 0.8$ we obtain for $B^{1/4}$ the value of $206MeV$. The different properties of hadrons lead to different estimation for the bag pressure ($B^{1/4}$), that however are in the range $145MeV - 235MeV$.
The Bag model permits to have an estimate of the transition temperature T_0 to the quark matter from the hadronic state. In fact, if the pressure of the quark matter inside the bag exceed the bag pressure, the bag cannot confine quarks and gluons and a new state of matter is formed. in order to do that it is necessary to calculate the pressure of the system that in the simplest case of massless non interacting quarks and gluons is given by

$$P = 37\frac{\pi^2}{90}T^4 \tag{1.20}$$

where 37 are the total degrees of freedom. Now it is possible to calculate T_c that correspond to the temperature for which the pressure P is equal to the bag pressure. Utilizing for $B^{1/4}$ the value of $235MeV$ one obtain $T_c = 170MeV$.

1.4.2 Lattice QCD

A powerful method to study the properties of the QCD at low energies is the lattice QCD and in this section will be briefly described the main features of lattice QCD and will be described some results related to the physics of phase transitions [19].

Path integral and partition function

Using the Feynman path integral formulation the transition amplitude can be written as a sum over all possible configuration of the fields. The vacuum to vacuum transition amplitude in such formulation is given by

$$\left\langle 0 \left| e^{-i\hat{H}(t_f - t_i)} \right| 0 \right\rangle = \int \mathcal{D}A^{\alpha}_{\mu} \mathcal{D}\bar{\psi}(x) \mathcal{D}\psi(x) e^{iS} \tag{1.21}$$

where S is the action coming from the Lagrangian in Eq. 1.6

$$S = \int d^4x \mathcal{L}(A^{\alpha}_{\mu}, \bar{\psi}, \psi) \tag{1.22}$$

From the Eq. 1.21 it is possible to obtain an expression for the grancanonical partition function of quarks, antiquarks and gluons in thermal equilibrium at a certain temperature T. This can be done performing a Wick-rotation, moving from Minkowski to Euclidean space. In practice, one replace time t by imaginary time τ ($t \to i\tau$), and restricts the integration range over τ in the action to the interval $[0, \beta = 1/T]$ [20]. In this way one obtain:

$$\mathcal{Z} = \int \mathcal{D}A^{\alpha}_{\mu} \mathcal{D}\bar{\psi}(x,\tau) \mathcal{D}\psi(x,\tau) e^{\int d^4x \mathcal{L}(A^{\alpha}_{\mu}, \bar{\psi}, \psi)} \tag{1.23}$$

That is the grancanonical partition function for a QCD system at finite T. The integral in Eq. 1.21 and 1.23 have contributious from an uncountably infinite number of degrees of freedom due to the continuous nature of space-time. These infinities must be removed by regularizing the theory.

Basics of lattice QCD

The regularization of the integral in Eq. 1.23 can be achieved introducing a four dimensional space-time lattice of size $N_\sigma^3 \times N_\tau$ with a lattice spacing a and performing the integration is such lattice [6]. Volume and temperature are then related to the number of points in space and time directions

$$\begin{aligned} V &= (N_\sigma \cdot a)^3; \\ T^{-1} &= N_\tau \cdot a \end{aligned} \tag{1.24}$$

In order to perform the discretization of the integral of Eq. 1.23 is necessary to divide the action S in a part that contains a purely gluonic contribution S_G and one that contains the fermion part S_F, ($S \equiv S_G + S_F$). This because the discretization of the two contribution must be done by different procedures.
In order to discretize the gluonic part one proceeds introducing the link variables $U_\mu(x)$, which are associated with the link between two neighboring sites on the lattice and describe the parallel transport of the fields A_μ from site x to $x + \hat{\mu}a$. Such link variables are determined by the line integral of A_μ along the link

$$U_\mu = \mathcal{P} e^{ig \int_x^{x+\mu a} dx^\mu A_\mu(x)} \tag{1.25}$$

where the $\mathcal{P}$-operator path-orders the field $_\mu$ along the integration path and g is the strong coupling. One uses U_μ in place of A_μ on the lattice because it is impossible to formulate a lattice version of QCD directly in terms of A_μ keeping gauge invariance. The U matrices on the other hand are elements of the SU(3) colour group and transform very simply under a gauge transformations:

$$U_\mu(x) \to G(x) U_\mu(x) G^{-1}(x + \mu). \tag{1.26}$$

In particular from the above equation seems clear that any closed loop of these matrices is gauge invariant. The minimum closed loop in the lattice

is a 1×1 square of lattice links, called *plaquette*, and in the following equation are shown the U matrices calculated along such a plaquette

$$U_{plaq} = U_\mu(x)U_\nu(x+\mu)U_\mu(x+\nu)U_\nu(x) \tag{1.27}$$

Using U_{plaq} it is possible to build a gauge invariant action for the gluonic field, called Wilson gauge action

$$S_G = \beta \sum_{plaq}(1 - \frac{1}{3} ReTr U_{plaq}) \tag{1.28}$$

where $\beta = 6/g^2$ is the gauge coupling. This lattice gauge action reproduces the continuum version of the QCD action in the limit $a \to 0$ up to cut-off errors of the order of a^2.

Regarding the discretization of the fermionic part of the action, it can be done naively replacing the derivatives appearing in the fermion Lagrangian by finite differences, i.e. $\partial_\mu \psi(x) = \psi_{n+\mu}(x) - \psi_{n-\mu}(x)/2a$. However if one performs this kind of discretization a specier doubling problem appears when one goes to the continuum limit. This is due to the fact that the lattice version of the massless fermion propagator have poles not only at zero momentum, but also at all corners of the Brillouin zone and hence generate 16 rather than a single fermion species. This problem can be solved either using the Wilson fermion formulation [6] or using the staggered fermions formulation, which consists in distributing the fermion Dirac spinors over several lattice sites [19, 21]. The staggered fermion formulation does not eliminate the species doubling problem but reduces from 16 to 4 the fermion species, however it has the advantage to preserve a continuous subgroup of the original global chiral symmetry [22].

With this new formulation of the actions is possible to write the QCD partition function on a lattice

$$Z(N_\sigma, N_\tau, \beta, m_q, \tilde{\mu}) = \int \prod_{n\eta} dU_{n,\eta} (\det Q^{KS}(m_q, \tilde{\mu}))^{n_f/4} e^{-\beta S_G} \tag{1.29}$$

where Q^{KS} is the staggered fermion matrix [19].
The integrand of Eq. 1.29 can be calculated with standard numerical techniques if $\tilde{\mu} = 0$. In fact in such a case the fermion determinant of Eq. 1.29 is real and positive. A problem emerges instead in the case $\tilde{\mu} \neq 0$ due to the fact that in this case the fermion determinant is complex. The imaginary part of this determinant however is zero, hence does not give any problem, but the real part it is not strictly positive and constitutes a serious problem in the application of numerical technique to solve the integral. This sign problem constitutes the main problem if one want to apply lattice QCD for $\tilde{\mu}$ different from zero as it would desireable to know if the transition has a critical point and to know the thermodynamics of compact stars.
From the partition function it is possible to calculate all thermodynamic observables, neverthless before it is necessary to set the lattice in such a way to reduce the discretization errors and one has to be sure that the lattice discretizate action reproduces the continuum limit. Moreover it is necessary to determine the temperature scale because the lattice observables are dimensionless and are calculated in appropriate units of lattice space a. In order to determine the temperature scale one has to perform calculations for an observables for which is known the physical value in MeV. Observables usually used for this purpose are the hadron masses, m_H, and in the following expression it is shown how the temperature is determined from it

$$\frac{T}{m_H} = \frac{1}{m_H a N_\tau}. \tag{1.30}$$

Result from Lattice QCD

Lattice QCD is a powerful method to study the phase transition of the QCD matter through the calculation of some observables that are sensitive to the phase transition. In fact such a phase transition is expected to occur at $T \approx 150 - 200 MeV \leq \Lambda_{QCD}$ therefore dwelling in the

non perturbative regime. A useful order parameter of the QCD matter is the *Polyakov loop* defined as:

$$L(T) \approx \lim_{r\to\infty} e^{-\frac{V(r)}{T}} \tag{1.31}$$

where $V(r)$ represents the potential between a static quark-antiquark pair separated by a distance r. This potential in the pure gauge case, i.e. without light quarks, is proportional to σr, where σ is the string tension. Therefore in the limit $r \to \infty$ the potential $V(r)$ tends to infinity and the Polyakov loop vanishes in a confined phase.
In a deconfined medium the color screening among gluons melts the string tension making $V(r)$ finite also at large distance r and consequently L is different from zero. The Polyakov loop hence can be viewed as an order parameter. The temperature T_c of the transition from the confined to the deconfined phase corresponds to the temperature at which L becomes different from zero. The behavior of the Polyakov loop for the different phase is summarized here

$$\langle L\rangle \begin{cases} = 0, & \Leftrightarrow \text{confined phase}, T < T_c \\ > 0, & \Leftrightarrow \text{deconfined phase}, T > T_c \end{cases}. \tag{1.32}$$

For the case of finite quark masses also in the confined phase $V(r)$ has a superior limit due to the finite masses. In fact, in this case, when the string potential becomes equal to the mass M_h of the smallest hadron it becomes more favorable to produce an additional quark-antiquark pair that allow for a new hadron creation and consequently the potential stops to increase even in the vacuum, i.e. even without color screening dynamics. Hence L does not vanishes but is however exponentially small as indicated in the following equation

$$L(T) \approx e^{-\frac{M_h}{T}} \tag{1.33}$$

In the deconfined phase L is larger than in the confined phase and hence also for finite quark masses it remains a good order parameter even if a

real first order phase transition is not observed. Indeed from the study of susrbilities it has been found that the QGP transition is a cross-over. Another step in the understanding of the confinement to deconfinement phase transition can be made analyzing the behavior of energy density and pressure as a function of temperature. As we have said above, from the partition function Z can be determined all thermodynamic variables and in particular E and P can be calculated as

$$\begin{aligned} \epsilon &= \left(\frac{T^2}{V}\right)\left(\frac{\partial \ln Z}{\partial T}\right)_V \\ P &= T\left(\frac{\partial \ln Z}{\partial V}\right)_T \end{aligned} \tag{1.34}$$

An enhancement near the critical temperature T_C in the energy density indicates an increase of the effective number of degrees of freedom, signal of a transition from hadronic matter to a deconfined system of quarks and gluons.
The results of lattice calculation obtained by the Wuppertal-Budapest Collaboration for the Equation of State (EoS) with N_τ=6,8 or 10 lattices are shown in Fig. 1.2 [23].

One can observe that near the critical value T_C the energy density shows a rapid increase. Such an enhancement indicates an increase of the effective number of degrees of freedom, signal of a transition from hadronic matter to a deconfined system of quarks and gluons. Moreover, it is important to note that the energy density in the deconfined phase is about $15-20\%$ below the Stefan-Boltzmann limit and thus there is a strong interaction among quark and gluons.

1.5 Quark Gluon Plasma

Asymptotic freedom suggests that under particularly condition of temperature or density the interaction which confine quarks and gluons inside hadrons becomes smaller enough to release them. Thus a new

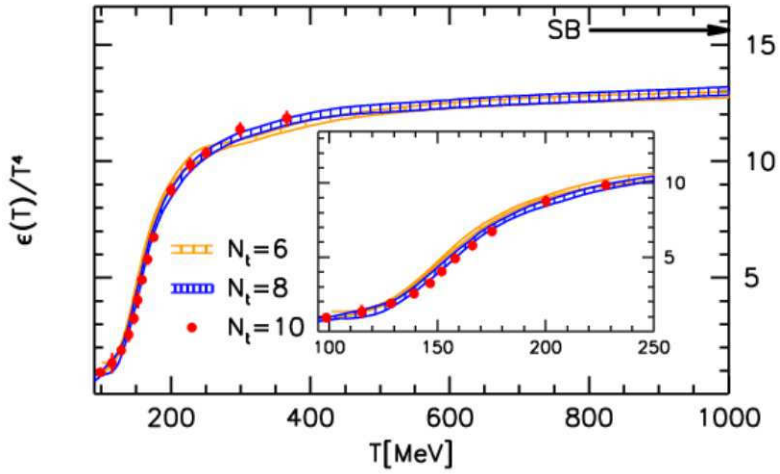

Figure 1.2: EoS of the Wuppertal-Budapest Collaboration [23]. The energy density is normalized by T^4 and is reported as a function of the temperature on N_τ= 6, 8 and 10 lattices. The Stefan-Boltzmann limit is indicated by an arrow.

state of the matter can exist in which the color charges are deconfined in a *Quark Gluon Plasma (QGP)*. There are two methods for the creation of the Quark Gluon Plasma:

- **QGP at high T**: One assume that the QCD vacuum is heated in a box. At low temperature, hadrons, such as pions, kaons, etc., are thermally excited from the vacuum. Note that only the color-white particles can be excited by the confinement at low energies. Because the hadrons are all roughly the same size (about $1fm$), they start to overlap with each other at a certain critical temperature, T_C. Above this temperature, the hadronic system dissolves into a system of quarks and gluons (QGP). Note that in the QGP thus produced the number of quarks, n_q , is equal to that of antiquarks, $n_{\bar{q}}$. Although this critical temperature is extremely high in comparison with (for example) the temperature at the center of the Sun, $1.5 \times 10^7 K = 1.3keV$, it is a typical energy scale of hadronic interactions and can be obtained in laboratories.

- **QGP at high** ρ_B: Suppose to put a large number of baryons into a cylinder with a piston and compress the system adiabatically, keeping $T \approx 0$. The baryons start to overlap at a certain critical baryon density, ρ_C, and dissolve into a system of degenerate quark matter. The quark matter thus produced is of high baryon density with $n_q \gg n_{\bar{q}}$.

Based on the two recipes for high T and high ρ, we should expect to find QGPs in three places: (1) in the early Universe (T), (2) at the center of compact stars (ρ) and (3) in the initial stage of colliding heavy nuclei at sufficiently high energies (T, ρ):

1. **In the early Universe:** according to Friedmann's solution of Einstein's gravitational equation, the Universe experienced an expansion from a singularity at time zero [24]. This scenario has been confirmed by the formulation of Hubble's law for the red shift of distant galaxies [25]. Hubble's law states that all objects observed in deep space (intergalactic space) are found to have a Doppler shift observable relative velocity to Earth, and to each other; and that this Doppler-shift measured velocity, of various galaxies receding from the Earth, is proportional to their distance from the Earth and more generally to all other interstellar bodies:

$$v = H_0 \times l \tag{1.35}$$

where $H_0 = 65 - 79 kms^{-1}Mpc^{-1}$ is the Hubble constant.
After the initial singularity, the temperature decreases inversely proportional to the scale parameter a so that the Early Universe passes through the electroweak phase transition at $t \approx 10^{-10} sec$ (corresponding to $T \approx 100 GeV$) and the QCD phase transition at $t \approx 10^{-5} sec$ ($T \approx 150 MeV$), then passing through the *Big Bang Nucleosynthesis (BBN)* at $t = 1\,sec - 3\,min$ ($T = 0.1 - 1\,MeV$).

This BBN plays a crucial role in constraining our views of the Universe: it is essentially the only probe for the radiation dominated epoch during the range $\approx$1-$10^4 sec$. Moreover, the aforementioned phase transitions could strongly affect the BBN, especially if they are first order phase transitions [8].

1.5.1 Energy density fluctuations in Early Universe

From this point of view, the role of the QCD phase transition on the evolution of the young universe is interesting because at that time a big change in the number of the degrees of freedom took place. The role of this primordial transition is still matter of debate. For example, in [26] it was realized that an inhomogeneous distribution of baryons due to a first-order QCD transition might change the primordial abundances of the light elements [27].
One expects that the use of this EoS in the Friedmann equation allows us to determine the precise time evolution of the thermodynamic parameters in the early Universe. In this context, we studied the impact of the EoS on the primordial QCD transition using: Bag Model as well as the most recent and realistc one coming from lQCD. Moreover, during the QCD transition strong magnetic fields might have been present [28, 29]. In order to take into account this possibility we present our results for the energy density fluctuations in presence of a strong magnetic background, using an effective model to compute the relevant equation of state [30]. Here we consider an admittedly large value of the magnetic field, $B \approx 10^{15}$ Tesla; this value of B is chosen to estimate the maximum effect a magnetic field can have on the evolution of the energy density fluctuations in the early universe. The use of an effective model to describe the QCD plasma in presence of a magnetic background

might appear opinable, since such model fails to reproduce the dependence of the chiral critical temperature on the magnetic field strength [31] (see however [32] and also the discussions in [33]). However our main point is to discuss the effect of the strengthening of the phase transition with the strength of $\vec{B}$, a characteristic which is observed both in lattice simulations and in the model calculation, which is not related to the dependence of the critical temperature on $\vec{B}$.

In the energy range considered in the early universe phase transition, it is possible to describe the plasma as a quark-gluon plasma plus electroweak matter in thermal equilibrium. The energy density (as well as other thermodynamical quantities) are then written as

$$\varepsilon = \varepsilon_{ew} + \varepsilon_{qgp}, \tag{1.36}$$

where ε_{ew}, ε_{qgp} correspond to the energy densities of the electroweak and QCD plasmas respectively. The electroweak sector will be considered as a perfect gas of massless particles in thermal equilibrium at the temperature T, hence

$$\varepsilon_{ew} = g_{ew}\frac{\pi^2}{30}T^4, \quad P_{ew} = g_{ew}\frac{\pi^2}{90}T^4 \ , \tag{1.37}$$

with g_{ew} =14.45 [8].

To determine the temperature evolution we solve the Friedmann equation that, assuming that the expansion of the Universe is isentropic, takes the form

$$\frac{d\varepsilon}{dt} = -3\sqrt{\frac{8\pi G\varepsilon}{3}}(\varepsilon + P) \tag{1.38}$$

The numerical solutions for the three different EoS are reported in Fig. 1.3 that clearly shows how changing the equation of state affects the behaviour of temperature vs time. The Bag Model (green line) presents a plateau during the transition corresponding to the

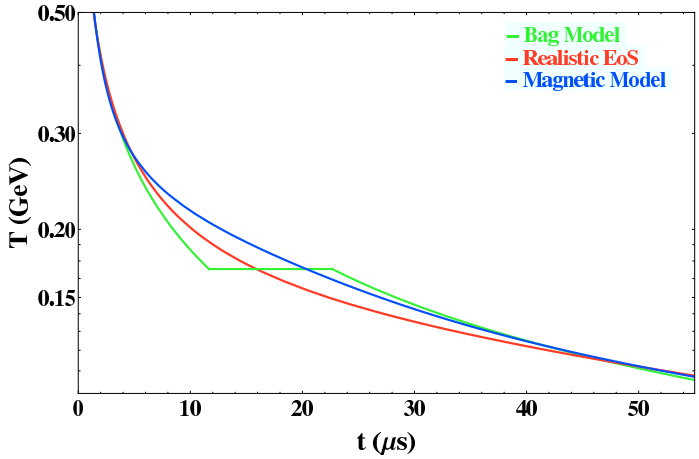

Figure 1.3: Temperature behavior obtained by solving the Friedmann equation for the three different approach presented in the text: the red line refers to the realistic lattice calculation, the blue line represents the same realistic case but with the inclusion of the magnetic field while the green line reports the simple Bag Model.

critical temperature of about 170 MeV, at which the phase transition is of first order. On the other hand because the QCD phase transition is actually a crossover, the use of the lattice EoS (red line) results in a smooth change of the temperature as a function of time. The magnetic field does not change the nature of the phase transition (blue line) but only leads to a delay of the cooling. We stress that the difference between the three cases are strictly confined to the time interval in which the transition takes place, while at later times the temperatures for the three different cases are very similar.

Finally we want to study the role of the primordial QCD transition on the energy density fluctuations in the early universe. We note that if the QCD phase transition was of the first order then the speed of sound would vanish at the critical temperature, implying large oscillations of the energy density fluctuation. For the realistic case of the crossover we do expect the fluctuations to be damped because the speed of sound never reaches zero but simply decreases

to a finite value in the crossover temperature range; nevertheless it is interesting to analyse how these fluctuations develop in presence of the crossover transition [34]. In order to accomplish this goal we solve the following system of equations [35]:

$$\frac{1}{H}\delta' + 3(c_s^2 - w)\delta = \frac{k}{H}\psi - 3(1+w)\alpha, \tag{1.39}$$

$$\frac{1}{H}\psi' + (1-3w)\psi = -c_s^2\frac{k}{H}\delta - (1+w)\frac{k}{H}\alpha, \tag{1.40}$$

$$\frac{1}{H}\delta'_{ew} = \frac{k}{H}\psi_{ew} - 4\alpha, \tag{1.41}$$

$$\frac{1}{H}\psi'_{ew} = -\frac{k}{3H}\delta_{ew} - \frac{4k}{3H}\alpha, \tag{1.42}$$

$$\left[\left(\frac{k}{H}\right)^2 + \frac{9}{2}(1+w_R)\right]\alpha = -\frac{3}{2}(1+3c_{sR}^2)\delta_R, \tag{1.43}$$

where the prime denotes the derivative with respect to the conformal time η.

In the above equations the most important quantity for our investivation is the function $\delta \equiv \delta\varepsilon/\varepsilon$, where $\delta\varepsilon$ corresponds to the energy density fluctuation and ε to the background energy density. Among the other variables involved in the dynamics, ψ is related to the fluid velocities and α to the fluctuation of the temporal part of the metric tensor. The function w is an input and corresponds to the ratio background pressure over background energy density, which we compute case by case according to the input EoS's presented before. In the system of Eqs. (1.39)-(1.43) the first two equations describe the dynamics of the QCD plasma and follow from the energy-momentum conservation; the second couple of equations refers to the electro-weak sector and follows from the Euler equation of general relativity; finally the the last one follows from the Einstein R_0^0-equation and couples the QCD plasma to the electroweak one. For more details we refer to [34, 36].

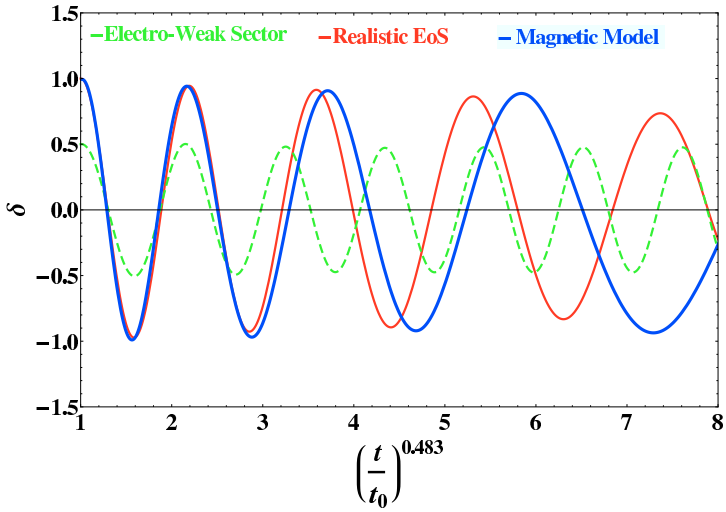

Figure 1.4: Time evolution of the energy density function with respect to the electro-weak part (green dashed line). The red line refers to the lattice QCD data while the blue line indicates the case in which a primordial magnetic field is included.

In Fig. 1.4 we plot the result of our numerical solution of the system of Eqs. (1.39)-(1.43), focusing in particular on the energy density fluctuations δ. The initial time is $t_0 = 1.35\ \mu s$ and is chosen in order to have an initial temperature of 500 MeV, while the final time corresponds to 110 μs which is well beyond the QCD transition. In the figure the green dashed line corresponds to the electro-weak component, while red (blue) solid line corresponds to the QCD EoS without (with) magnetic field. It is evident that the presence of the QCD crossover in the EoS at $B = 0$ damps the energy density fluctuations in the considered time range in both cases, affecting also the frequency of these fluctuations. Moreover, effect of the magnetic field is to make this damping less efficient; this was expected because $B \neq 0$ makes the crossover a stiffer one, thus reducing strongly the speed of sound in the crossover region compared to the speed of sound at $B = 0$, and favouring the energy density fluctuations bringing the system behaviour closer to

the one expected for a first order phase transition.
In this way, we found that the oscillations of the energy density fluctuations are damped during the QCD crossover, this implies that there are small chances of inhomogeneities phenomena during the Big Bang nucleosynthesis.

2. **In the core of super-dense stars**: there are three possible stable branches of compact stars: white dwarfs, neutron stars and quark stars. The white dwarfs are made entirely of electrons and nuclei, while the major component of neutron stars is liquid neutrons, with some protons and electrons. The first neutron star was discovered as a radio pulsar in 1967 [37]. If the central density of the neutron stars reaches $5-10\rho_{nm}$, there is a fair possibility that the neutrons will melt into the cold quark matter. There is also a possibility that the quark matter, with an almost equal number of u, d and s quarks (the strange matter), may be a stable ground state of matter; this is called the strange matter hypothesis. If this is true, quark stars made entirely of strange matter become a possibility. In order to elucidate the structure of these compact stars, we have to solve the Oppenheimer-Volkoff equation [38], obtained from the Einstein equation, together with the equation of states for the superdense matter.

3. **In the initial stage of the Little Bang**: by means of relativistic nucleus-nucleus collisions with heavy ion accelerators. At such relativistic energies the nuclei are Lorentz-contracted as *pancakes*. When the center-of-mass energy per nucleon is more than about 10-20 GeV, the colliding nuclei tend to pass through each other, and the produced matter between the receding nuclei is high in energy density and temperature but low in baryon density. The Relativistic Heavy Ion Collider (RHIC) at Brookhaven National Laboratory

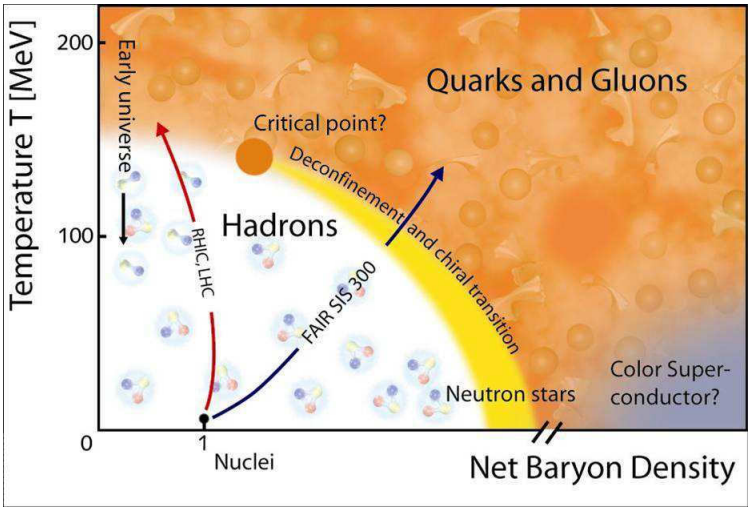

Figure 1.5: Phase diagram of the QCD matter in the (μ,T) plane.

and the Large Hadron Collider (LHC) at CERN provide us with this situation. In particular RHIC accelerates nuclei at the energy range $10 - 200\,AGeV$ creating a transient state at maximum temperature $T_{max} \cong 350\,MeV$ and LHC at $T_{max} \cong 600\,MeV$ which are both values above the one at which the transition to QGP is expected.

1.6 Phase diagram of the QCD

The above consideration bring us to sketch the phase diagram for the QCD matter Fig.1.5. In the horizontal axis there is the baryon chemical potential μ_B, while in vertical axis there is the temperature, both quantities are expressed in MeV. The cold nuclear matter, as one can find in the inner part of a lead nucleus, has a temperature equal to zero and a chemical potential μ_B equal to 940 MeV. In correspondence to $\mu_B = 0$ and T=170 MeV the matter undergoes a cross over from the confined phase of hadronic gas to a quark gluon plasma (QGP). As we have seen this phase should have existed in the early phase of the Universe after the Big-Bang. In the region of non zero μ and low temperature T there is

also a phase transition towards the QGP phase, the place in which may exist this condition is the interior of neutron stars. The phase transition in this region seems to be of first order. For some moderate value of μ and T a critical point is expected, for which the first order transition becomes a crossover. The only possibility to create the Quark gluon plasma in laboratory is to perform ultra-relativistic heavy-ion collisions that will be discussed in the next chapter.

CHAPTER 2

QGP IN HEAVY ION COLLISIONS

Contents

The most useful experimental approach to probe the high temperature QCD matter is the detailed analysis of heavy ion collisions (HIC). In fact, the suggestion of using HIC to create high density states of matter predates the full development of QCD. In heavy ion collisions at relativistic energies, indeed, there is both compression of the baryonic matter in the nuclei and also the release of a large amount of energy within a small volume from the almost simultaneous collisions of many nucleons. One

or the other, or both, of these consequences of the interactions have the potential to produce new forms or phases of QCD matter. This is one of the prime reasons why in the past few decades much effort has been spent studying collisions of heavy ions at higher and higher energies [39]. The modern era of HIC arrived with beam energies of 10-200 GeV/nucleon at fixed-target facilities: the Alternating Gradient Synchrotron (AGS) at Brookhaven National Laboratory (BNL) and the Super Proton Synchrotron (SPS) at European Center for Nuclear Research (CERN). Both the AGS and the SPS accelerated protons and several types of ions onto fixed targets of heavy nuclei [40].

In 2001 has started the activity at RHIC (Relativistic Heavy Ion Collider) where it was possible to reach energies up to 200 GeV for nucleons. The experiments at RHIC have supplied a large amount of observables that have permitted to start a quantitative study of the Quark Gluon Plasma properties [41–44]. In 2010 the experiments at LHC have started with an energy of 2.7 TeV per nucleons and in 2013 it will be performed experiments with the highest energy accessible at LHC that is 5.5 ATeV. In this chapter the main features of the collision dynamic will be described, as well as the evolution of the matter created in such collisions and the observables that allow to identify if a new state of matter have been created during the collisions.

2.1 Collision Dynamics

In the initial stage of this kind of collision, the incoming nuclei approaches each other with more than 99.9% of the speed of light and so they are strongly Lorentz contracted along the beam direction. Thus in the center of mass frame they appear as two tiny disks of thickness $2R/\gamma_{c.m.}$, where R is the nuclear radius and

$$\gamma_{c.m.} = \frac{1}{\sqrt{1-\beta^2}} = \frac{1}{\sqrt{1-\frac{p_z^2}{E_{c.m.}^2}}} \tag{2.1}$$

where $E_{c.m.}$ is the energy of one nucleus in the center of mass frame.
However, due to the uncertainty principle ($\Delta p_z \Delta z \approx \hbar$), the longitudinal size of nuclei cannot be smaller than a value Δz which depends on the energy of the collision and can be larger than the contracted geometrical radius. This implies a geometrical delocalization of the nucleons inside the nuclei that consequently pass through each other and leave the region of the collision. Such a transparency behaviour of ultrarelativistic nuclei increases with the energy of the collision and allows to create in the central region of the collision a matter that is not contaminated by the original baryonic matter of the colliding nuclei.
As well established by the deep-inelastic lepton-hadron scattering experiments, the nucleon is composed of valence quarks, gluons and sea-quarks. Just after the collision, the nuclei are mostly composed by gluons because the parton distributions functions inside the nucleons at high energy is a function of $x \approx p_T/\sqrt{s}$. A successful picture that describes the initial stage was proposed by Bjorken. According to this picture the production of particles in ultra-relativistic heavy-ion collision is due to the excitation of the vacuum caused by the collision of the two beams of partons, with a consequent production of virtual quanta [45]. It takes a certain proper time, τ_{de} (de-excitation or de-coherence time), for these quanta to be de-excited to real quarks and gluons. The de-excitation time would

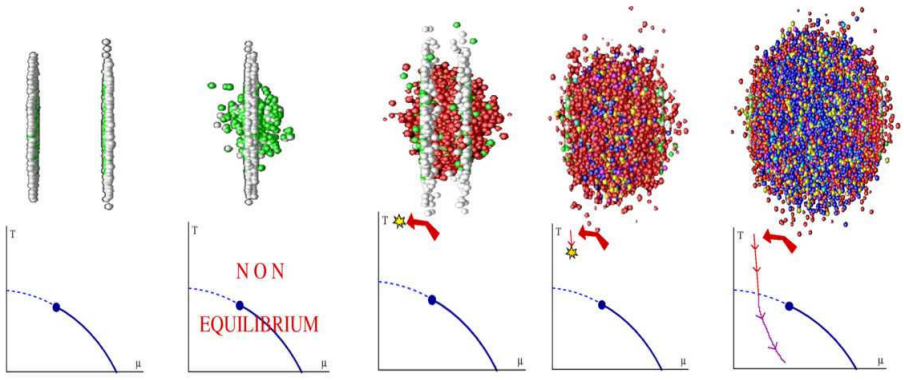

Figure 2.1: Heavy ion collision sequence

typically be a fraction of 1 fm. The state of matter for $0 < \tau < \tau_{de}$ is said to be in the pre-equilibrium stage. Since τ_{de} is defined in the rest frame of each quantum, it experiences Lorentz dilation and becomes $\tau = \tau_{de}\gamma$ in the center-of-mass frame of the collision, where γ is the Lorentz factor of each quantum. This implies that slow particles emerge first near the collision point, while the fast particles emerge last, far from the collision point. This phenomenon is called the *inside-outside cascade*. The real partons produced during the de-excitation process interact with each other and constitute an equilibrated plasma (quark-gluon plasma) [46].

An important role in the collision dynamics is played by the geometric aspects of high energy heavy ion collsion that can be described using the Glauber model that allows to estimate the initial spatial distribution in the transverse plane that will be described in the following subsection.

2.2 Glauber model

The Glauber model is based on the geometrical configuration of the nuclei in order to estimate the initial spatial distribution just after the collision. It is a semiclassical model in which a nucleon of incident nucleus interacts with target nucleons with a given density distribution: the

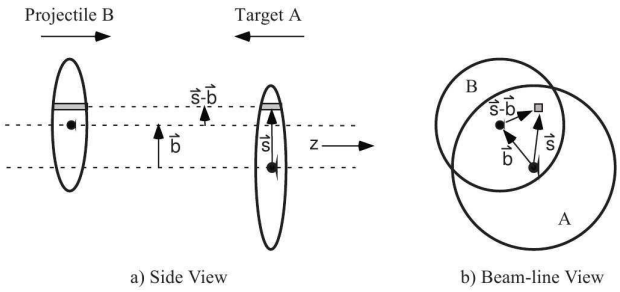

Figure 2.2: Representation of a collision between the nuclei A and B at a given impact parameter: (a) trasverse view, (b) longitudinal view

nucleus-nucleus collision are treated as multiple nucleon-nucleon interaction. The use of such a geometrical model is giustified by the fact that at high energies the De Broglie wave length of the nucleons are smaller with respect to the typical nuclear sizes. Moreover nucleons are assumed to travel in straight lines and are not deflected after the collision and according to eikonal approximation the multiple interaction can be considered as independent. Also, the nucleon-nucleon inelastic cross-section, σ_{NN}, is assumed to be the same as that in the vacuum. In order to describe the Glauber model we begin by introducing the nuclear overlap function $T_{AB}(\mathbf{b})$ [47]:

$$\hat{T}_{AB}(\mathbf{b}) = \int \hat{T}_A(s)\hat{T}_B(s-\mathbf{b})d^2s \tag{2.2}$$

where $\mathbf{b}$ is the impact parameter and s is the transverse coordinate; while $\hat{T}_A$ and $\hat{T}_B$ are the nuclear tickness functions that give the probability to find a nucleon per unit of transverse area and they are defined as:

$$\hat{T}_{A/B}(s) = \int \hat{\rho}_{A/B}(s, z_{A/B})dz_{A/B} \tag{2.3}$$

being $\hat{T}_{A/B}$ the nuclear mass number density normalized to mass number A or B, that in case of heavy ion is usually parametrized as a Wood Saxon distribution:

$$\rho = \frac{\rho_0}{1+\exp\left(\frac{r-R}{a}\right)}. \tag{2.4}$$

Through the nuclear thickness function and the nuclear overlap function it is possible to evaluate the number of binary nucleon nucleon collisions N_{coll} and the number of the participant nucleons N_{part}, that are both strongly related to the value of the impact parameter b.

$$N_{coll}(b) = AB \cdot \hat{T}_{AB}(b)\sigma_{inel}^{NN} \tag{2.5}$$

$$\begin{aligned} N_{part}(b) = A \int \hat{T}_A(s) \left\{ 1 - \left[1 - \hat{T}_B(s - \mathbf{b})\sigma_{inel}^{NN} \right]^B \right\} d^2s + \\ + B \int \hat{T}_B(s - \mathbf{b}) \left\{ 1 - \left[1 - \hat{T}_A(s)\sigma_{inel}^{NN} \right]^A \right\} d^2s \end{aligned} \tag{2.6}$$

The number of binary collisions and the number of participant cannot be directly measured in experiments but they are related to the charged particle multiplicity N_{ch} that is a measurable quantity. Exploiting the relation between b, N_{part} and N_{ch} it is possible to trace back to the impact parameter of the collision performing a subdivision of N_{ch} in terms of centrality classes. The relation between N_{ch} and N_{part} and b is shown in Fig 2.3.

The Glauber model can also be exploited to estimate the initial spatial distribution of partons in the transverse plane. In fact, if one do not perform the integration over s in Eq. 2.2 and in Eq. 2.6 obtain respectively the density profile in the transverse plane of the number of participant and that of the binary collision. Whose linear combination could well approximate the density profile in the transverse plane of the partons created in the heavy-ion collision.

2.3 Evolution of the heavy ions collisions

In this paragraph the different stages of the evolution of relativistic heavy-ion collisions will be described. In such collisions a hot and dense

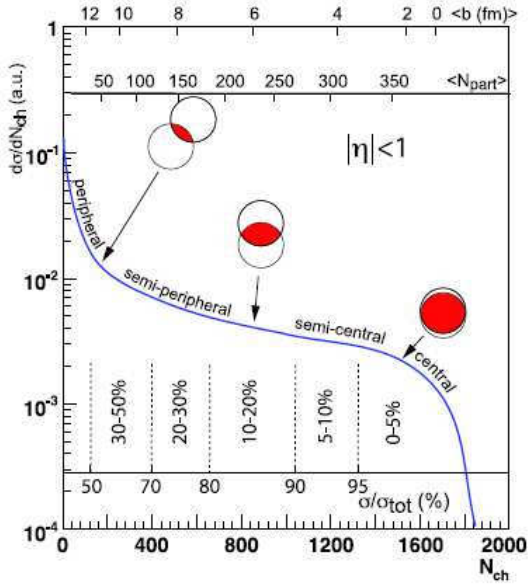

Figure 2.3: Cross section observed in function of N_{ch}. On the x-axes can be seen the relations between N_{ch}, N_{part} and b

matter, called *fireball*, will be created and subsequently cools and expands until it thermally freezes out and free-streaming hadrons reach the detector. In principle, a non-equilibrium dynamical theory of a heavy ion collision should be developed from the QCD lagrangian. Unfortunately, due to the large range of energies and densities reached, it is not possible to describe in a unified approach the whole evolution of a HIC, because it involves also low energy scale where the theory is in a non-perturbative regime. In literature two different approach have been proposed to describe the evolution of the fireball: the hydrodynamical and the kinetic approaches. The firs one is a macroscopic description of the problem where local equilibrium is assumed while the second one is a microscopical approach and it is also valid for non equilibrium stages. The dynamical evolution of the collision can be divided in different stages (Fig. 2.4):

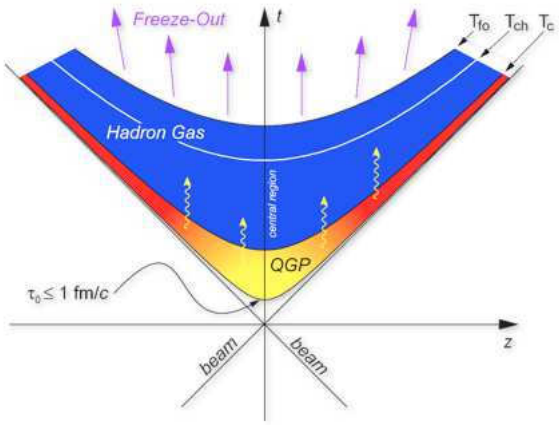

Figure 2.4: Schematic representation of the space time evolution of a ultra-relativistic collision between heavy ions as a function of time t and the longitudinal coordinate z (the collision axis). In this Minkowski-diagram the time variable which is used in the discussion in the text is the *proper time* $\tau = \sqrt{(t^2 - z^2)}$, which has a Lorentz-invariant meaning and is constant along the hyperbolic curves separating various stages in this figure.

- **Pre-equilibrium stage and thermalization**: The nuclei meet each other at the point (z,t)=(0,0). As we have said due to the Lorentz contraction the incoming nuclei are approximately transparent and thus they pass through each other. However, in the region of the collision is generated a strong color field, which causes an excitation of the vacuum and produces a dense pre-equilibrium matter consisting mostly of gluons and also of quark and anti-quark. This system takes about 1 fm/c to achieve the local thermalization and forms the quark gluon plasma. In this very early collision stage, the primary collisions between fast partons inside the colliding nuclei generate hard particles with either a large mass (m, Δ_{QCD}) or a large transverse momenta $p_T \gg 1GeV (p_T \gg T)$. Their creation involves large momentum transfer, therefore their production can be calculated in perturbative QCD using factorization theorems from the nuclear structure function.

  Hydrodynamic cannot be used to describe the pre-equilibrium phase

because it involves out of equilibrium processes. Hence, to describe the successive stages of evolution, using hydrodynamics, it is necessary to know the initial condition, for the energy and spatial density. Moreover is necessary to estimate the time τ_0 at which the system reaches the equilibrium. As regard the transport theory, it can be used also to describe the pre-equilibrium phase, once the initial spatial density distribution of the particles is known and is put as input. From these last considerations it seems clear that is important to know the initial condition of the just thermalized system. The initial energy density ϵ_0 can be estimated knowing the energy density released in the collision region (dE_T/dy), which is accessible if one measure the total energy of the final products collected in the detectors. The initial energy density negletting the work done by the pressure in the expansion is

$$\epsilon(0) = \frac{1}{\pi R_0^2 \tau_0} \frac{dE_T}{dy} \tag{2.7}$$

and the Bjorken estimate for RHIC is between 5 and 7 GeV/fm^3 [48], assuming an isoentropic expansion and neglecting the work needed by longitudinal expansion. Taking into account the expansion of the plasma, the previous estimation must be corrected to a value $\epsilon_0 \approx 10 \div 15\, GeV/fm^3$, this energy density is much greater than the critical energy density estimates by the lattice QCD. A further correction would be necessary if the expansion of the system were not iso-entropic and dissipation is taken in account.

- **QGP expansion**: Once the system has reached a kinetic equilibrium it is characterized by an energy density well above the critical energy density of the QCD phase transition ($\approx$1GeV/fm^3); at RHIC for example, this energy density is about 10$\div$15 GeV/fm^3 as previously said, and at LHC the energy density is $\approx$4$\div$5 ϵ_0^{RHIC}. Thus the system is expected to be in the quark gluon plasma phase. Actually

due to the predominant presence of gluons with respect to quarks, at the beginning of this phase the system is often considered as a gluon plasma (Glasma). Driven by thermal pressure gradients the QGP expands and cools down very quickly and the partons inside the bulk rescatter elastically and inelastically. In particular, the elastic collisions lead the system towards kinetic equilibrium, while inelastic collisions cause a change in the relative abundances of the different flavours of partons, leading the system towards chemical equilibrium [49, 50].

This phase of the evolution of QGP can be described by relativistic hydrodynamics or using kinetic theory. Historically the first and most simple approach proposed was the ideal hydrodynamic. In this approach, the equations of motion are obtained from the local conservations law for energy-momentum and baryon number:

$$\partial_\mu T^{\mu\nu}(x) = 0; \qquad \partial_\mu J^\nu_B = 0, \tag{2.8}$$

where $T^{\mu\nu}$ is the energy momentum tensor, that for a perfect fluid can be written as:

$$T^{\mu\nu}(x) = [\epsilon(x) + P(x)]\, u^\mu(x) u^\nu(x) - P(x) g^{\mu\nu} \tag{2.9}$$

where $u^\mu(x)$ is the four flow velocity and $g^{\mu\nu}$ is the metric tensor. In the local rest frame:

$$T^{00} = (\epsilon + P) - P = \epsilon, \qquad T^{ii} = -P \tag{2.10}$$

The additional equation necessary to solve the five equations 2.8 is the Equation of State (EoS) of the system that drives its evolution, in the form $P = P(\epsilon, \rho)$. In fact together with the EoS, the equations 2.8 form a closed system, that can be solved once the initial condition, i.e the energy density $\epsilon(x)$ and the velocity profile $u^\mu(x)$, have been specified. In recent years further improvment have been

proposed including viscous effect. In this approach the expression for the energy momentum tensor can be modified adding terms that enable to take into account the dissipative effect present in a viscous fluid. In fact it seems that the quark gluon plasma has a low but non zero shear viscosity η/s to entropy density ratio close to the conjectured lower boundary equal to $1/4\pi$, expected for system in the infinite coupling limit.

- **Hadronization and hadronic phase**: When the energy density reaches the critical value $\epsilon_c = 1\text{GeV/fm}^3$ partons hadronize. There are two different mechanism of hadronization: the fragmentation and the coalescence. In the first one each partons fragment into a jet of hadrons which carries a fraction of the momenta of the initial partons. This is the predominant way to hadronize in proton-proton collisions for partons with energy greater than 2 GeV.
  In HIC there are several indications that the mechanism of coalescence is dominant for producing hadrons up to p_T ≈5-6 GeV. It consists in the reconbination of two or three quarks that form respectively mesons or baryons [51].
  In the hadronic phase the hadrons keep rescattering to each other until the distance between them is larger than the range of strong interactions d_R ≈1 fm. Therefore at densities $\rho < d_R^3$ all scatterings stop and the hadrons decouple and free stream towards the detector; this is called *kinetic freeze-out*.
  In the Hydrodynamic description of the plasma the hadronization is introduced through a freeze-out algorithm (Cooper Frye formula) which stops the hydrodynamic evolution and translates the hydrodynamic output i.e energy density, baryon density and flow into hadron spectra, making use of the statistical model which can account correctly for hadronization of the bulk i.e $p_T \leq$2 GeV.

2.4 Principal observable probes for QGP

There are several suggestions at present to identify whether the matter produced in a high energy heavy ion collision is the Quark Gluon Plasma phase. One approach is to look for primordial remnants in the observed hadron features: discontinuities in the momentum distribution of the secondaries reflecting a first order phase transition or strangeness enhancement which is expected to be significantly larger if it arises from the QGP. Another usual suggestion is to look for signals produced at early times and are not affected by the subsequent hadronization. Possible observables of this type are thermal dileptons and thermal photons, which are emitted by the plasma and then escape.
In the same context, one may also study the effect of the produced dense medium on the observed production of heavy quark bound states, like J/ψ suppression or hard jets.
In the following a list of the principals observables of the QGP will be presented:

- **Global observables**: The rapidity distribution of particles dN/dy and transverse energy dE_T/dy allow for the determination of temperature, entropy, and energy density of the system created in a heavy-ion collision. These observables need to be compared to model calculations (lattice QCD calculations and so on), in order to investigate if the system may have reached the QGP phase.

- **Electromagnetic probes**: During the evolution of a nuclear collision are created photons and dileptons that can be used to probe the QGP. The importance of such probes is due to the fact that they do not interact through strong interaction and so there is a little possibility that they interact after their creation. Therefore these probes furnish information relative to the phase of the evolution in which they are originated. Unfortunately there are many

sources which can produces photons or dileptons, hence the analysis of such kind of observables is quite difficult.

- **Strangeness enhancement**: Enhancement of strangeness and antibaryon production is a frequently discussed signal, it is due to the reduction of the threshold for production of strange hadrons from $2m_K - 2m_\pi \approx 700$ MeV to $2m_s \approx 300$ MeV and baryon-antibaryon pairs from ≈ 2 GeV to almost zero. The strongest signal is obtained by considering strange antibaryons which combine both effects [52]. The enhanced strange quark production in deconfined quark-gluon plasma leads to chemical equilibrium abundances for all strange quarks. The strangeness abundance for hadronic matter in chemical equilibrium is smaller. This signal was first predicted as a consequence of the interaction between partons in the QGP [52]. It has indeed been observed at both the SPS and the RHIC energies.

- **J/Ψ suppression**: J/Ψ particles are bound states formed by a charm and an anticharm quark ($c\bar{c}$). They are produced mostly by the hard scatterings in the first stage of the collision. When they are created in p+p collisions, they can freely escape from the collision region. On the other hand, the J/Ψ produced in nucleus-nucleus collisions crosses the QGP and feels screening effects in the medium. Although the J/Ψ meson is a tightly bound particle, in a quark-gluon plasma environment the charm-anticharm potential is screened, like in the analogous phenomenon called Debye screening in QED. As a consequence, the interaction between the $\bar{c}$ and c quark is strongly weakened when $r_{\bar{c}c} > \lambda_D$, with λ_D the Debye screening lenght. For sufficently high density, λ_D is so small that the J/Ψ dissociates, leading to a suppression of the observed yield compared to p+p or p+nucleus collisions [53].

2.5 Anisotropic collective flow

One of the strongest pieces of evidence for the formation of a thermalized dense state of unconventional strongly interacting matter in ultra-relativistic nucleus-nucleus collisions stems from the strong anisotropic collective flow measured in non-central collision events [54].
Studies of the final charged particle momentum distributions have revealed strong collective effects in the form of anisotropies in the azimuthal distribution transverse to the direction of the colliding nuclei [55], and theory holds that their anisotropy around the beam axis in non-central collisions is established during the earliest stages of the evolution of the collision fireball [56]. This anisotropy has been interpreted as a result of pressure-driven anisotropic expansion (referred to as "*flow*") of the created matter. Flow signals the presence of multiple interactions between the constituents of the medium created in the collision. More interactions usually leads to a larger magnitude of the flow and brings the system closer to thermalization. The magnitude of the flow is therefore a detailed probe of the level of thermalization [57].

2.5.1 Definitions: the reaction and participant plane

Experimentally, the most direct evidence of flow comes from the observation of anisotropic flow which is the anisotropy in particle momentum distributions correlated with the so-called *reaction plane* (fig. 2.5).
This reaction plane is spanned by the vector of the impact parameter and the beam direction. Its azimuth is given by Ψ_{RP}. The particle azimuthal distribution measured with respect to the reaction plane is not isotropic, so it is customary to expand it in a Fourier series [58]:

$$E\frac{d^3N}{d^3p} = \frac{1}{2\pi}\frac{d^2N}{p_T dp_T dy}\left(1 + \sum_{n=1}^{\infty} 2v_n \cos\left[n\left(\phi - \Psi_{RP}\right)\right]\right), \qquad (2.11)$$

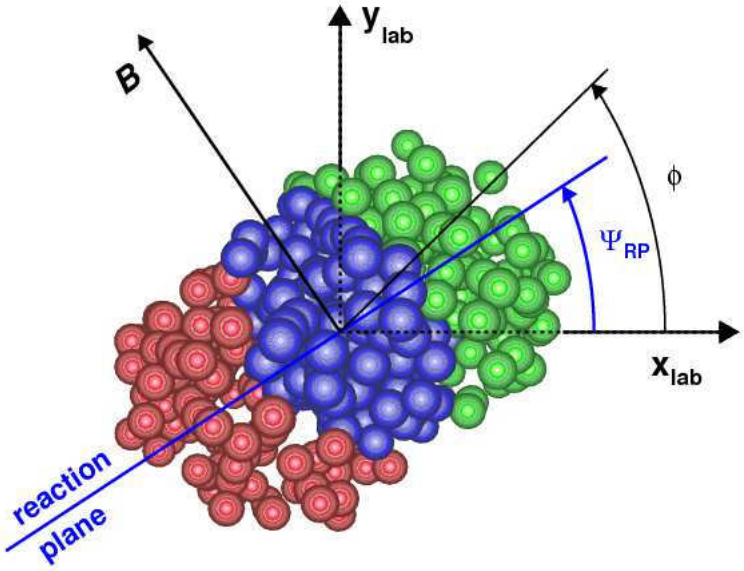

Figure 2.5: Schematic view of a collision of two heavy ions (the left one emerging from and the right one going into the page). Particles are produced in the overlap region (blue-colored nucleons). The azimuthal angles and the reaction plane are also depicted.

where E is the energy of the particle, p the momentum, p_T the trasverse momentum, ϕ the azimuthal angle, y the rapidity and Ψ_{RP} the reaction plane angle. The sine terms in such an expansion vanish because of the reflection symmetry with respect to the reaction plane. The Fourier coefficients are p_T and y dependent and are given by

$$v_n(p_T, y) = \langle \cos\left[n\left(\phi - \Psi_{RP}\right)\right] \rangle \,, \tag{2.12}$$

where the angular brackets denote the avarage over the particles, summed over all events, in the (p_T, y) bin under study. In this Fourier decomposition, the coefficient v_1 is known as directed flow, v_2 as elliptic flow, v_3 as triangular flow, v_4 as the fourth harmonic and so on.

The reaction plane cannot be directly measured in high energy nuclear collisions, but can be estimated from the azimuthal distribution event-by-event. Then the different harmonic flow coefficients are reconstructed from two or many particle azimuthal correlations. This introduces un-

certainty in the analysis as the azimuthal correlations are not determined solely by anisotropic flow but have other contributions, usually referred to as *nonflow* and in case of two-particle correlations quantified by parameters δ_n:

$$\langle \cos\left[n\left(\phi_i - \phi_j\right)\right]\rangle = \left\langle v_n^2 \right\rangle + \delta_n. \tag{2.13}$$

Anisotropic flow can fluctuate event to event both in magnitude and direction even at fixed impact parameter. This flow fluctuation can be described by

$$\sigma_{vn}^2 = \left\langle v_n^2 \right\rangle - \left\langle v_n \right\rangle^2. \tag{2.14}$$

One of the important sources of flow fluctuations is in the initial geometry of the overlapping region due to the random nature of the interaction between constituents of the two nuclei. The participants are those constituents which take part in the primary interaction. The principal axis of the so-called *participant zone* can deviate from the reaction plane. The axes of the participant coordinate system (PP), compared to the reaction plane system (RP) are shown in figure 2.6. It is important to distinguish between flow values measured in these two system: the values in the RP system being always smaller than in the PP system [59].

Moreover, the flow is determined by the initial density profile. Although its precise value depends on the detailed shape of the profile, most of the relevant information is encoded in the initial eccentricity of the overlap zone, ϵ [60]. The standard definition of the eccentricity is [61]

$$\epsilon = \frac{\langle y^2 - x^2 \rangle}{\langle y^2 + x^2 \rangle}, \tag{2.15}$$

where (x, y) is the position of a participant nucleon in the RP system. Also in this case, the angular brackets mean the avarage over participant nucleons and over many collision events at the same impact parameter. Because of the event-by-event fluctuations in the participant nucleon positions, the eccentricity driving flow in a given event is that defined by

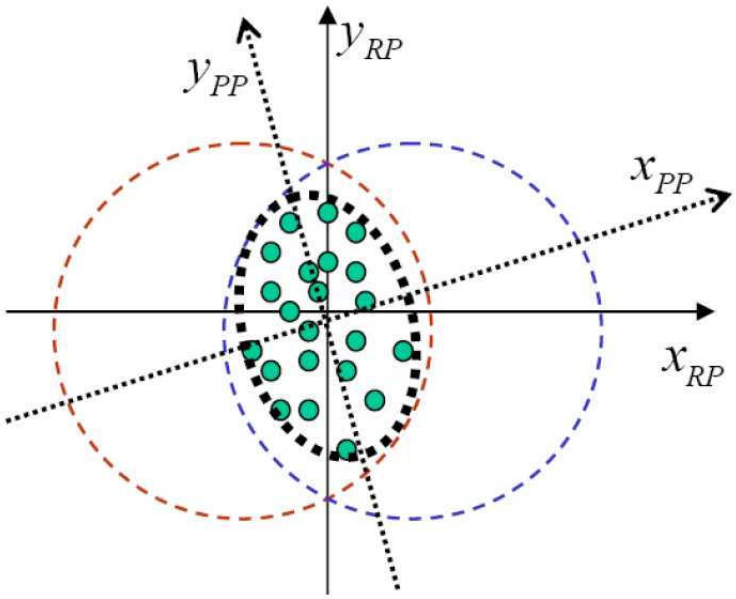

Figure 2.6: Schematic view of the participant and reaction planes with respect to the beam direction (z-axis). Due to fluctuations, the overlap zone could be shifted and tilted with respect to the RP frame. x_{PP} and y_{PP} are the principal axes of inertia of the dots.

the principal axes of the PP system. This *participant eccentricity* can be written as [54]

$$\epsilon_{part} = \frac{\sqrt{\langle r_T^n \cos(n\phi)\rangle^2 + \langle r_T^n \sin(n\phi)\rangle^2}}{r_T^n} \tag{2.16}$$

2.6 Experimental methods

Since the reaction plane is not known exactly on an event-by-event basis, v_n is measured indirectly using azimuthal correlations. Several methods have been used. In the following, we present a little summary of these methods.

2.6.1 Event plane method

In the standard event plane method one estimates the azimuthal angle of the reaction plane from the observed event plane angle determined from the anisotropic flow itself [62]. This is done for each harmonic, n, of the Fourier expansion. The event flow vector $\mathbf{Q_n}$ is a 2D vector in the transverse plane:

$$\begin{aligned} Q_{n,x} &= \sum_i w_i \cos(n\phi_i) = \mathbf{Q}_n \cos(n\Psi_n) \\ Q_{n,y} &= \sum_i w_i \sin(n\phi_i) = \mathbf{Q}_n \sin(n\Psi_n) \end{aligned} \tag{2.17}$$

where the sum goes over all particle i used in the event plane calculation. The quantities ϕ_i and w_i are the lab azimuthal angle and the weight for particle i, where for odd harmonics $w_i(-y) = w_i(y)$. The optimal choice for w_i is to approssimate $v_n(p_T, y)$. Since often $v_n(p_T, y)$ almost linearly increases with p_T, the transverse momentum is a common choice as a weight. The event plane angle is the azimuthal angle of $\mathbf{Q_n}$ calculated as

$$\Psi_n = \frac{1}{n} \arctan \frac{Q_{n,y}}{Q_{n,x}} = \frac{1}{n} \arctan \frac{\langle p_T \sin(n\phi) \rangle}{\langle p_T \cos(n\phi) \rangle} \tag{2.18}$$

The observed v_n is the n^{th} harmonic of the azimuthal distribution of particles with respect to this event plane:

$$v_n^{obs}(p_T, y) = \langle \cos[n(\phi_i - \Psi_n)] \rangle \,, \tag{2.19}$$

where angle brackets denote an average over all particles in all events with their azimuthal angle ϕ_i in a given rapidity and p_T momentum space bin at a fixed centrality. To remove auto-correlations one has to subtract the **Q**-vector of the particle of interest from the total event **Q**-vector, obtaining a Ψ_n to correlate with the particle.

Since finite multiplicity limits the estimation of the angle of the reaction plane, the v_n have to be corrected for the event plane resolution for each

harmonic given by

$$\mathcal{R}_n = \langle \cos[n(\Psi_n - \Psi_{RP})] \rangle \,, \tag{2.20}$$

where angle brackets denote an average over a large event sample. The final flow coefficients are

$$v_n = \frac{v_n^{obs}}{\mathcal{R}_n}. \tag{2.21}$$

By large event one means a large enough sample to obtain good averages, but small enough to avoid shifts in the beam position and/or detector response as a function of time.

2.6.2 Two-particle correlation

The pair-wise correlation method is based on the fit of the two-particle azimuthal distribution to that expected from anisotropic flow:

$$\frac{dN^{pairs}}{d\Delta\phi} \propto \left(1 + \sum_{n=1}^{\infty} 2v_n^2 \cos(n\Delta\phi)\right) \tag{2.22}$$

where all pairs of particles in a given momentum region are correlated. No event plane is used. Acceptance correlations are removed to first order by dividing by the mixed event distribution. The harmonic coefficients are small because they are the squares of the flow coefficients. This quantity is only for integrated quantities, but normally the integrated values are obtained by averaging the differential quantities.

The two-particle cumulants method differs from the previous one because instead of the fit to the two-particle distribution it calculates the coefficients directly as

$$v_n\{2\}^2 = \langle \cos[n(\phi_1 - \phi_2)] \rangle \tag{2.23}$$

for all pairs of particles.

Event plane method and two-particle cumulants are essentially equivalent [63].

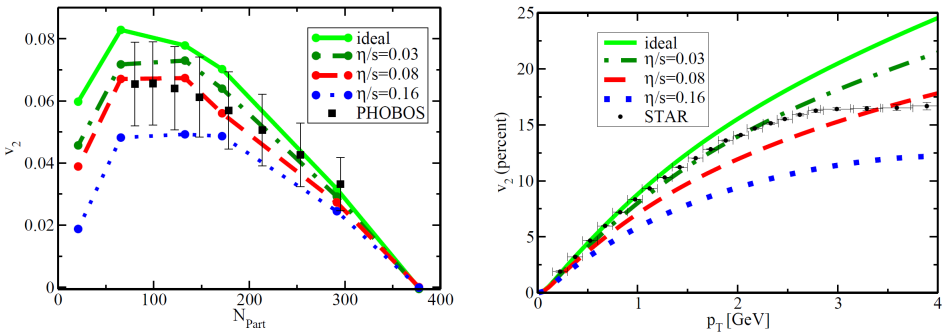

Figure 2.7: Experimental $Au+Au$ data on p_T integrated v_2 from RHIC compared to hydrodynamic model for various viscosity ratios η/s as presented in [64].

2.7 Viscous effect

Historically one of the most important result from the $Au + Au$ collisions at RHIC was the observation of large elliptic flow $v_2(p_T)$ for $p_T \leq 2\,GeV$. The comparison of the centrality and p_T dependence of v_2 with the ideal hydrodynamics calculations and the experimental results had led to the conclusion that the matter created in these collision behaves like a perfect fluid.

A more through study joined to more precise experimental data shows that the elliptic flow produced was smaller than the ideal hydrodynamic calculation. This deviation was due to the breakdown of the local equilibrium hypothesis. Further improvement have been done with the inclusion of viscous effect and the develop of viscous hydrodynamics.

The comparison between the experimental results and the viscous hydrodynamics calculations (shown in fig. 2.7) confirmed that the matter created had a very small viscosity with an $\eta/s \approx 1/4\pi$ [64].

Known good fluids in nature have an η/s of order $\hbar/k_B$. In a strongly coupled $\mathcal{N} = 4$ supersymmetric Yang Mills theory with a large number of colors ('t Hooft limit), η/s can be calculated using a gauge gravity duality and this gives [65]:

$$\frac{\eta}{s} = \frac{\hbar}{4\pi k_B} \tag{2.24}$$

Kovtun, Son and Starinets [65] conjectured, using the AdS/CFT correspondence, that this implies that all fluids have $\eta/s \geq \hbar/4\pi k_B$ (the KSS bound). Therefore a fluid with $\eta/s = 1/4\pi$ (in natural units) is very close to a perfect fluid. The KSS bound raises the interesting question on how fundamental this value is in nature and if the QGP behaves like an almost perfect fluid. It is argued that the transition from hadrons to quarks and gluons occurs in the vicinity of the minimum in η/s, just as is the case for the phase transitions in helium, nitrogen, and water. An experimental measurement of the minimal value of η/s would thus pinpoint the location of the transition [66].

However, small value of $\eta/s \sim 1/4\pi$ is not an evidence of the creation of a QGP phase. A phenomenological estimation of its temperature dependence could give information if the matter created in these collisions undergoes a phase transition [66, 67].

There are several theoretical indications that η/s should have a particular behavior with the temperature [66, 67, 70–73]. As an example in Fig. 2.8 it is shown a collection of theoretical results about the temperature dependence of η/s. Figure 2.8 shows that in general η/s should have a typical behavior of phase transition with a minimum close to the critical temperature T_C [66, 67].

On one hand at low temperature estimations of η/s performed in the chiral perturbation theory for a meson gas [70, 71], have shown that in general η/s is a decreasing function with the temperature, see down-triangles in Fig. 2.8. Similar results for η/s have been extrapolated from heavy-ion collisions at intermediate energies, see HIC-IE diamonds in Fig. 2.8. On the other hand at higher temperature $T > T_C$ lQCD calculation have shown but with large error bars that in general η/s becomes an increasing function with the temperature [72], see up-triangles and circles in Fig. 2.8.

In general due to the large error bars in the lQCD results for η/s it is not

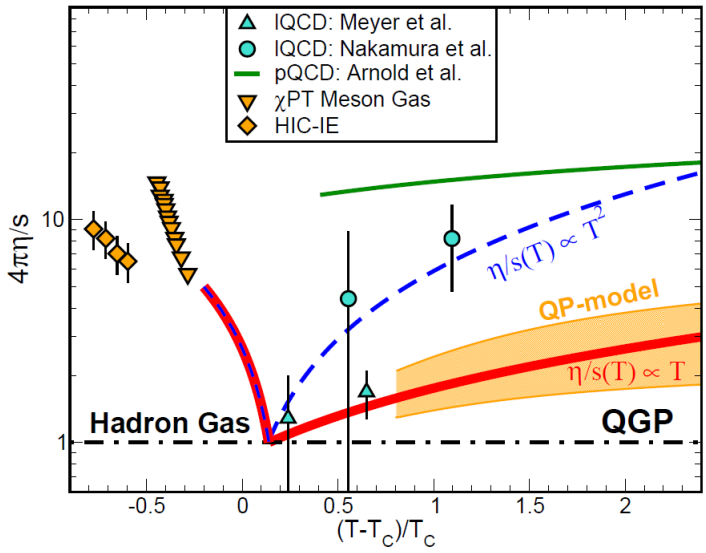

Figure 2.8: Different parametrizations for η/s as a function of the temperature. The orange area refers to the quasi-particle model predictions for η/s [68]. The different lines indicate different possible T dependencies while green line represents the result for the pQCD calculation [69]. Symbols are as in the legend. See the text for more details.

possible to infer a clear temperature dependence in the QGP phase. The analysis at different energies of $v_2(p_T)$ and the extension to high order harmonics $v_n(p_T)$ can give further information about the T dependence of η/s.

The comparison between event-by-event viscous hydrodynamical calculations and the experimental results for v_n seems to confirm a finite but not too large value of $4\pi\eta/s \sim 1-3$ (as shown in figure 2.9) [74, 75].

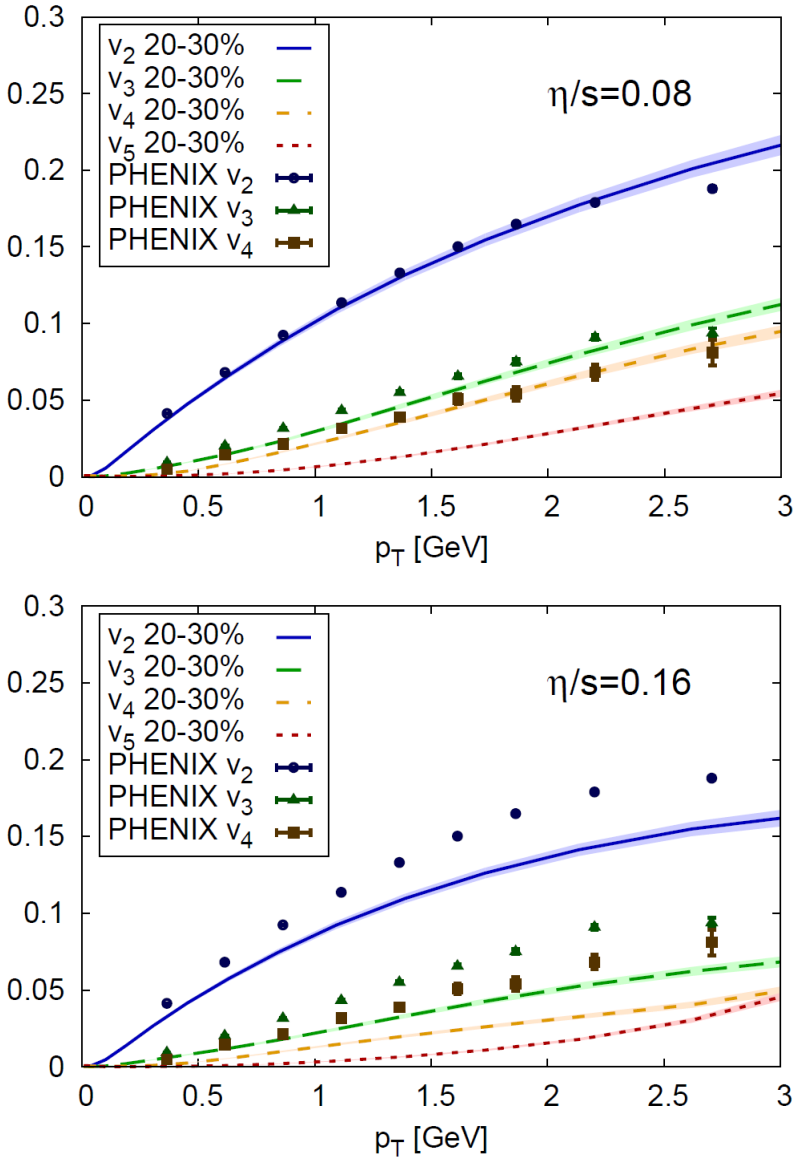

Figure 2.9: Viscous hydrodynamic calculations for $v_n(p_T)$ with $\eta/s = 0.08$ (upper panel) and $\eta/s = 0.16$ (lower panel) compared with experimental RHIC data [74].

CHAPTER 3

TRANSPORT THEORY

Contents

In order to describe the Quark Gluon Plasma created in ultra-relativistic heavy ion collisions, we use in this work an effective transport theory that permits to study a system evolving dynamically. In this chapter will be discussed the main features of transport theory, from its classical formulation up to its application to field theory. Moreover, the solution

of the relativistic Boltzmann equation for the parton distribution function tuned at a fixed shear viscosity to entropy density ratio η/s will be analyzed.

3.1 Classical transport theory

In the classical kinetic theory, one considers a system composed by N particles inside a box of volume V colliding each other with a cross section σ. In such a system the probability to find a particle in a phase space element at the position x and momentum p is defined by:

$$f(\mathbf{x},\mathbf{p})d^3xd^3p \tag{3.1}$$

where $f(\mathbf{x},\mathbf{p})$ is the phase space density, basic element of the kinetic theory. To point out that the N particles must be inside the V volume one may normalize the function in the following way:

$$\int_V f(\mathbf{x},\mathbf{p})d^3xd^3p = N. \tag{3.2}$$

While the spatial density of the system can be calculated performing an integration over p:

$$\rho(\mathbf{x}) = \int f(\mathbf{x},\mathbf{p})d^3p. \tag{3.3}$$

Moreover trought the distribution function is possible to calculate the average of a physical observable $O(\mathbf{x},\mathbf{p})$:

$$\langle O(\mathbf{x})\rangle = \frac{1}{N}\int O(\mathbf{x},\mathbf{p})f(\mathbf{x},\mathbf{p})d^3pd^3x. \tag{3.4}$$

The aim of the kinetic theory is to describe the evolution of the distribution function for a certain interaction. In order to do this, our first task is to find an equation of motion for this distribution function. Considering the simplest case in which collisions are switched off ($\sigma = 0$), at time t a particle have coordinates (**x**,**p**). After a certain time $t + \delta t$, the same particle will have coordinates ($\mathbf{x} + \mathbf{v}\delta t$,$\mathbf{p} + \mathbf{F}\delta t$), where $\mathbf{F}$ is an external force applied on the particle and $\mathbf{v} = \mathbf{p}/m$ is the velocity. In this way, all the particles inside the volume d^3xd^3p around (**x**,**p**) at time t, will be found in the volume $d^3x'd^3p'$ around ($\mathbf{x} + \mathbf{v}\delta t$,$\mathbf{p} + \mathbf{F}\delta t$) at time $t + \delta t$. Hence, in the case of no collisions, we have:

$$f(\mathbf{x} + \mathbf{v}\delta t, \mathbf{p} + \mathbf{F}\delta t)d^3x'd^3p' = f(\mathbf{x},\mathbf{p})d^3xd^3p \tag{3.5}$$

which, in case of forces that depending only from position, reduces to

$$f(\mathbf{x}+\mathbf{v}\delta t, \mathbf{p}+\mathbf{F}\delta t) = f(\mathbf{x},\mathbf{p}). \tag{3.6}$$

Expanding the left-hand side to the first order in δt, we obtain the equation of motion for the distribution function as we let $\delta t \to 0$:

$$\left(\frac{\partial}{\partial t} + \frac{\mathbf{p}}{m}\cdot\nabla_{\mathbf{x}} + \mathbf{F}\cdot\nabla_{\mathbf{p}}\right) f(\mathbf{x},\mathbf{p}) = 0, \tag{3.7}$$

while, when there are collisions ($\sigma > 0$), the eq. 3.6 must be modified as:

$$f(\mathbf{x}+\mathbf{v}\delta t, \mathbf{p}+\mathbf{F}\delta t) = f(\mathbf{x},\mathbf{p}) + \mathcal{C}[f], \tag{3.8}$$

where $\mathcal{C}[f]$ is a functional of the distribution function f, called collision integral, and it takes into account the change of the function f due to the collisions. Also in this case, expanding the left-hand side to the first order in δt, one obtains:

$$\left(\frac{\partial}{\partial t} + \frac{\mathbf{p}}{m}\cdot\nabla_{\mathbf{x}} - \nabla\mathcal{U}\cdot\nabla_{\mathbf{p}}\right) f(\mathbf{x},\mathbf{p}) = \mathcal{C}[f] \tag{3.9}$$

where we have considered the force as derivable from a potential $\mathcal{U}$.
An explicit form of $\mathcal{C}[f]$ can be obtained taking into account the number of particles that get into or are removed from the volume element during the time interval δt. This statement may be expressed in the form:

$$\mathcal{C}\delta t = \left(\bar{R} - R\right)\delta t, \tag{3.10}$$

where $R\delta t d^3x d^3p$ represents the number of collision occurring during the time between t and $t+\delta t$ in which one of the initial particles is in $d^3x d^3p$ around ($\mathbf{x}$,$\mathbf{p}$) while $\bar{R}\delta t d^3x d^3p$ is the same number in which one of the final particles is in $d^3x d^3p$ around ($\mathbf{x}$,$\mathbf{p}$) [76].

3.1.1 Collision term derivation

To derive an explicit form of the collision term we neglect the possibility that three or more particles may collide simultaneously, so we

assume that only binary collisions need be taken into account. Moreover the effect of external forces on collisions are ignored.
With this assumption we can simply define a collision as a transition from the initial state to a set of final states. For final states in the infinitesimal momentum-space element $d^3p_1' d^3p_2'$ the transition rate is:

$$dP_{12\to 1'2'} = d^3p_1' d^3p_2' \delta^4(P_f - P_i)|\mathcal{M}_{fi}|^2 \tag{3.11}$$

where $\mathcal{M}_{fi}$ is the transition amplitude of the process and the function $\delta^4(P_f - P_i)$ enforce momentum-energy conservation and is defined as:

$$\delta^4(P_f - P_i) \equiv \delta^3(\mathbf{P} - \mathbf{P}')\delta(E - E'). \tag{3.12}$$

The number of transition $12 \to 1'2'$ in a volume element d^3x at $\mathbf{x}$, owing to collisions during the time interval δt is:

$$dN_{12} dP_{12\to 1'2'} \delta t \tag{3.13}$$

where dN_{12} is the initial number of colliding pairs $(\mathbf{p}_1, \mathbf{p}_2)$. The two-particle correlation function is introduced by:

$$dN_{12} = \hat{f}(\mathbf{x}, \mathbf{p}_1, \mathbf{p}_2) d^3x d^3p_1 d^3p_2. \tag{3.14}$$

Thus, using eq. 3.11 and the notation described above, we obtain:

$$R = \int d^3p_2 d^3p_1' d^3p_2' \delta^4(P_f - P_i)|\mathcal{M}_{fi}|^2 \hat{f}(\mathbf{x}, \mathbf{p}_1, \mathbf{p}_2) \tag{3.15}$$

and similarly for $\bar{R}$ we have:

$$\bar{R} = \int d^3p_2 d^3p_1' d^3p_2' \delta^4(P_i - P_f)|\mathcal{M}_{if}|^2 \hat{f}(\mathbf{x}, \mathbf{p}_1', \mathbf{p}_2') \tag{3.16}$$

Finally, taking into account that the δ functions in the above equations are identical and that $|\mathcal{M}_{fi}| = |\mathcal{M}_{if}|$, we find for the collision term:

$$\mathcal{C}[f] = (\bar{R} - R) = \int d^3p_2 d^3p_1' d^3p_2' \delta^4(P_f - P_i)|\mathcal{M}_{if}|^2 \left(\hat{f}_{1'2'} - \hat{f}_{12}\right). \tag{3.17}$$

The expression we obtained is exact but it contains the unknown correlation function $\hat{f}$. So that, we now introduce the crucial assumption:

$$\hat{f}(\mathbf{x}, \mathbf{p}_1, \mathbf{p}_2) \approx f(\mathbf{x}, \mathbf{p}_1) f(\mathbf{x}, \mathbf{p}_2). \tag{3.18}$$

This says that the momenta of two particles in the volume element d^3x are uncorrelated, so that the probability of finding them simultaneously is the product of the probability of finding each alone. This is known as the *assumption of molecular chaos*, introduced firstly by Boltzmann. It allows to obtain a closed form for the Boltzmann transport equation:

$$\left(\frac{\partial}{\partial t} + \frac{\mathbf{p}_1}{m} \cdot \nabla_x - \nabla_x \mathcal{U} \nabla_p\right) f_1 = \int d^3p_2 d^3p_1' d^3p_2' \delta^4(P_f - P_i) |\mathcal{M}_{fi}|^2 (f_2' f_1' - f_2 f_1) \tag{3.19}$$

which is a nonlinear integro-differential equation for the distribution function [76].

3.2 Relativistic transport theory

In the relativistic case of the kinetic theory, the distribution function $f(x, p)$ is a Lorentz scalar where x represents the spacetime coordinates ($x = x^\mu = (t, \mathbf{x})$) and the components of the four-momentum $p = p^\mu = (p^0, \mathbf{p})$ obey to the mass shell condition $p^0 = \sqrt{\mathbf{p}^2 + m^2}$ [77].
Considering the relativistic formalism, the distribution function can be expressed with the following formula:

$$f(x, p) = \sum_{i=1}^{N} \delta^{(4)}(x_i(t) - x) \delta^{(4)}(p_i(t) - p). \tag{3.20}$$

The temporal evolution of the phase space density is described by the Liouville's theorem which states that in absence of dissipative force the phase space density is a constant of motion i.e. $df(x, p)/dt = 0$. Starting from this theorem is possible to derive the equation of motion for $f(x, p)$

as follows [78]:

$$\frac{d}{dt}f(x,p) = \sum_{i=1}^{N}\left[\frac{dx_i^\mu}{dt}\frac{\partial}{\partial x_i^\mu} + \frac{dp_i^\mu}{dt}\frac{\partial}{\partial p_i^\mu}\right]\delta^4(x_i(t)-x)\delta^4(p_i(t)-p) = \\ = \left(\frac{1}{m}p^\mu\frac{\partial}{\partial x^\mu} + F^\mu(x)\frac{\partial}{\partial p^\mu}\right)f(x,p) \tag{3.21}$$

where $F^\mu(x)$ denotes an external or a selfconsistent internal four-force. This equation is the relativistic Vlasov equation that in the non-relativistic limits becomes:

$$\left(\frac{\partial f}{\partial t} + \frac{\mathbf{p}}{m}\cdot\nabla_{\mathbf{x}} + \mathbf{F}\cdot\nabla_{\mathbf{p}}\right)f(\mathbf{x},\mathbf{p}) = 0. \tag{3.22}$$

The Vlasov equation is appropriate for a system in which there are only conservative forces but does not take into account dissipative effects that arise to incorporate some two body correlation in the one body treatment. In presence of two body scatterings in fact the phase space density is no more a constant of motion but changes as a consequence of the collisions. Making this consideration is possible to derive the equation of motion for $f(x,p)$ adding a collision term $\mathcal{C}[f]$. One obtains in this way the Boltzmann-Vlasov equation:

$$\left[\frac{1}{m}p^\mu\frac{\partial}{\partial x^\mu} + F^\mu(x)\frac{\partial}{\partial p^\mu}\right]f(x,p) = \mathcal{C}[f](x,p) \tag{3.23}$$

The collision term could be derived rigorously by mean of the BBGKY hierarchy (BogoliubovBornGreenKirkwoodYvon hierarchy) or it can be written for the case of a two-body collisions, see next paragraph. Its effect can be studied also by mean of a phenomenological ansatz taking the dissipation into account:

$$\mathcal{C}[f] \cong \frac{f - f_0}{\tau_r} \tag{3.24}$$

where τ_r denotes the relaxation time parameter and f_0 the equilibrium one-body distribution function, towards which the system will relax.

If effects of quantum statistics are neglected the equilibrium solution of the Boltzmann equation is given by the *Jüttner distribution*:

$$f_0(x,p) \equiv \exp\left[-\beta(p\cdot u+\mu)\right] \tag{3.25}$$

where the local parameters $[\beta \equiv 1/T, u^\mu, \mu](x)$ denote the inverse temperature, flow four-velocity and chemical potential, respectively. When quantum effects are included the exponential Boltzmann is replaced by the Fermi-Dirac or Bose-Einstein distribution, depending on the nature of the considered particles.

3.2.1 Collision integral

As we have seen, the Vlasov equation does not take into account dissipative effects that arise from the collisions between particles. In order to consider such scatterings it is necessary to add the collision term that when only the two body collision processes are considered is indicated with $\mathcal{C}_{22}$. Assuming that there are no particle correlations before each collision (molecular chaos), the $\mathcal{C}_{22}$ is related to the product of the phase space densities of the colliding particles, and is given by [79]

$$\begin{aligned}\mathcal{C}_{22} =& \frac{1}{2E_1}\int\frac{d^3p_2}{(2\pi)^3 2E_2}\frac{1}{\nu}\int\frac{d^3p_1'}{(2\pi)^3 2E_1'}\frac{d^3p_2'}{(2\pi)^3 2E_2'}f_1'f_2' \\ &\times|\mathcal{M}_{1'2'\to 12}|^2(2\pi)^4\partial^4(p_1'+p_2'-p_1-p_2) - \frac{1}{2E_1} \\ &\times\int\frac{d^3p_2}{(2\pi)^3 2E_2}\frac{1}{\nu}\int\frac{d^3p_1'}{(2\pi)^3 2E_2'}\frac{d^3p_2'}{(2\pi)^3 2E_2'}f_1f_2 \\ &\times|\mathcal{M}_{12\to 1'2'}|^2(2\pi)^4\partial^4(p_1+p_2-p_1'-p_2'),\end{aligned} \tag{3.26}$$

where $\nu = 2$ if one considers identical particles, to avoid double counting, otherwise $\nu = 1$. $|\mathcal{M}_{f\to i}|^2$ is the invariant amplitude matrix for a specific scattering process. Beyond the hypothesis of the molecular chaos it is assumed that the collisions are local in the x-space.

3.3 Quantum transport theory

The transport theory can be extended also to the quantum mechanics. In order to find the analogous of such equations in quantum theory it is necessary to define a quantity that can play the same role of $f(x,p)$. This quantity is the Wigner function $f_w(x,p)$ that is defined as [80]

$$f_w(x,p) = \int \frac{dy}{2\pi\hbar} e^{-ipx/\hbar} \langle x_+|\hat{\rho}|x_-\rangle \tag{3.27}$$

where $x_\pm = x \pm y/2$. The above equation using the explicit expression for the density operator $\rho = |\psi\rangle\langle\psi|$ becomes for pure states:

$$f_w(x,p) = \int \frac{dy}{2\pi\hbar} e^{-ipx/\hbar} \Psi^*(x_+)\Psi(x_-) \tag{3.28}$$

In analogy to the phase space function, the Wigner function allows to obtain the probability distributions in x and p variable, as indicated in the following expressions:

$$\rho(x) = \int f_w(x,p,)dp \qquad \rho(p) = \int f_w(x,p)dx \tag{3.29}$$

Once the Wigner function has been defined one can obtain the quantum version of the Vlasov equation simply performing a Wigner transformation of the Schroedinger equation or, equivalently, as shown in the following performing a Wigner transformation of the Heisenberg equation. Therefore one starts from the equation of motion for the density operator

$$\frac{\partial\hat{\rho}}{\partial t} = \left[\hat{\rho}, \hat{H}\right] \tag{3.30}$$

with $\hat{H} = \hat{p}^2/2m + \hat{U}$; making the Wigner transformation

$$\int \frac{dy}{2\pi\hbar} e^{-ipx/\hbar} \left\langle x_+ \left| \left(\frac{\partial\hat{\rho}}{\partial t} - \left[\hat{\rho}, \frac{\hat{p}^2}{2m} + \hat{U}\right]\right)\right| x_- \right\rangle = 0 \tag{3.31}$$

and after some calculations one gets the equation of motion for the Wigner function:

$$\frac{\partial f_w}{\partial t} + \frac{p}{m}\frac{\partial f_w}{\partial x} + \sum_{k=0} \frac{1}{(2k+1)!} \left(\frac{\hbar}{2}\right)^{2k} U(x) \left(\vec{\nabla}_x \cdot \vec{\nabla}_p\right)^{2k+1} f_w(x,p) = 0. \tag{3.32}$$

No approximation has been made to find this equation and it is exactly equivalent to the Heisenberg equation or to the Schroedinger equation. If the gradient of the potential is not too strong the summation over k index can be truncated at the first term and the previous equation become:

$$\frac{\partial f_w}{\partial t} + \frac{\mathbf{p}}{m}\frac{\partial f_w}{\partial x} + \vec{\nabla}_x U \cdot \vec{\nabla}_p f_w = 0 \tag{3.33}$$

that has the same form of the classical transport equation but it is here for the Wigner functions. In case of collisions, one can also add the collision integral.

3.4 Transport theory in relativistic quantum field theory

The extension of the Wigner function formalism to quantum field theory brings to a 4×4 matrix as indicated in the following expression

$$[\hat{F}(x,p)]_{\alpha\beta} = \int \frac{d^4y}{(2\pi\hbar)^4} e^{\frac{ipy}{\hbar}} \left\langle : \bar{\Psi}_\beta(x_+)\Psi_\alpha(x_-) : \right\rangle \tag{3.34}$$

where α and β are indices for spin and flavor; $\Psi(x)$ is the field and the colons denote normal ordering.

According to the Clifford algebra, the Wigner function $\hat{F}(x,p)$ can be decomposed as:

$$\hat{F}(x,p) = F(x,p) + \gamma_\mu F^\mu(x,p) + \frac{1}{2}\sigma_{\mu\nu}F^{\mu\nu}(x,p) + \gamma^5 A(x,p) - \gamma^5\gamma_\mu A^\mu(x,p). \tag{3.35}$$

The components are all real, except $A(x,p)$ which is purely imaginary, and are related to the scalar, vector, tensor, pseudoscalar and pseudovector densities respectively. The pseudoscalar and axial-vector parts of $\hat{F}(x,p)$ vanish for the case of locally spin-saturated system as demonstrated in [81], while the tensor part can be neglected in the classical limit as shown in [82]. Thus the Wigner matrix can be simply decomposed in terms of a scalar and a vector part as:

$$\hat{F}(x,p) = F_S(x,p) + \gamma_\mu F_V^\mu(x,p). \tag{3.36}$$

The procedure to derive the transport equation i.e. the equation of motion for the Wigner function is similar to that used in the previous section in order to derive the transport equation in quantum mechanics. Thus one has to do a Wigner transformation of the field's equation of motion. Taking into account a system described by a fermionic field which interacts trough a scalar field, the Lagrangian of such a system is

$$\mathcal{L} = \bar{\psi}(x)\left[i\gamma_\mu\partial^\mu - g_s\sigma\right]\psi(x) - \frac{1}{2}m_s^2\sigma^2 \tag{3.37}$$

from the lagrangian we derive the equation of motion for the fermionic fields:

$$\left[i\gamma_\mu\partial^\mu - (g_s\sigma)\right]\psi(x) = 0. \tag{3.38}$$

At this point one makes the Wigner transformation of the equation of motion [83, 84] obtaining

$$\int \frac{d^4y}{(2\pi\hbar)^4} e^{-\frac{ipy}{\hbar}}\bar{\Psi}_\beta(x_+)\left[i\gamma_\mu\partial^\mu - (m - g_s\sigma)\right]\Psi_\alpha(x_-) = 0 \tag{3.39}$$

and after some operations one gets

$$(\gamma{\cdot}p - \frac{i}{2}\gamma{\cdot}\partial - m)_{\beta\rho}\hat{F}_{\rho\alpha}(x,p) + \int \frac{d^4y}{(2\pi\hbar)^4} e^{-\frac{ipy}{\hbar}}\left\langle :\bar{\Psi}_\beta(x_+)\Psi_\alpha(x_-)\sigma(x_-): \right\rangle = 0 \tag{3.40}$$

This equation is exactly equivalent to the Dirac equation 3.38. However to derive the usual expression of the quantum relativistic transport equation one makes two approximations. In fact the evaluation of the integrals in eq. 3.40 is considerably simplified if one uses the mean field approximation treating the scalar field as a classical function and thus keeping it out from the expectation value. Moreover using the so called semi-classical approximation the field can be expanded in a Taylor series at the space time x and, if its gradient is not too large, is reasonable to stop the expansion at the first order getting

$$\sigma(x_-) = \sigma(x) - \frac{y^\mu}{2}\partial_\mu^x\sigma(x) \tag{3.41}$$

if one substitute this semiclassical approximation in eq. 3.40:

$$\left[\frac{i}{2}\gamma\cdot\partial+\gamma\cdot p-m^*(x)+\frac{i}{2}\partial_x^\mu\sigma(x)\partial_\mu^p\right]\hat{F}(x,p)=0 \tag{3.42}$$

where m^* is the effective mass ($m^* = m - \sigma(x)$). The equation 3.42 corresponds to two different equations: one for the imaginary part and the other one for the real part. For this last one has:

$$\left[\gamma\cdot p-m^*(x)\right]\hat{F}(x,p)=0 \tag{3.43}$$

while for the imaginary part we have:

$$\left[\gamma_\mu\partial^\mu-m^*(x)\partial_x^\mu m^*(x)\partial_p^\mu\right]\hat{F}(x,p)=0. \tag{3.44}$$

In the real part is contained the mass shell condition.
Making use of the decomposition of $\hat{F}(x,p)$ into scalar and vector components as shown in eq. 3.36, writing all in terms of the scalar part $F_s(x,p)$ and using the relation between the latter and the one-body phase space distribution $f(x,p) = F_s(x,p)/M(x)$ one obtains:

$$\left[p^\mu\partial_\mu+m^*(x)\partial_\mu m^*(x)\partial_p^\mu\right]f(x,p)=0 \tag{3.45}$$

that is the Vlasov equation for a system of fermions that interact through a scalar field σ.
Finally, adding the collision integral, one has an equation describing the motion of particles considering both the collisions acting at short range and the mean field that accounts for the long range physics:

$$\left[p^\mu\partial_\mu+m^*(x)\partial_\mu m^*(x)\partial_p^\mu\right]f(x,p)=\mathcal{C}[f](x,p). \tag{3.46}$$

3.5 Kinetic approach at fixed shear viscosity to entropy density ratio

In this section we introduce a transport approach in which it is possible to fix the η/s ratio. The motivation to develop such a transport

approach is twofold: from one hand, in this way it is possible to have a direct link with viscous hydrodynamic calculations and therefore it is possible to have an estimation of the viscosity of the plasma. On the other hand we have a kinetic approach which is valid in a wider range of transverse momentum p_T and η/s ratio. In particular in this way it is possible to include in a self consistent way the effect of the kinetic freeze out.

In order to study the dynamical evolution of the fireball with a certain $\eta/s(T)$ we determine locally in space and time the total cross section σ_{tot} needed to have the wanted local viscosity.

In the Chapmann-Enskog theory and for a pQCD inspired cross section, typically used in parton cascade approaches [79, 85–90], with $d\sigma/dt \sim \alpha_s^2/(t-m_D^2)^2$, the η/s is given by the following expression:

$$\eta/s = \frac{1}{15}\langle p\rangle\tau_\eta = \frac{1}{15}\frac{\langle p\rangle}{g(a)\sigma_{tot}\rho} \tag{3.47}$$

where $a = m_D/2T$, with m_D being the screening mass regulating the angular dependence of the cross section, while $g(a)$ is the proper function accounting for the pertinent relaxation time $\tau_\eta^{-1} = g(a)\sigma_{tot}\rho$ associated to the shear transport coefficient and in the function $g(a)$ it is encoded the information about the anisotropy of the collision. The function $g(a)$ is given by:

$$g(a) = \frac{1}{50}\int dy y^6 \left[(y^2+\frac{1}{3})K_3(2y) - yK_2(2y)\right] h\left(\frac{a^2}{y^2}\right), \tag{3.48}$$

where K_n-s are the Bessel functions and the function h relate the transport cross section to the total cross section

$$\sigma_{tr}(s) = \sigma_{tot}\, h(m_D^2/s) \tag{3.49}$$

with

$$h(\zeta) = 4\zeta(1+\zeta)\big[(2\zeta+1)ln(1+1/\zeta) - 2\big]. \tag{3.50}$$

Therefore the total cross section is evaluated locally by mean the Eq.3.47, and the effective total cross section is given by:

$$\sigma_{tot} = \frac{1}{15}\langle p\rangle\tau_\eta = \frac{1}{15}\frac{\langle p\rangle}{g(a)\eta/s\rho}. \tag{3.51}$$

From this approach is clear that at lower temperature, where it is expected the increase of η/s toward the value estimated for hadron gas $\eta/s \approx 6-7$, it permits a smooth realization of the kinetic f.o..

3.6 Numerical implementation of the transport equation

To solve the transport equation we use the so called test particle method, introduced by Wong [91] and used in almost all transport calculations [87, 88, 92–94]. In this method the phase space distribution function is sampled by mean of a large number of so called *test particles*. Usually the test particles are to be chosen point-like, i.e δ function in coordinates and momenta space, hence the phase space distributions can be written as a sum of the δ test particle distribution:

$$f(\mathbf{x},\mathbf{p}) = \omega\sum_{i=1}^{N_{test}}\delta^3(\mathbf{x}-\mathbf{x}_i)\delta^3(\mathbf{p}-\mathbf{p}_i) \tag{3.52}$$

where $\mathbf{x}_i$ and $\mathbf{p}_i$ indicate respectively the position and the momentum of the i-th test particle; N_{test} is the total number of test particles; while ω is a renormalization factor that is related to the real number of particles, N_{real}, so that the integral over coordinates and momenta space of the phase space distribution is equal to the total number of actual particles:

$$\int d^3x\int\frac{d^3p}{(2\pi)^3}f(\mathbf{x},\mathbf{p}) = \frac{\omega}{(2\pi)^3}N_{test} = N_{real} \tag{3.53}$$

hence $(2\pi)^3/\omega$ is equal to the number of test particles per real particles. Once the test particles have been introduced, the solution of the transport equation reduces to solve the classical equation of motion for the

test particles as will be described in the following. In fact, it can be shown, with the help of the Liouville theorem, that the phase space distribution given as a collection of point like test particles is a solution of the Boltzmann-Vlasov equation if the positions and momenta of the test particle obey the relativistic Hamilton equations [95]:

$$\begin{aligned} \dot{\mathbf{x}}_i =& \frac{\mathbf{p}_i}{E_i} \\ \dot{\mathbf{p}}_i =& -\nabla_x E_i + coll \end{aligned} \tag{3.54}$$

where the term *coll* indicates the effect of the collision integral, while $-\nabla_x E_i$ comes from the presence of a mean field depending from the mass of the generic particle.
In this work, the Boltzmann relativistic equation of motion will be solved in the case of binary collision without the $\nabla_x E_i$ term. In this way, the equations of motion are implemented numerically as shown hereafter:

$$\begin{aligned} \mathbf{x}_i(t+\Delta t) =& \mathbf{x}_i(t-\Delta t) - 2\Delta t \left(\frac{\mathbf{p}_i(t)}{E_i(t)}\right) \\ \mathbf{p}_i(t+\Delta t) =& \mathbf{p}_i(t-\Delta t) + coll \end{aligned} \tag{3.55}$$

where the index i refers to i-th test particle and Δt is the mesh time.

3.6.1 The stochastic method

In this section it will be discussed the numerical implementation of the collision integral that is based on the so called stochastic method implemented by Xu and Greiner in a parton cascade [79].
In such a method whether one collision between two particles will happen or not is sampled stochastically comparing the collision probability associated to the process P_{22} with a random number chosen between 0 and 1. The collision will occur only if the extracted number is less than P_{22}. The P_{22} can be derived directly from the collision term of the Boltzmann-Vlasov equation [96]. We know in fact that the collision probability in a unit box $\Delta^3 x$ and unit time Δt can be defined as the ratio between the

number of collision that happen in such unit box during the time Δt and the total number of pair present in the unit box

$$P_{22} = \frac{\Delta N_{coll}^{2\to 2}}{\Delta N_1 \Delta N_2} \tag{3.56}$$

$\Delta N_{coll}^{2\to 2}$ is simply derived once is known the collision rate per unit phase space indicated in the following equation that can be read off from the collision term:

$$\begin{aligned}\frac{\Delta N_{coll}^{2\to 2}}{\Delta t \frac{1}{(2\pi)^3}\Delta^3 x \Delta^3 p_1} =& \frac{1}{2E_1}\frac{\Delta^3 p_2}{(2\pi)^3 2E_2} f_1 f_2 \\ &\times \frac{1}{\nu}\int \frac{d^3p_1'}{(2\pi)^3 2E_1'}\frac{d^3p_2'}{(2\pi)^3 2E_2'}|\mathcal{M}_{12\to 1'2'}|^2 \\ &\times (2\pi)^4\delta^4(p_1+p_2-p_1'-p_2').\end{aligned} \tag{3.57}$$

Writing the distribuction function in the following way:

$$f_i = \frac{\Delta N_i}{\frac{1}{(2\pi)^3}\Delta^3 x \Delta^3 p_i} \quad i = 1,2 \tag{3.58}$$

and employing the definition of cross section [77]:

$$\sigma_{22} = \frac{1}{4F}\frac{1}{\nu}\int \frac{d^3p_1'}{(2\pi)^3 2E_1'}\frac{d^3p_2'}{(2\pi)^3 2E_2'}|\mathcal{M}_{12\to 1'2'}|^2(2\pi)^4\delta^4(p_1+p_2-p_1'-p_2') \tag{3.59}$$

where $F = \sqrt{(p_1\cdot p_2) - m_1^2 m_2^2}$ is the so called invariant flux, one obtains the expression for the probability:

$$P_{22} = \frac{\Delta N_{coll}^{2\to 2}}{\Delta N_1 \Delta N_2} = v_{rel}\sigma_{22}\frac{\Delta t}{\Delta^3 x} \tag{3.60}$$

where the relative velocity v_{rel} is defined as:

$$v_{rel} = \frac{\sqrt{(p_1\cdot p_2) - m_1^2 m_2^2}}{E_1 E_2} = \frac{\sqrt{[s-(m_1+m_2)^2][s-(m_1-m_2)^2]}}{2E_1 E_2} \tag{3.61}$$

with $s = (p_1+p_2)^2$ and in the massless case becomes:

$$v_{rel} = \frac{s}{2E_1 E_2}. \tag{3.62}$$

The numerical solution using the stochastic method converges to the exact solution of the Boltzmann equation in the limit $\Delta t \to 0$, $\Delta^3 x \to 0$. Hence we divide the space into sufficiently small spatial cells. In order to have reasonable results Δt and $\Delta^3 x$ have to be taken smaller than the typical scales of spatial and temporal inhomogeneities of the particle densities. Only particles from the same cell can collide with each other, and the collision probability has to be calculated for each pair of couple inside the cell and compared with a random number, and this is done for all the cells in which the lattice space is divided.
In order to reduce the computational time instead of considering all possible pair of particles it is possible to follow the scheme of Refs [79, 97]. In such a scheme the pairs of particles analyzed are an arbitrary number $\mathcal{N}_{22}$. Hence the correct collision rate is obtained multiplying the collision probability by an amplification factor, obtaining in this way an effective probability as indicated in the following expression:

$$P^{eff} = P_{22} \frac{n(n-1)/2}{\mathcal{N}_{22}}. \tag{3.63}$$

A good choice in order to have a substantial reduction of the computational time is to take $\mathcal{N}_{22}$ equal to the number of particle inside the cell n.

CHAPTER 4

TESTING THE CODE

Contents

In this chapter will be discussed the implementation of the initial state fluctuation in a transport approach.
We will start with the description of the implementation of Monte Carlo Glauber model in order to generate in the coordinate space an initial profile that change event by event. Furthermore we will discuss the effect of these initial state fluctuations on the initial eccentricities ϵ_n.
Our purpose is tu study the evolution of the QGP anisotropies. In particular we will investigate how the initial asimmetry in coordinate space is traslated in final anisotropies in momentu space of the emitted particles.
Finally, at the end of the chapter, some convergency test of the code will be presented.

4.1 Initial conditions

In order to generate an initial profile that change event by event we use the Monte-Carlo Glauber model to obtain the initial density distribution for each event. In this model the Woods-Saxon distribution is used to sample randomly the positions of the nucleons in the two colliding nucleus A and B:

$$\rho(r) = \frac{\rho_0}{1 + \exp\left[(r - R)/d\right]} \tag{4.1}$$

where the radius R and the diffuse constant d depend on the particular nucleus (Au or Pb in our case). The above distribution is normalized to the atom number $\int d^3r\rho(r) = A$ with $\rho_0 = 0.163fm^{-3}$, $R = 6.3\,fm$ for Au and $R = 6.5\,fm$ for Pb.

In this way a discrete distribution for these nucleons is generated. We employ the geometrical method to determine if the two nucleons one from the nucleus A and the other one from the nucleus B are colliding. To simulate a collision of two nuclei using the Monte Carlo approach, one first samples the positions of all nucleons in the nucleus according to a Woods-Saxon distribution eq.4.1, and obtains discrete nucleon distributions with each single nucleon corresponding to a δ function. The probability function $\hat{\sigma}(\mathbf{s}_i, \mathbf{s}_j, \mathbf{b})$ for two nucleons to collide is taken to be geometrical in form:

$$\begin{aligned} \hat{\sigma}(\mathbf{s}_A, \mathbf{B}_j, \mathbf{b}) &= 1 \qquad if\ \ d_T = \sqrt{(x_A - x_B)^2 + (y_A - y_B)^2} \leq \sqrt{\sigma_{NN}/\pi} \\ \hat{\sigma}(\mathbf{s}_A, \mathbf{B}_j, \mathbf{b}) &= 0 \qquad if\ \ d_T = \sqrt{(x_A - x_B)^2 + (y_A - y_B)^2} > \sqrt{\sigma_{NN}/\pi} \end{aligned} \tag{4.2}$$

In other words, within this method two nucleons collide each other if the relative distance in the transverse plane is $d_T \leq \sqrt{\sigma_{NN}/\pi}$ where σ_{NN} is the nucleon-nucleon cross section.

In the following discussion we will concentrate on the fireball produced in $Au+Au$ at $\sqrt{s_{NN}} = 200GeV$ and $Pb+Pb$ at $\sqrt{s_{NN}} = 2.76TeV$ so for the nucleon-nucleon cross section we have used $\sigma_{NN} = 4.2\,fm^2$ for RHIC

and $\sigma_{NN} = 7.0\, fm^2$ for LHC.

With the above probability distribution, the calculation of N_{coll} and N_{part} is given by counting the number of collisions and the number of participating nucleons for each event. In this way the position of the participating nucleons will fluctuate from event-to-event.

The next step is the conversion of the discrete distribution for the nucleons into a smooth one by assuming for each nucleon a gaussian distribution centered in the nucleon position. In our model we choose to convert the information of the nucleon distribution into the density in the transverse plane $\rho_T(x, y)$ which is given by the following sum

$$\rho_T(x, y) = C \sum_{i=1}^{N_{part}} \exp\left[-\frac{(x - x_i)^2 + (y - y_i)^2}{2\sigma_{xy}^2}\right] \tag{4.3}$$

where C is an overall normalization factor fixed by the longitudinal distribution dN/dy while σ_{xy} is the Gaussian width which regulate the smearing of the fluctuations. In the following calculations the Gaussian width has been fixed to $\sigma_{xy} = 0.5\, fm$. In our calculation we have assumed a longitudinal boost invariant distribution with a uniform pseudorapidity distribution with $\eta = y = \frac{1}{2} \ln \frac{t+z}{t-z}$ in the range $-2.5 \leq \eta \leq 2.5$. The initial total number of particles has been fixed to $\frac{dN}{dy} = 1050$ for RHIC energies and $\frac{dN}{dy} = 2500$ for LHC energies for $(0 - 5)\%$ of centrality class (corresponding to an input parameter fo $b = 2.5\, fm$) and for mid rapidity.

In fig. 4.1 it is shown the initial test particle distribution at mid rapidity along the x-axis for a given event and for $y = 0\, fm$ (left panel) and $y = 2.5\, fm$ (right panel). In particular in fig. 4.1 we compare the analitical results (yellow band) as given in the formula 4.3 with the same calculation coming from our code (black point). The calculation with our code is made for a given event with impact parameter $b = 7.5\, fm$ at mid rapidity. The good agreement within the error bars between the two result make us confident of the right implementation of the initial

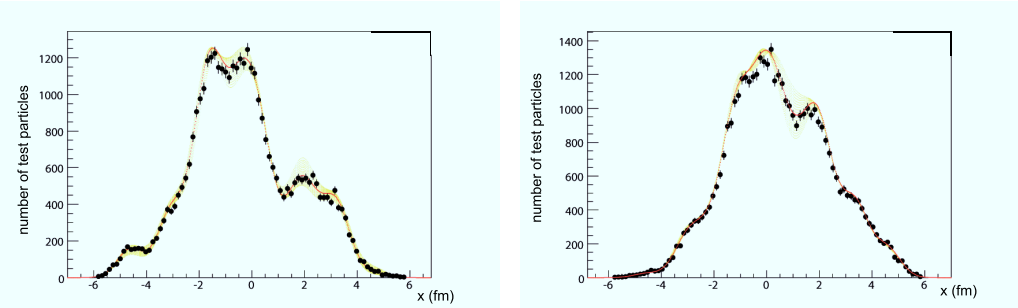

Figure 4.1: Comparison between the analitical result of the density function (red line and yellow band) with respect to the code calculation (black point) for a given event. Left panel refers to a pseudorapidity $y = 0\,fm$ while right panel has $y = 2.5\,fm$.

state fluctuation in the transport code. Note that both analitical and simulation code results will be exactly the same when $N_{test} \to \infty$. In our simulation in fig. 4.1 we have used $N_{test} = 3000$ that was enough to have a resolution better than 5%.

The contour plot of the initial transverse density at mid rapidity for a given event with impact parameter $b = 7.5fm$ is reported in fig. 4.2. The upper panel refers to the system $Au + Au$ at $\sqrt{s_{NN}} = 200GeV$ and the lower panel to $Pb + Pb$ at $\sqrt{s_{NN}} = 2.76TeV$.

For the initialization in momentum space at RHIC (LHC) energies we have considered for the bulk, i.e. for partons with transverse momentum $p_T \leq p_T 0 = 2\,GeV$ $(3\,GeV)$ a thermalized spectrum in the transverse plane:

$$\frac{dN}{dp_T^2} \propto m_T e^{-\frac{m_T}{T}} \tag{4.4}$$

with $m_T = \sqrt{p_T^2 + m^2}$ and T is the temperature. Assuming the local equilibrium the initial local temperature in the transverse plane $T(x, y)$ is evaluated by using the standard thermodynamical relation:

$$\rho_T(x, y) = \frac{\gamma}{\pi^2} T^3 \tag{4.5}$$

with $\gamma = N_c N_f N^{spin} N^q = 37$. In fig. 4.3 it is shown the corresponding initial local temperature in transverse plane for RHIC (upper panel) and

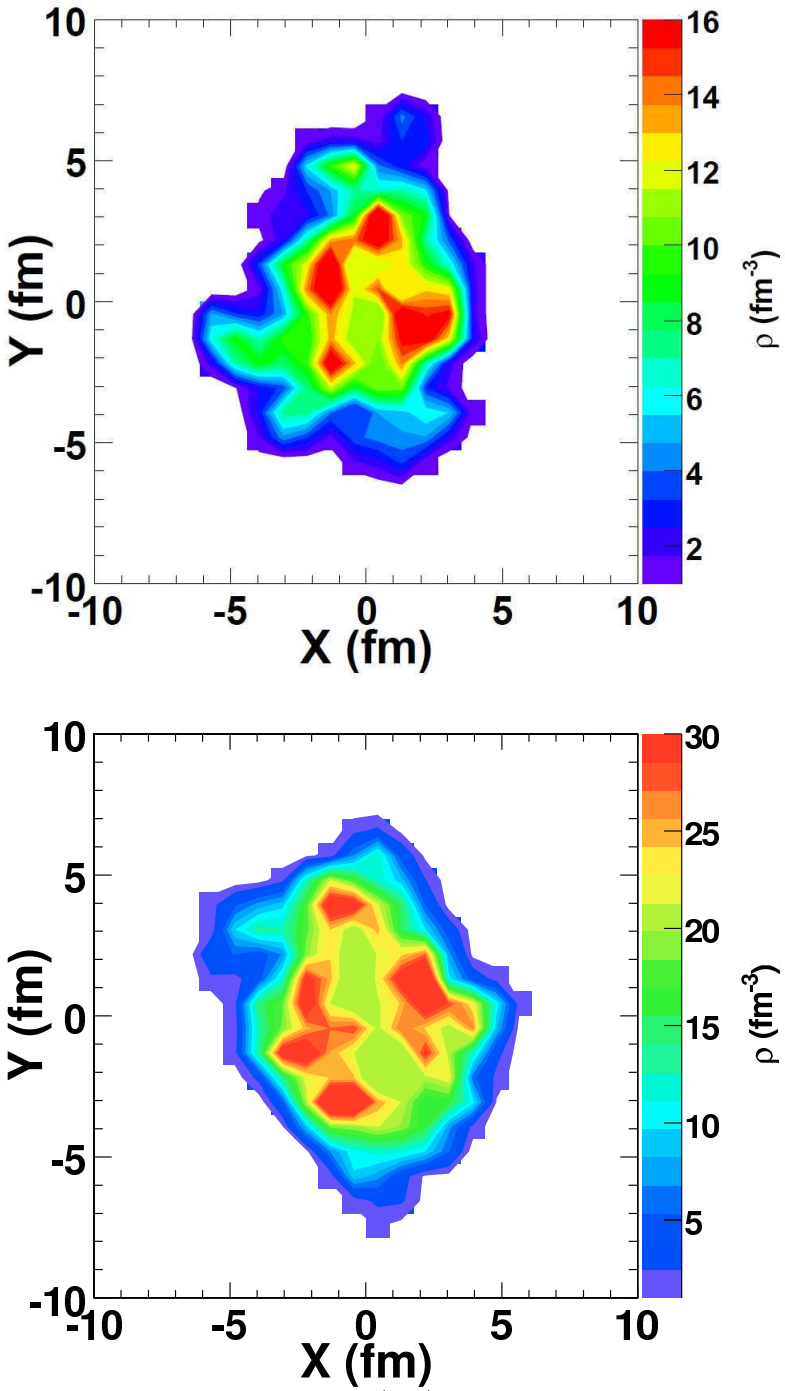

Figure 4.2: Initial transverse density $\rho_T(x, y)$ at mid rapidity for $Au+Au$ at $\sqrt{s_{NN}} = 200\,GeV$ (upper panel) and $Pb+Pb$ at $\sqrt{s_{NN}} = 2.76\,TeV$ (lower panel). These plots are for an impact parameter of $b = 7.5\,fm$.

LHC (lower panel). As shown in the central region of the fireball for mid peripheral collision we can reach temperature $T \cong 2T_C \approx 300\,MeV$ at RHIC and $T \approx 400\,MeV$ at LHC. These are typical values used also in hydrodynamical simulations. Notice that in this way the fluctuations in the initial geometry include fluctuations in momentum space. Therefore for partons with $p_T > p_0$ we have assumed the spectrum of non-quenched minijets according to standard NLO-pQCD calculations with a power law shape:

$$\frac{dN^{minijet}}{dp_T^2} \cong \frac{A}{(B + p_T)^n} \tag{4.6}$$

The initial transverse momentum of the particles is distributed uniformly in the azimuthal angle.

4.2 Initial geometry

Once the transverse density $\rho_T(x, y)$ has been fixed the initial anisotropy in coordinate space can be evaluated. The initial anisotropy is quantified in terms of the following coefficients ϵ_n:

$$\epsilon_n = \frac{\sqrt{\langle r_T^n \cos(n\phi)\rangle^2 + \langle r_T^n \sin(n\phi)\rangle^2}}{\langle r_T^n \rangle} \tag{4.7}$$

where $r_T = \sqrt{x^2 + y^2}$ and $\phi = arctan(y/x)$ are the polar coordinate in the transverse plane.

In figure 4.4 we have shown the distribution of ϵ_2, ϵ_3, ϵ_4 and ϵ_5 as a function of the number of participant N_{part} and for a total number of events $N^{event} = 10^5$. In figure 4.5 it has been shown the corresponding averaged initial spatial anisotropies ϵ_2, ϵ_3, ϵ_4 and ϵ_5 as a function of the impact parameter. The second coefficient ϵ_2 (solid green line) shows a stronger dependence with the impact parameter respect to the other coefficients because it acquires a contribution due to the global almond shape of the fireball while the other harmonics have most of their origin in the fluctuations in the positions of the nucleons. In fact for more central

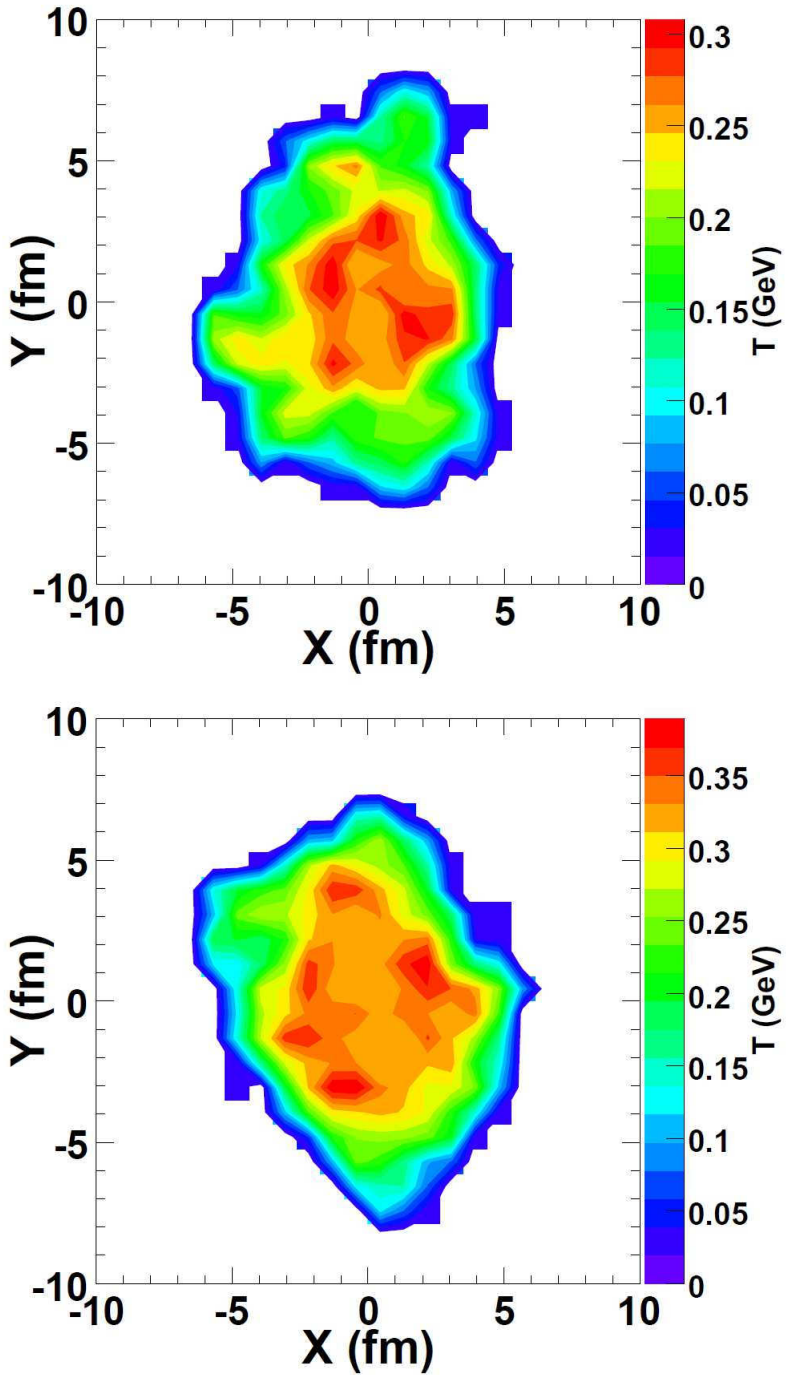

Figure 4.3: Initial temperature in trasverse plane at RHIC (upper panel) and LHC (lower panel). These plots are for an impact parameter of $b = 7.5\, fm$.

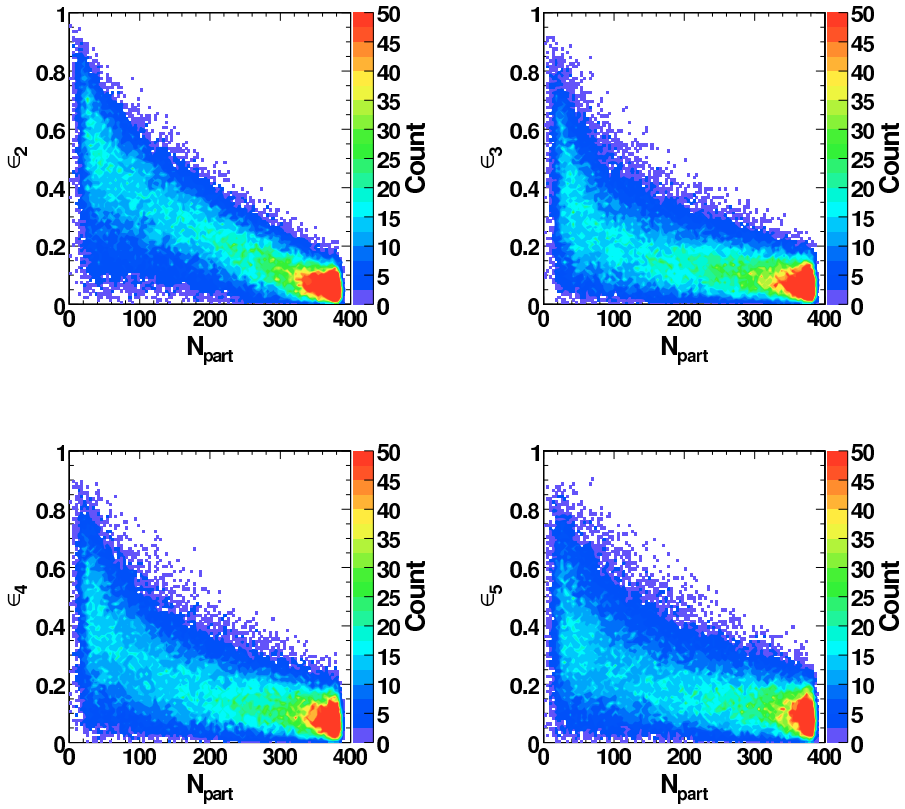

Figure 4.4: Initial anisotropy coefficient ϵ_n as a function of the participant nucleons N_{part} respectively for $n = 2$, 3, 4 and 5.

collisions $b \leq 2.5\, fm$ the ϵ_2 becomes smaller than the other harmonics this is because when the effect of the overlap region disappear the only contribution to ϵ_2 comes from the fluctuations. In fact for smaller impact parameter becomes more difficult to have fluctuations of the positions of the nucleons along one direction and for large n we get larger ϵ_n. Moreover, in fig. 4.5 we have shown the comparison between the Monte Carlo Glauber approach (solid lines) and the Glauber model (dashed lines). It is clear that in this second case with the absence of the initial fluctuation, the ϵ_n vanishes for all odd moments and presents a very different behaviour for even ones, expecially at low impact parameter b. In fact for central collisions ϵ_2 in the Glauber model becomes zero due to

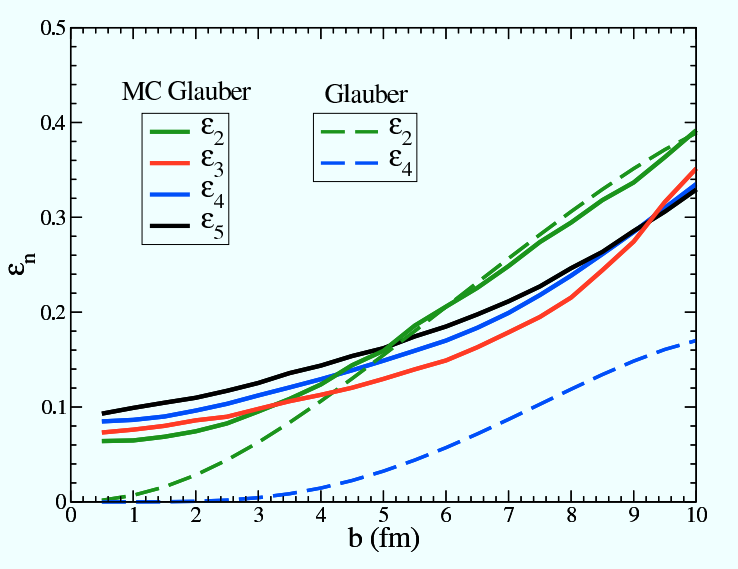

Figure 4.5: Initial spatial anisotropies ϵ_n as a function of the impact parameter. Different colors are for different n. The solid lines refer to the Monte Carlo Glauber while the dashed ones to the Glauber model.

a more symmetric shape while for large impact parameter it approaches the values obtained with the Monte Carlo Glauber where the fluctuation gives a very small contribution.

4.3 Simulation code parametrization

In the following discussion, the final set of parameters chosen in our simulation are tested and presented.

The inclusion of the initial state fluctuations introduces further difficulties because in order to get stable results we need to have a good sampling of the initial geometry event by event and this is controlled by the total number of test particles N_{test}. Furthermore an irregular initial profile need a good calculation grid resolution. We have checked the convergency of our results for v_2, v_3, v_4 and v_5 with the lattice spacing of the calculation grid and N_{test}. In order to determine this convergency we have performed our simulations with a fixed viscosity $\eta/s = 1/4\pi$ constant during all the expansion of the fireball and for an impact parameter $b = 7.5\, fm$

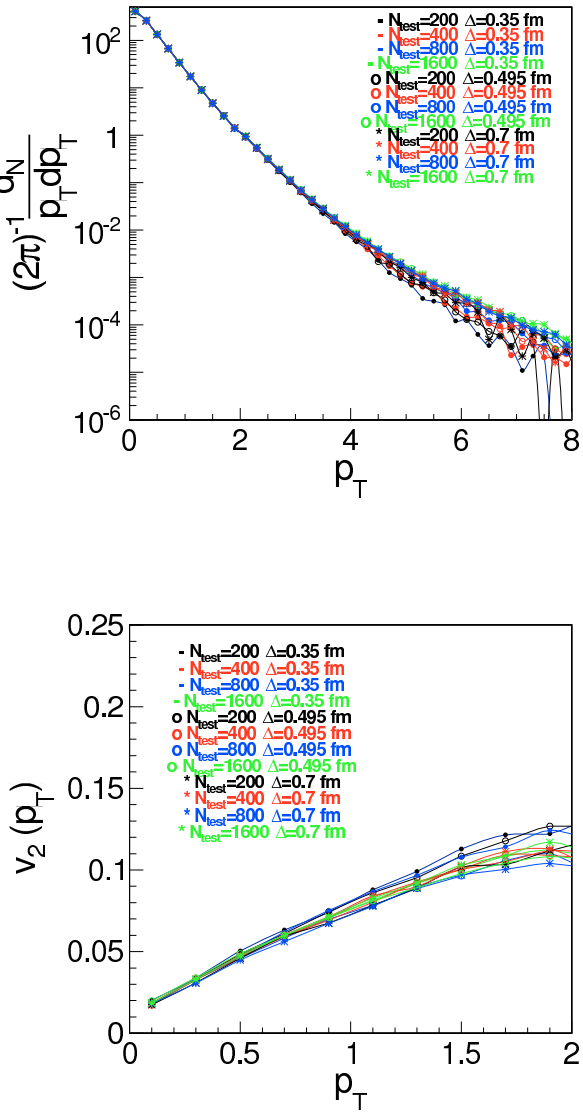

Figure 4.6: Checking the convergency with several parameters. The results of our code are reported for the spectra (upper panel) and for the elliptic flow (lower panel). See the text for details.

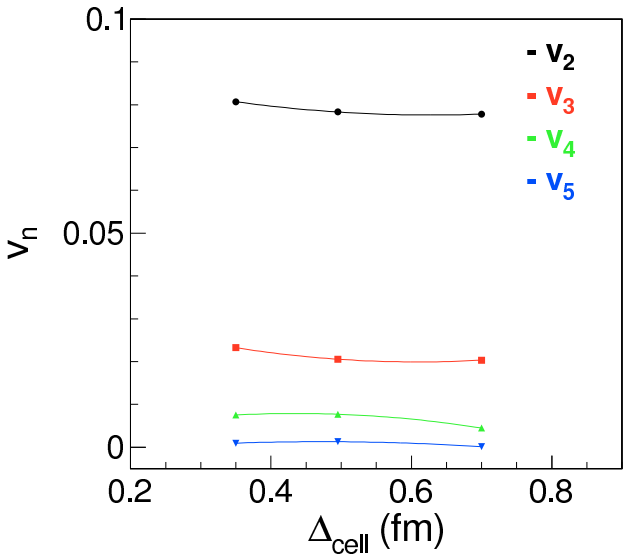

Figure 4.7: v_n at mid rapidity as function of the grid dimension at a fixed value of p_T.

for the case of $Au + Au$ at $\sqrt{s_{NN}} = 200\,GeV$. Moreover, we have selected three different grid dimensions ($\Delta x = \Delta y = 0.35\,fm$, $0.465\,fm$ and $0.7\,fm$) and four different number of test particles for real particle (200 N_{test}, 400 N_{test}, 800 N_{test} and 1600 N_{test}). Finally, in order to separate the physical fluctuation from the numerical ones, we set for these simulations a fixed density profile calculated for a single event with the fluctuating Monte Carlo Glauber approach.

In the upper panel of fig. 4.6 we have shown the results for the spectra, $(2\pi)^{-1}\frac{dN}{p_T dp_T}$, integrated over the azimuthal angle and over the momentum rapidity window $|y| < 0.5$ as function of p_T for different grid resolution and for different number of test particles N_{test}. The spectra clearly show a good convergency for all cases, expecially at intermediate transverse momentum $p_T < 4\,GeV$ which is the range of our interest. However this study does not allow us to choose the best set of parameters. A more

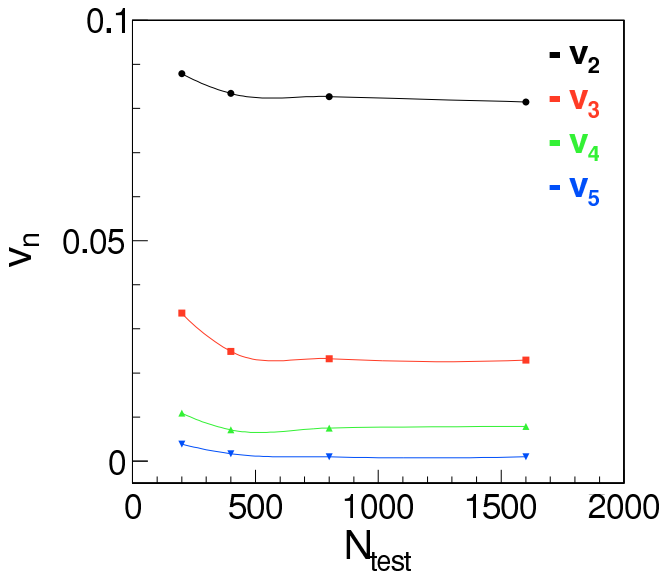

Figure 4.8: v_n at mid rapidity as function of the total number of test particles for real particle at a fixed value of $p_T = 1\,GeV$.

sensitive observable is the elliptic flow v_2. In fact as shown in the lower panel of fig. 4.6 the $v_2(p_T)$ at mid rapidity reveal a small sensitivity to the grid resolution and a large sensitivity to the number of test particles. We observe a difference of about 20% for the single event.

In order to focus on the results of elliptic flow and to select the best set of parameter, in fig. 4.7 we reported the value of v_2, v_3, v_4 and v_5 for the three different values of grid dimensions at a fixed transverse momentum $p_T = 1\,GeV$. From this plot it is possible to deduce that for all n-order of flow there is a very small dependence with respect to the lattice spacing of the calculation grid. So that in the following simulations we decide to use $\Delta = 0.35\,fm$ which is the value closer to the one used in viscous hydro calculations of about $0.2\,fm$. Note that the choice of this value of Δ improve the resolution but does not introduce sensible delay in the time of calculation.

In the similar way discussed above in fig. 4.8 we have checked the convergency of the value of v_n with respect to the total number of test particles N_{test} at mid rapidity and for the same fixed value of p_T. The plot shows a dependence in the values of v_n with respect to the number of N_{test} for $N_{test} < 400$ and then a clear stability of the numerical results for all v_n. As a consequence we choose 800 as total number of test particles for real particle in all the following calculations since for $N_{test} = 1600$ the computational time increase of about a factor of 4.

In conclusion, in this preliminary study we have been checking the implementation of the initial state fluctuation and the subsequent evolution spectra and the related collective flows. Moreover, we discussed the initial parametrization of our code and presented the result about the convergency of the numerical procedure. Finally, we found that for the evolution of all $v_n(p_T)$ it is safe to use a grid with $A_T = 0.12 fm^2$ of transverse area and total number of test particles $N_{test} = 2 \cdot 10^6$ and these parameters will be used for all the computations presented in the next chapter.

CHAPTER 5

RESULTS

Contents

In this chapter will be presented the final results coming from the computation of the simulation transport code presented in the previous chapters. The main purpose of this work of thesis is to study the effect of a temperature dependent shear viscosity to entropy density ratio η/s in the evolution of the elliptic flow v_2 and high order harmonics v_n.
To this aim we run our simulations with and without the inclusion of the fluctuating Monte Carlo Glauber initial condition for two different beam energies: RHIC for $Au + Au$ at $\sqrt{s} = 200\,GeV$ and LHC for $Pb + Pb$ at $\sqrt{s} = 2.76\,TeV$.
Moreover, it will be discussed the influence of the impact parameter in the behaviour of the build up of elliptic flow and high order harmonics.
Finally, we have investigated the correlation between the initial spatial

anisotropies ϵ_n and flow coefficients v_n and its evolution with the beam energy.

5.1 Event by event fluctuations

In this section we discuss the effect of the initial state fluctuation on the final azimuthal integrated spectra $(2\pi)^{-1}\frac{dN}{p_T dy dp_T}$ and the differential anisotropic flows $v_n(p_T)$.
The initial time of the simulation have been fixed to $\tau_0 = 0.6\, fm/c$ for RHIC and $\tau_0 = 0.3\, fm/c$ for LHC. In the following table 5.1 is summarized the set of parameters that we have presented in the above discussion:

Table 5.1: Set of parameters chosen in our code. See the text for more informations.

	σ_{NN} (fm^2)	$\sigma_{x,y}$ (fm)	p_0 (GeV)	τ_0 (fm/c)
RHIC	4.2	0.5	2.	0.6
LHC	7.0	0.5	3.	0.3

In this work, we will consider two different types of initial conditions. One of them consist in a fixed initial distribution by using the standard Glauber model as used in previous works, see [98, 99]. The second one consist of an initial profile changing event by event according to the MC glauber model as discussed before.
In our simulations we have used $N_{event} = 500$ events for each centrality class. This number is enough to get solid results for the spectra, differential elliptic flow and high order flow coefficients $v_n(p_t)$.

In fig. 5.1 the spectra at final time of evolution ($t = 7.5\, fm/c$, black color) and initial time ($t = 0.6\, fm/c$, red color) for the two approaches are shown: the solid line refer to the case with initial state fluctuations while the dashed line is for the case without fluctuations. The simulation refers to RHIC $Au + Au$ mid peripheral $|y| < 0.5$ collisions at $\sqrt{s} = 200\, GeV$ and for $4\pi\eta/s = 1$ constant during all the expansion of the fireball.
The results of our model show that the inclusion of the initial state fluc-

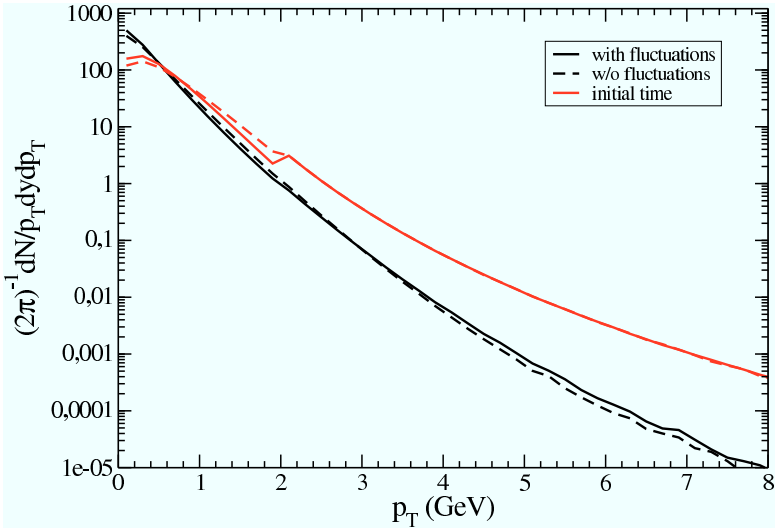

Figure 5.1: Transverse momentum spectrum at RHIC in $Au + Au$ collisions $\sqrt{s} = 200\,GeV$. Solid line is for the initial state that change event by event while dashed line refers to the case with an averaged initial profile. These results are $(20 - 30\%)$ centrality class and $4\pi\eta/s = 1$ constant during all the expansion of the fireball.

tuation introduces a small tail in the parton distribution at high p_T with respect to the standard non fluctuating case at the end of the evolution while in the initial time the two approach are very similar. This means that due to the different density distribution we have a little bit more particles that escape from the interaction zone at the early stage of the collision. However, this is not a significantly sizeable effect while the most significant consequences in the application of the event by event approach are in the build up of the differential flow coefficients v_n.
The elliptic flow $v_2(p_T)$ and the high order harmonics $v_3(p_t)$ and $v_4(p_T)$ have been calculated as

$$v_n = \langle \cos n(\phi - \Psi_n) \rangle \tag{5.1}$$

where the momentum space angles Ψ_n are given by

$$\Psi_n = \frac{1}{n} \arctan \frac{\langle \sin(n\phi) \rangle}{\langle \cos(n\phi) \rangle} \tag{5.2}$$

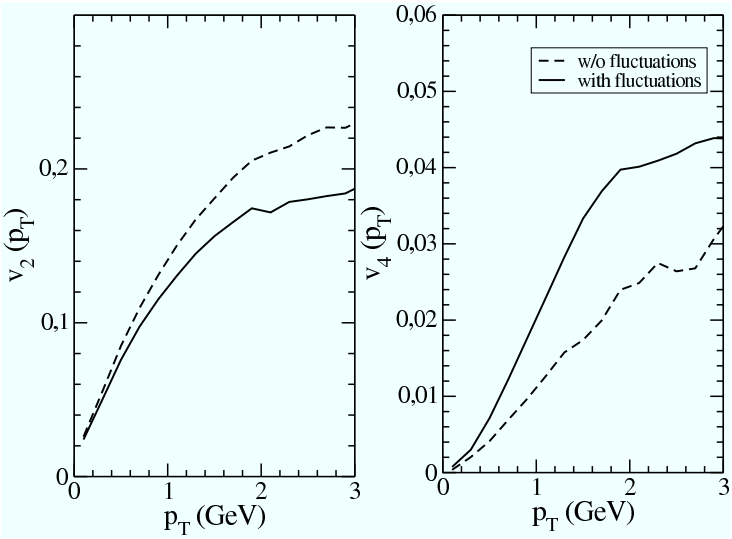

Figure 5.2: Results for $Au + Au$ collisions at $\sqrt{s_{NN}} = 200\,GeV$ for $(20 - 30\%)$ centrality class. Left: differential elliptic flow $v_2(p_T)$ at mid rapidity. The solid line refer to the case with initial state fluctuations while the dashed lines is for the case without initial fluctuations. Right: differential $v_4(p_T)$ at mid rapidity with the same legend as in the left panel.

as detailed thouroughly in chapter 4.

In figure 5.2 we present the results for the final $v_2(p_T)$ and $v_4(p_T)$ corresponding to the two different initial configurations. In the left panel we show the comparison between the differential elliptic flow $v_2(p_T)$ obtained with and without (w/o) fluctuations. These results are for $Au + Au$ collisions at $\sqrt{s} = 200\,GeV$ and for $(20 - 30\%)$ centrality class. In these calculation we have considered $4\pi\eta/s = 1$ constant during all the expansion of the fireball.

One can note that for this centrality the effect of the fluctuations in the initial geometry is to reduce the $v_2(p_T)$ with a reduction of about 20%. Despite for this centrality we have the same initial eccentricity, see green solid and dashed lines in fig. 4.5, the fluctuations anyway lead to a reduction of $v_2(p_T)$. This reduction is related to the fact that for an irregular geometry in the transverse plane the pressure gradients generate a small flow towards the inner part of the fireball reducing the build up of the az-

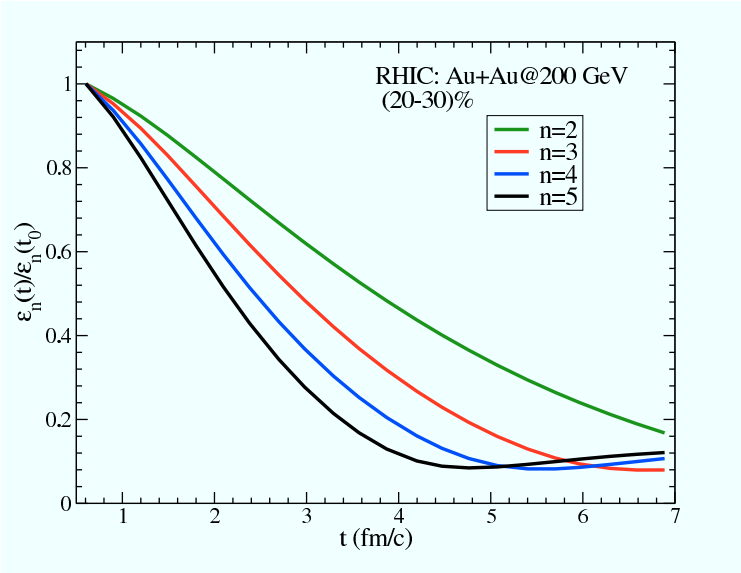

Figure 5.3: $\epsilon_n/\epsilon_n(t_0)$ as a function of the time for $Au + Au$ collisions at $\sqrt{s_{NN}} = 200\,GeV$ and for peripheral collisions. Different colors refer to different harmonics n.

imuthal anisotropy in momentum space due to the global almond shape. Moreover the fluctuations in the initial geometry play the role of generating the higher order harmonics in particular the odd harmonics v_3 which were absent due to the symmetry constraint in the averaged initial configuration.

In the right panel of fig. 5.2 we compare the quadrangular flow $v_4(p_T)$ for the same system with and w/o fluctuations. We observe an opposite behaviour with respect to the $v_2(p_T)$: the initial state fluctuations increase the final $v_4(p_T)$ of about 60%. This result is related to the fact that the fluctuations introduce a larger initial ϵ_4 as shown by the comparison between blue solid and dashed lines in fig. 4.5. In other words for mid peripheral collisions most of $v_2(p_T)$ comes from the global almond shape while $v_4(p_T)$ comes from the fluctuations.

In fig. 5.3 it is shown the time evolution of the initial eccentricities at RHIC energies. In particular we plot the ϵ_n normalized to the initial eccentricity $\epsilon_n(t_0 = 0.6\,fm/c)$. At very early times the small deformation of the fireball in the transverse plane decrease with time and at first order

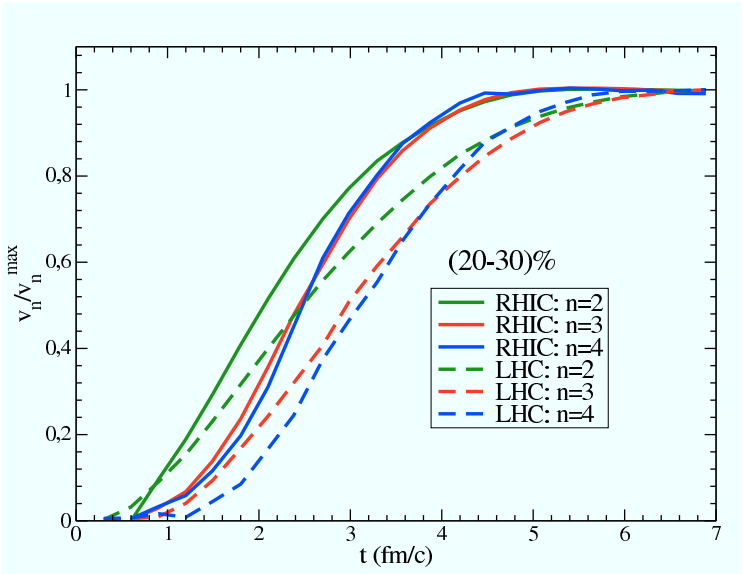

Figure 5.4: $\langle v_n \rangle / \langle v_n \rangle^{max}$ as a function of time at mid rapidity and for $(20-30)\%$ of centrality. Solid lines are the results for $Au+Au$ at $\sqrt{s_{NN}} = 200\,GeV$ while dashed lines $Pb+Pb$ at $\sqrt{s_{NN}} = 2.76\,TeV$. Different colors correspond to different harmonics: green, red and blue curves correspond to $n = 2$, 3 and $n = 4$ respectively.

of this deformation we have that $\epsilon_n \propto \epsilon_n(t_0) - \alpha_n\, t^{n-2}$. This gives the ordering in the time evolution of ϵ_n shown in the plot: the time evolution of ϵ_n is faster for larger n.

On contrary $\langle v_n \rangle$ show an opposite behaviour during the early times of the expansion of the fireball. In fig. 5.4 we present the average $\langle v_n \rangle$ normalized to $\langle v_n^{max} \rangle$ which is the maximum value at the end of the expansion. The solid line refers to $Au+Au$ collisons at $\sqrt{s} = 200\,GeV$ while the dashed one to $Pb+Pb$ collisions at $\sqrt{s} = 2.76\,TeV$. As it is possible to see the $\langle v_n \rangle$ appear later for larger n and it is flatter at early times for larger n. Similar results have been obtained in a $2+1D$ transport approach where considerations on the early times evolution of the fireball give that $\langle v_n \rangle \propto t^n$ [100, 101].

As we can see comparing the dashed lines with the solid ones the time evolution of $\langle v_n \rangle$ depends on the collision energy, in fact for example the generation of v_n ends at $t \approx 4.5\,fm/c$ at RHIC and at $t \approx 6.5\,fm/c$

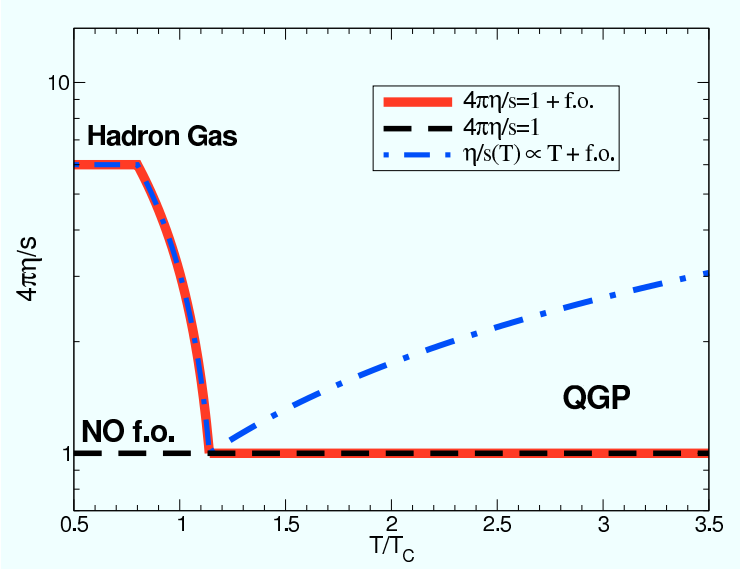

Figure 5.5: Different parametrization of $\eta/s(T)$. Black dashed line refer to $4\pi\eta/s = 1$ during all the evolution. Red solid line refers to the inclusion of kinetic f.o. for $T \leq 1.2T_C$. Finally, blue dot dashed line refer to the inclusion of linear temperature dependence for $T > 1.2T_C$ and the kinetic f.o. at lower temperature.

al LHC energies. At LHC energy we note that after $2\,fm/c$ about 40% of the v_2 is already formed, while ate the same time only 10% of v_4 is present. This suggests that the different harmonics are sensitive to different stages of the QGP fireball evolution, hence their value is determined by the properties of QGP at different temperatures.

5.2 Effect of the $\eta/s(T)$ on $v_n(p_T)$

Differential flow coefficients $v_n(p_T)$ are observables that carry out more informations about the fireball created in the heavy ion collisions with respect to the p_T spectrum. In particular they are sensitive to the transport properties of the medium like the η/s ratio.
In this section we discuss the role of the η/s on the build up of the elliptic flow $v_2(p_T)$ and on the high order harmonics $v_3(p_T)$ and $v_4(p_T)$.

In order to study the role of the η/s ratio and its temperature dependence we have performed three different calculations, corresponding to

the different parametrization of η/s reported in figure 5.5: one with a constant $4\pi\eta/s = 1$ during all the evolution of the system (dashed line); another one with $4\pi\eta/s = 1$ at higher temperature in the QGP phase and an increasing η/s in the cross over region towards the estimated value for hadronic matter $4\pi\eta/s \approx 6$ (solid line).
Such an increase of η/s in the cross over region $0.8T_C \leq T \leq 1.2T_C$ allows for a smooth realistic realization of the kinetic freeze-out. This is because at lower temperature in our approach the effective total cross section is $\sigma \propto 1/\eta/s$ (see eq. 3.47) therefore to account for the increase of η/s towards the estimated value for the hadronic matter, the total cross section decrease. In the following discussion the term f.o. take into account the increase of η/s at low temperature.
The third one is shown in fig. 5.5 by the dot dashed line. In this case we consider the increase of η/s at higher temperature with a linear temperature dependence (as suggested by quasi particle models [68]), a minimum close to the critical temperature and the increase of η/s in the cross over region.
In the following discussion with $v_n(p_T)$ we mean the root mean square $v_n\{EP\} = \sqrt{\langle v_n^2 \rangle}$ as it has been done in experimental data using the event plane method (see section 2.6.1).
In the upper panel of fig. 5.6 it is shown the elliptic flow $v_2(p_T)$ and the $v_4(p_T)$ (green and blue lines) at mid rapidity for $(20-30)\%$ centrality for both RHIC $Au+Au$ at $\sqrt{s} = 200\,GeV$ (left panel) and LHC $Pb+Pb$ at $\sqrt{s} = 2.76\,TeV$ (right panel). The increase of the viscosity of the medium has the effect to reduce the v_2 and v_4 as expected, but the size of the reduction is quite different at RHIC with respect to LHC.
As we can see at RHIC energies comparing the green dashed lines with the solid ones, in the upper-left panel of fig. 5.6, the $v_2(p_T)$ is sensitive to the increase of the η/s at lower temperature close to the cross over region. In particular the effect is a reduction of the elliptic flow of about

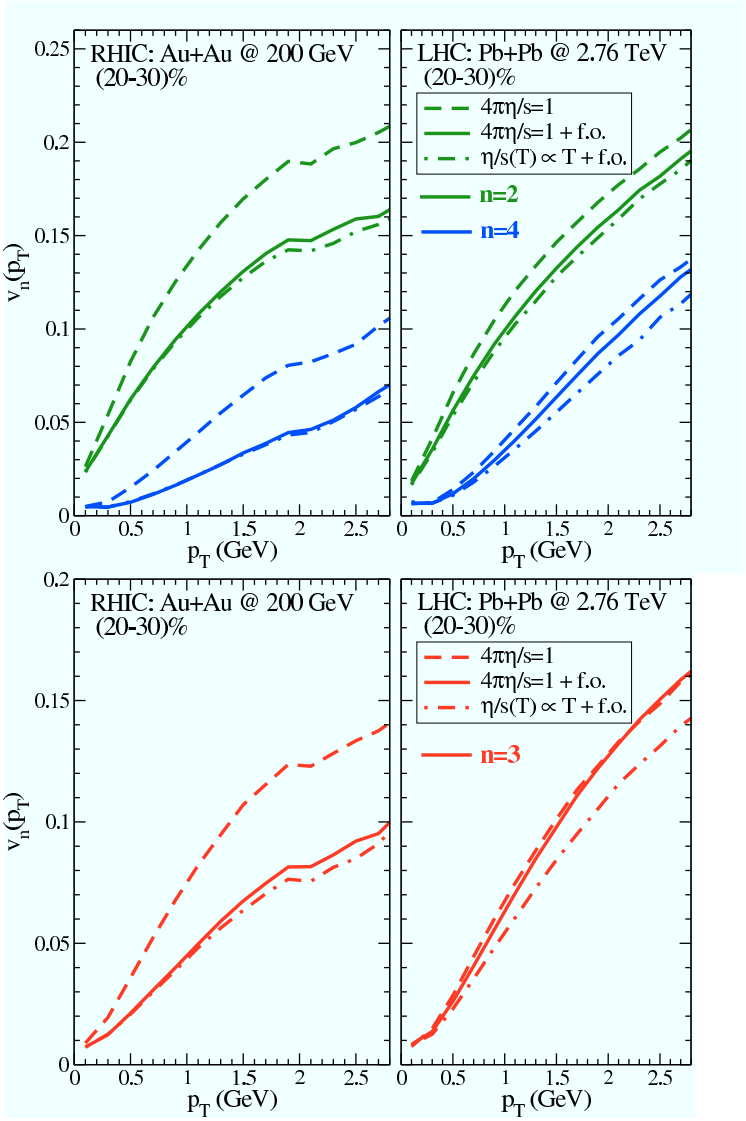

Figure 5.6: Upper panel: differential $v_2(p_T)$ and $v_4(p_T)$ green and blue lines respectively at mid rapidity and for $(20-30)\%$ collision centrality. The comparison is between the two systems: $Au+Au$ at $\sqrt{s}=200\,GeV$ and $Pb+Pb$ at $\sqrt{s}=2.76\,TeV$. The dashed lines refer to the case with a constant $\eta/s=(4\pi)^{-1}$ during all the evolution while the solid lines to the case with $\eta/s=(4\pi)^{-1}$ at higher temperature and with an increasing η/s ratio at lower temperature. Finally, the dot dashed lines represent an η/s increasing linearly with the temperature.
Lower panel: differential $v_3(p_T)$ red lines with the same legend as in the upper panel.

20%. A similar trend is observed for the 4-th harmonic $v_4(p_T)$ where we have a reduction due to the increase of η/s at lower temperature but the effect in this case is larger then the previous, about 30%.
The different sensitivity to the η/s of v_4 with respect to v_2 can be attributed to their different formation time, $t_{v_4} > t_{v_2}$ [88]. As shown in fig. 5.4 each harmonics v_n start to develop at different time. In particular v_4 start to develop approximatively at $\Delta\tau = 1.5 - 2\, fm/c$ later than v_2. This means that different harmonics probe different temperatures and hence different value of the η/s ratio. In fact assuming that the first few fm/c ($\tau \approx 1-2\, fm/c$) of the expanding fireball are dominated by the 1D longitudinal expansion [102] where approximatively $T(\tau) = T_0(\tau_0/\tau)^{1/3}$ we have that when v_4 start to develop at about $\tau \approx 2\, fm/c$ the temperature is $1.3T_C$ at RHIC and $2T_C$ at LHC. In other words this tell us that the v_3 and v_4 at RHIC energies start to develop closer to the cross over region. According to this interpretation and looking at fig. 5.4 a similar trend should be seen also for v_3 (as we find in fig. 5.6 lower-left panel). On the other hand at LHC energies, upper-right panel of fig. 5.6, the scenario is different, the elliptic flow is almost unaffected by the increase of η/s ratio at low temperature (in the hadronic phase) as we can see comparing the green dashed line with the solid one. Instead we observe that the increase of η/s at lower temperature has a more sensitive effect on the $v_4(p_T)$ with a reduction of about 5%, see blue solid and dashed lines. Again this different sensitivity to the η/s in the cross over region between v_2 and v_4 at LHC are consistent with the results obtained at RHIC energies and related to the different formation time of the harmonics. The greater sensitivity at RHIC energies of both v_2 and v_4 to the η/s at low temperature is related to the different life time of the fireball. In fact the life time of the fireball at LHC is greater than that at RHIC, 8-10 fm/c at LHC against 4-5 fm/c at RHIC. In general this means that at RHIC energies the v_n have not enough time to fully develop in the QGP phase.

While at LHC energies we have that the v_n develops almost completely in the QGP phase and therefore it is less sensitive to the dynamics at lower T.
Other interesting informations can be extracted by studying the $v_n(p_T)$ at different collision energies for example from RHIC to LHC energies. In particular it is possible to extract information about the temperature dependence of η/s. In fig. 5.6 it is shown the effect of an $\eta/s(T)$ in the QGP phase. In the comparison between the solid lines and the dot dashed ones the only difference is in the linear temperature dependence of η/s for $T > T_C$ while at lower temperature we have the same dependence. As we can see the v_4 at LHC is sensitive to the change of η/s at higher temperature while at RHIC energies the v_4 is unaffected by this change.
In the lower panel of fig. 5.6 it is shown the triangular flow $v_3(p_T)$ (red lines) at mid rapidity for (20−30)% centrality and for both RHIC Au+Au at $\sqrt{s} = 200\,GeV$ (left panel) and LHC Pb+Pb at $\sqrt{s} = 2.76\,TeV$ (right panel). In agreement with what has been obtained for the even harmonics v_2 and v_4, we observe at RHIC energies a reduction of $v_3(p_T)$ due to the increase of the η/s at low temperature with a reduction of about 30%, while at LHC it is almost insensitive to the change of η/s in the cross over region. However we observe that at LHC the third and fourth harmonics are more sensitive to the change of $\eta/s(T)$ with respect to the elliptic flow with a deviation of about 10% and 15% for v_3 and v_4 against 5% for v_2.

Finally, even if in the results presented in this work the hadronization is not included, in fig. 5.7 we compare our simulation results with the experimental data of both RHIC and LHC. In fact while the hadronization and hadron decay can lead to some re-shaping of the $v_n(p_T)$ the comparison allows us to show that the $v_n(p_T)$ generated by our transport approach show similar trends and size to the experimental data for all

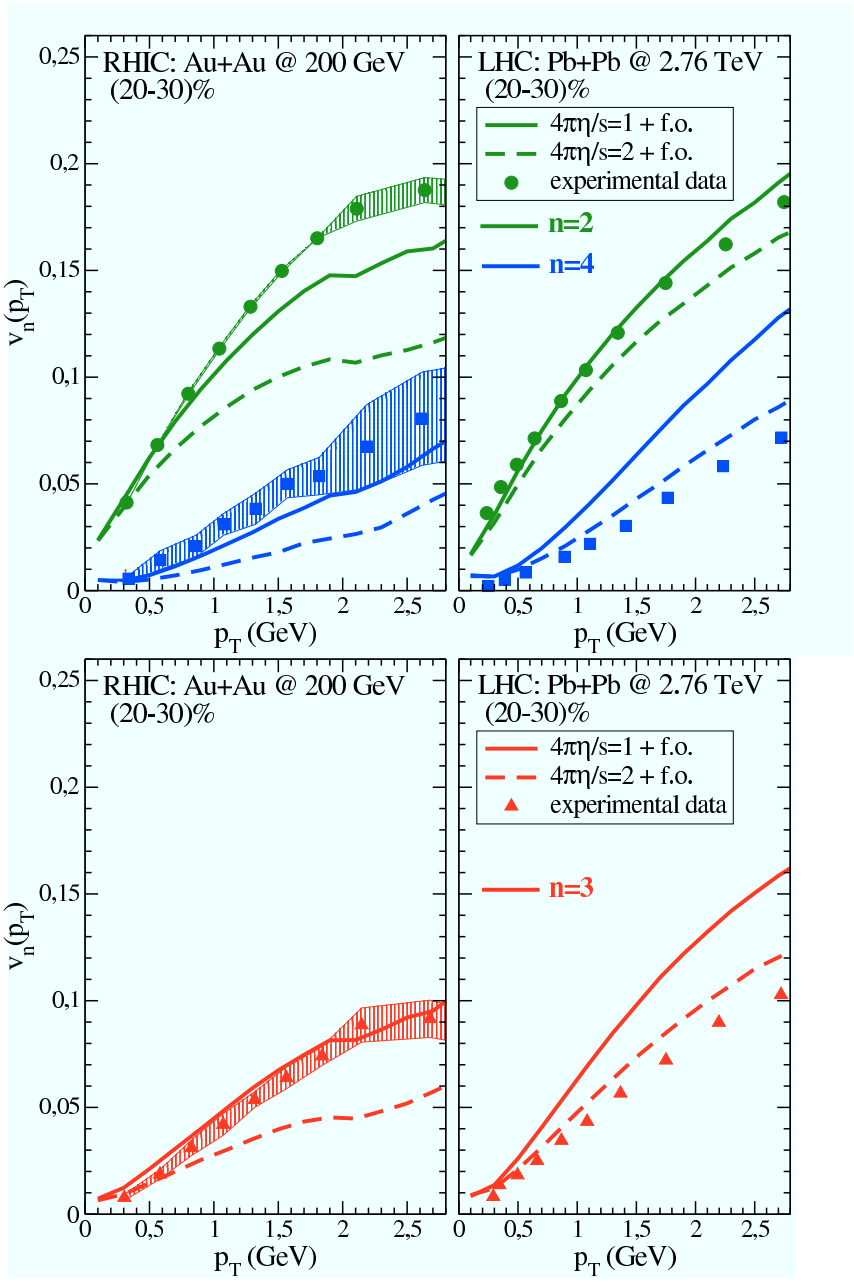

Figure 5.7: Comparison between experimental data and differential v_n coming from our simulation code (see the text for details) at both RHIC and LHC energy (see legend).

the n-harmonics. Left panels report the comparison between our calculations and most recent data of the PHENIX experiment at RHIC for $Au+Au$ collisions at $\sqrt{s} = 200\,GeV$ at mid rapidity and for $(20-30)\%$ centrality with their error bars [103] while in the right panels of fig. 5.7 is shown the same comparison at LHC energies with the data taken from CMS collaboration for $Pb+Pb$ collisions at mid rapidity for $(20-30)\%$ centrality (in this case the error bars are included in the experimental points) [104, 105]. Different colors refer to different flow harmonics: v_2 (green lines), v_3 (red lines) and v_4 (blue lines). As we already mentioned, fig. 5.7 clearly shows that at LHC energy a larger η/s is favored. In particular in fig. 5.7 we compare with the case where $4\pi\eta/s = 2$ in the QGP phase plus the kinetic f.o. in the cross over region (dashed lines) while at RHIC energies the case with $4\pi\eta/s = 1$ in the QGP phase (solid lines) is quite close to the data within the experimental error bars. This result is in agreement to that has been obtained in viscous hydrodynamical calculations in which is usually exctracted a range of value $1 < 4\pi\eta/s < 3$ and favor for LHC energy and η/s about 1.5-2 times larger than at RHIC. The most natural interpretation of such a trend is that in the QGP phase the η/s has a T dependence as suggested by quasi-particle models.

5.3 $v_n(p_T)$ for central collisions

In order to have more information about the dynamic of the collisions we have performed our calculation also for ultra central collisions with $b = 0\,fm$. In such a way it is possible to study all v_n's as coming from the fluctuations because of the circular symmetry determined by the exact centrality of the collisions. The ultra central collisions are interesting because the initial geometry and the ϵ_n comes completely from the fluctuations and in particular as we will discuss in the next section the final v_n is strongly correlated with the initial ϵ_n.

For this case we run our simulation for the most interesting energy of

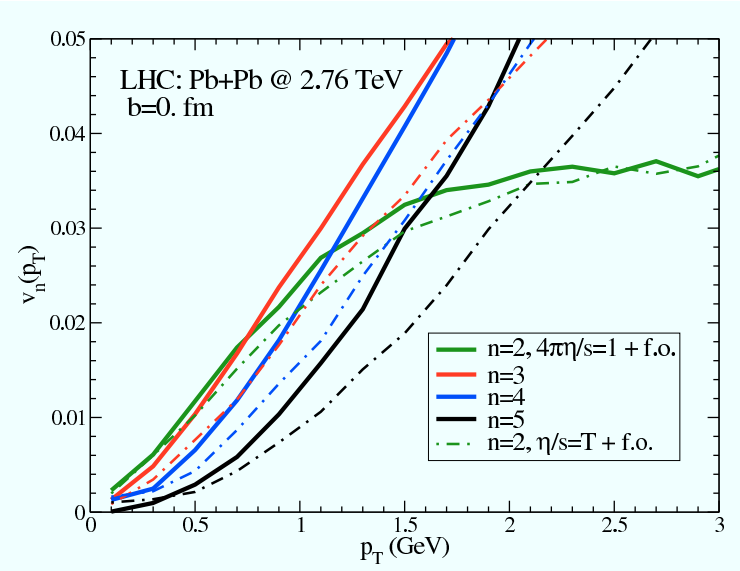

Figure 5.8: Differential $v_n(p_T)$ as a function of the transverse momentum for $Pb+Pb$ collisions at $\sqrt{s_{NN}} = 2.76 TeV$ and for central collision, $b = 0. fm$. Different colors are for different harmonics n. Solid lines refer to the case with $4\pi\eta/s = 1$ in QGP phase and f.o. while the dot dashed lines refer to the case with $\eta/s \propto T$ in the QGP phase and f.o..

LHC $Pb + Pb$ at $\sqrt{s} = 2.76 TeV$. In figure 5.8 we plot the differential $v_n(p_T)$ as a function of the transverse momentum for the the first five harmonics $n = 2 - 5$ (reported in different colors). We select two different parametrizations for the η/s ratio: solid lines refer to the case with $4\pi\eta/s = 1$ in QGP phase and f.o. (see solid red line in fig. 5.5) while the dot dashed lines refer to the case with $\eta/s \propto T$ in the QGP phase and f.o. (blue dot-dashed line in fig. 5.5).

The first result is that $v_n(p_T)$ at low p_T is much flatter for larger n. This result is in agreement with what has been obtained also in ideal hydrodynamic calculation where one generally expect that $v_n(p_T)$ at low p_T scale like p_T^n [100]. On the other hand at high p_T we observe that $v_n(p_T)$ for $n \geq 3$ increase linearly with p_T. A different behaviour is found for the second coefficient $v_2(p_T)$ where at high p_T it shows a saturation with a behaviour very similar to the experimental data.

We observe in agreement with the results obtained for mid peripheral

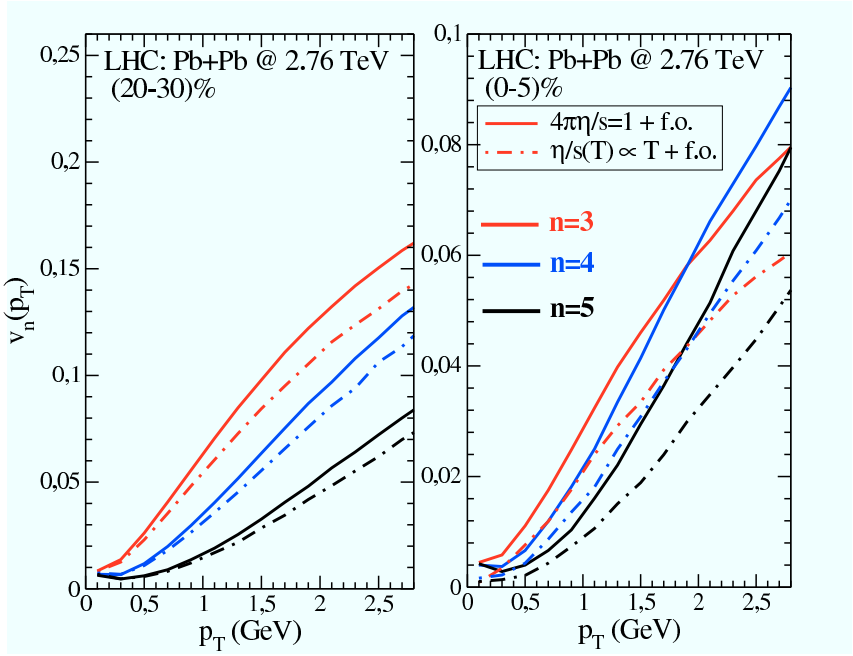

Figure 5.9: Comparison between $v_n(p_T)$ for mid peripheral (left panel) and central (right panel) collision. Different colors refer to different harmonics while solid lines correspond to $4\pi\eta/s = 1$ in QGP phase and f.o. and dot dashed lines to $\eta/s \propto T$ in the QGP phase and f.o.

collisions that the $v_n(p_T)$ at LHC is more sensitive to the value of the η/s ratio in the QGP phase. In particular comparing mid peripheral and central collision one can note that for central collisions $v_n(p_T)$ are more sensitive to the value of η/s in the QGP phase especially for larger value of n. This is shown in fig. 5.9 in which we have been plotted the results of $v_n(p_T)$ for the two different class of centrality: $20-30\%$ in the left panel and $0-5\%$ in the right one. Different colors refer to different harmonics n while with the solid lines it is reported the results for $4\pi\eta/s = 1$ in QGP phase and f.o. and with the dot dashed lines the ones for $\eta/s \propto T$ in the QGP phase and f.o. (as in fig 5.8). We observe once more that $v_n \propto p_T^n$ also in the case of non central collisions. Moreover we note that the effect of the reduction of v_n due to the temperature dependent η/s in the QGP is enhanced when we have $0-5\%$ centrality class and this effect is greater for high n order. In fact, if we take into account the v_3

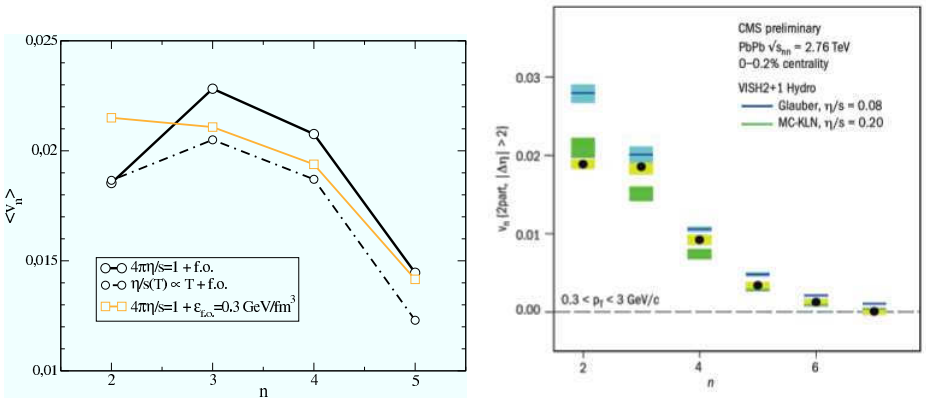

Figure 5.10: Left panel: avaraged $\langle v_n \rangle$ in function of n for three different cases of viscosity: solid black line refers to $4\pi\eta/s = 1$ in QGP phase and f.o., dot dashed one for $\eta/s \propto T$ in the QGP phase and f.o. while solid orange line reports the case of the same value of eta/s but with a suddenly kinetic f.o. when the local energy density is $\epsilon < \epsilon_{f.o.}$ (see the text for details). Right panel: experimental v_n vs n for central $Pb + Pb$ collision (black points) compared to hydro calculations for different models as presented in [106].

we note that the reduction due to the different $\eta/s(T)$ is of about 12% in the case of $b = 7\,fm$ while becomes 25% for $b = 0\,fm$. This behavior increase with the n: for v_4 we have a reduction of about 20% in central collision instead of 9% for mid peripheral ones while for v_5 we have 30% instead of 12%.

Finally, in left panel of fig. 5.10 we report the avaraged $\langle v_n \rangle$ corresponding to the $v_n(p_T)$ of fig. 5.8 as a function of the n-order for $Pb+Pb$ collisions at LHC energy and for $0-5\%$ of centrality class. In this figure, solid black line refers to the case of $4\pi\eta/s = 1$ in QGP phase and f.o. while dot dashed lines for $\eta/s \propto T$ in the QGP phase and f.o.. Moreover in order to investigate the effect of the kinetic f.o. on the $\langle v_n \rangle$ we show with the solid orange line the results for the case of a different implementation of the kinetic f.o.. In particular we have considered a *suddenly f.o.*, i.e. when the local energy density $\epsilon < \epsilon_{f.o.} = 0.3\,GeV/fm^3$ we impose that the total cross section drop instantly to the zero value. The value of $\epsilon_{f.o.}$ is choosen in order to correspond to the value of the critical

temperature. This type of f.o. is more similar to the one implemented in hydrodynamics where the f.o. is just a cut in the evolution when the local temperature of the fluid reaches $T_{f.o.} \approx 120\, MeV$. As we have seen the η/s of the QGP phase reduces the value of $\langle v_n \rangle$. As shown in fig. 5.8 comparing the black solid and black dashed lines we found a peak of $\langle v_n \rangle$ for $n = 3$. This result is in agreement with the recent experimental results obtained at LHC [107]. In general we observe that the effect of $\eta/s \propto T$ is to reduce the value of $\langle v_n \rangle$. However it is worth to note that a peak at $n = 3$ remains and moreover the relative strength of v_2 and v_3 is closer to the experimental data when $\eta/s \approx T$ that should represent a more realistic case. This behavior is particularly interesting because viscous hydrodynamics predicts a $v_2 > v_3$ (as shown in left panel of fig. 5.10). We find out that a main reason for such a different ordering may reside on the way the f.o. is realized. Comparing the solid black and orange lines we have that in the case with the suddenly f.o. we obtain that $\langle v_n \rangle$ becomes a decreasing function with respect to n and in this way we obtain similar result to what has been obtained in viscous hydrodynamical calculation where is not possible to include a smooth realization of the kinetic freeze out. These hydrodynamical results are shown in the right panel of fig 5.10 where different blue and green bands correspond to different hydrodynamical approaches as shown in [106], the black points are the experimental data (yellow boxes represent the statistical error bars) taken by CMS collaboration [106].

5.4 Correlations between v_n and ϵ_n

In the recent years, the correlation between integrated v_2 and high order harmonics v_3, v_4 with the initial asymmetry in coordinate space ϵ_2, ϵ_3 and ϵ_4 have been studied [108–110]. In general it has been shown that the elliptic flow is strongly correlated with the initial eccentricity while a weaker correlation has been found for higher harmonics v_3, v_4

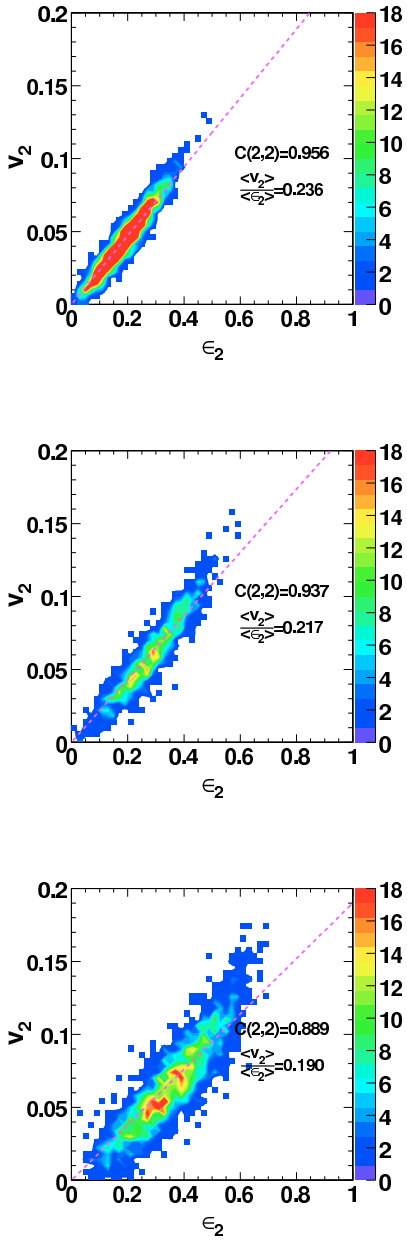

Figure 5.11: ϵ_2 and v_2 for $Au + Au$ collisions at $\sqrt{s_{NN}} = 200\,GeV$ and for three different centrality class from up to down: $(10-20)\%$, $(20-30)\%$ and $(30-40)\%$ respectively.

with ϵ_3 and ϵ_4.

One explanation for the weak correlation observed between v_4 and ϵ_4 is that for final v_4 there is also a correlation with the initial ϵ_2. In particular in [110] it has been shown that it is possible to have a good linear correlation between v_4 and a linear combination of the initial ϵ_2 and ϵ_4.

In this section we discuss these correlations within an event by event transport approach with initial state fluctuation. As first we discuss the change of the degree of correlation between the initial ϵ_n and the final v_n with the centrality of the collision and collision energy. Finally, we discuss the role of the η/s ratio and the effect of the kinetic f.o. on the correlation between ϵ_n and v_n.

A measure of the linear correlation is given by the correlation coefficient $C(n,m)$ given by the following expression:

$$C(n,m) = \frac{\sum_i (\epsilon_n^i - \langle \epsilon_n \rangle)(v_m^i - \langle v_m \rangle)}{\sqrt{\sum_i (\epsilon_n^i - \langle \epsilon_n \rangle)^2 \sum_i (v_m^i - \langle v_m \rangle)^2}} \tag{5.3}$$

where ϵ_n^i and v_m^i are the values of ϵ_n and v_m corresponding to the given event i. $C(n,m) \approx 1$ corresponds to a strong linear correlation between the initial ϵ_n and the final v_m.

The results shown in this section have been obtained with $N_{event} = 1000$ events for each centrality class. In figure 5.11, it is shown the two-dimensional plots of the integrated flow coefficients v_2 as a function of the corresponding initial ϵ_2 for each event. The results shown are for $Au + Au$ collisions at $\sqrt{s_{NN}} = 200\,GeV$ and for three different centralities $(10-20)\%$, $(20-30)\%$ and $(30-40)\%$. The viscosity has been fixed to $4\pi\eta/s = 1$ plus the kinetic f.o. below the transition. One can observe a strong linear correlation between ϵ_2 and v_2 for mid central collisions with a linear correlation coefficient that shows a monotonic behaviour with the collision centrality from $C(2,2) \approx 0.96$ for $(10-20)\%$ to $C(2,2) \approx 0.89$ for $(30-40)\%$. Qualitatively the results are in agreement with the one

obtained within a 2+1D viscous hydrodynamics, see [108]. In general we observe a smaller degree of correlation: the main difference is that we simulate a 3+1D expansion that can give a contribution to the uncorrelation but also the increase of $\eta/s(T)$ for $T < 1.3T_C$. Neverthless the value of $C(2,2)$ is only marginally different with respect to 2+1D viscous hydrodynamics especially for more central conllisions.

In the left and right panels of fig. 5.12 we have shown similar plots for the third and fourth harmonics, respectively. We observe again a reduction of the correlation coefficient with the centrality of the collision similarly to v_2 and ϵ_2. We obtain that the correlation between ϵ_3 and v_3 for all the collision centralities is weaker with respect to that obtained for the elliptic flow. Furthermore for the fourth harmonic flow v_4 we observe essentially a luck of linear correlation with the initial ϵ_4 also for mid peripheral collisions as shown by a correlation coefficient close to the zero value, $C(4,4) \approx 0.45 - 0.03$. Furthermore we observe that the $\langle v_n \rangle / \epsilon_n$ ratio decrease when decrease the correlation coefficient $C(n,n)$ which happens for more peripheral collisions.

A similar behaviour of the coefficient $C(n,n)$ we observe at LHC energies for $Pb + Pb$ collisions at $\sqrt{s_{NN}} = 2.76\, TeV$. In fig. 5.13 it is shown the coefficient $C(n,n)$ as a function of the impact parameter for both RHIC (solid lines) and LHC (dashed lines) energies. As shown the correlation coefficient is a decreasing function of the impact parameter for all the harmonics and for the two different collision energies considered. However we note that the comparison between the dashed and solid lines show that at LHC energies we get a stronger correlation between ϵ_n and v_n for all n respect to RHIC energies. Indeed for most central collisions $C(n,n)$ remains above 0.95 for all $n = 2, 3, 4$, as shown in the comparison of fig. 5.14.

Furthermore we observe that v_2 and ϵ_2 have the same degree of correlation for both RHIC and LHC energies. Instead a lower degree of

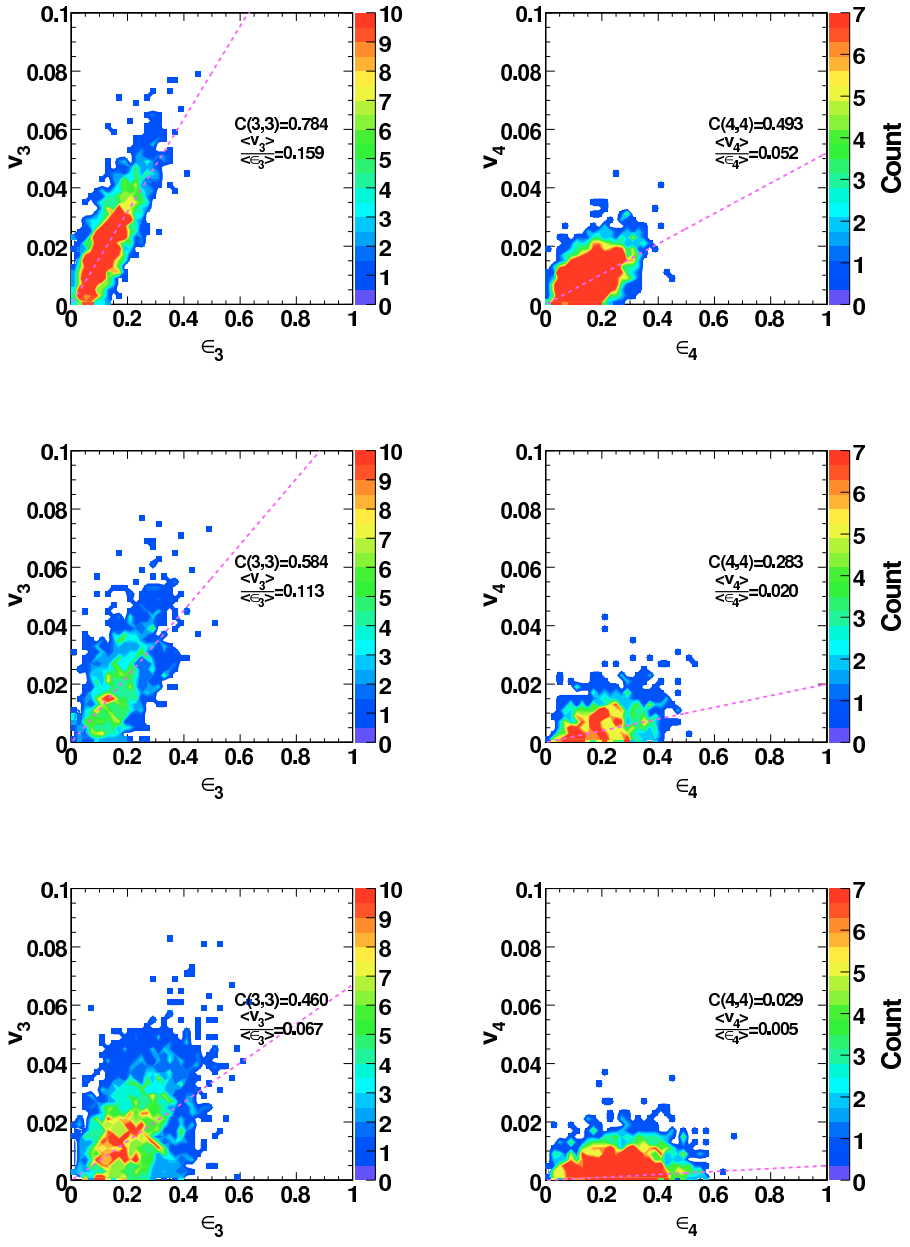

Figure 5.12: In the left panels are shown the correlations plots between ϵ_3 and v_3 for $Au+Au$ collisions at $\sqrt{s_{NN}} = 200\,GeV$ and for three different centrality class from up to down: (10−20)%, (20−30)% and (30−40)% respectively. Similar plots are reported in the right panels for ϵ_4 and v_4.

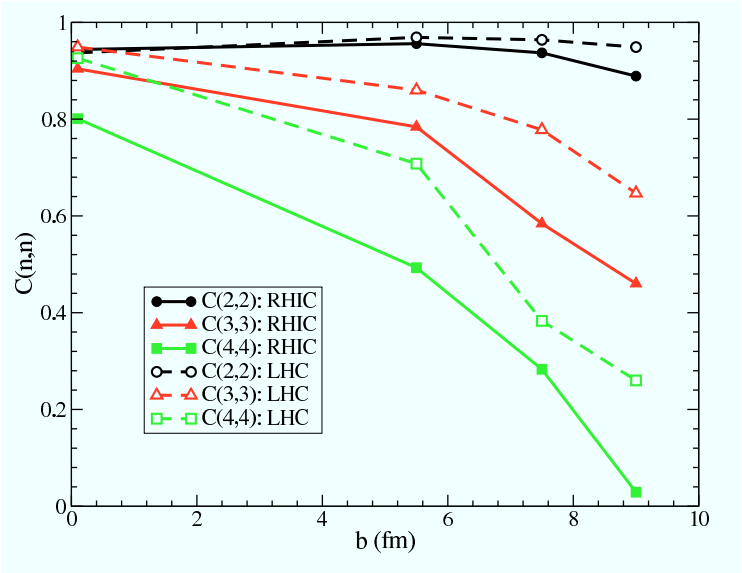

Figure 5.13: Correlation coefficient $C(n,n)$ as a function of the impact parameter b. Different symbols refer to different harmonics n. in particular circles, triangles and squares refer to $n = 2, 3$ and 4 respectively. The solid lines correspond to $Au+Au$ collisions at $\sqrt{s_{NN}} = 200\,GeV$ while dashed lines to the system $Pb+Pb$ at $\sqrt{s_{NN}} = 2.76\,TeV$.

correlation it is shown for higher harmonics $n = 3$ and $n = 4$ at RHIC especially for non-central collisions.

According to these results for central and mid peripheral collisions the $\langle v_2 \rangle$ gives a direct information about the initial eccentricities of the fireball. Furthermore this explains the strong dependence of $\langle v_2 \rangle$ with the collision centralities observed in the experiments at LHC against an almost flat behaviour observed for $\langle v_3 \rangle$ and $\langle v_4 \rangle$.

Moreover the strong correlation observed for central collisions means that the value obtained for $\langle v_n \rangle$ and its dependence with the harmonics n for those collisions is strongly related to the value of the initial ϵ_n. In particular this could imply that the structure of the $v_n(p_T)$ at LHC where $C(n,n) \approx 1$ carry out informations about the geometry of the fluctuations. This joined to the observation that for ultra-central collisions the sensitivity of v_n to η/s is increased by about a factor of two suggest to focus the experimental efforts at LHC highest energy and ultra-central

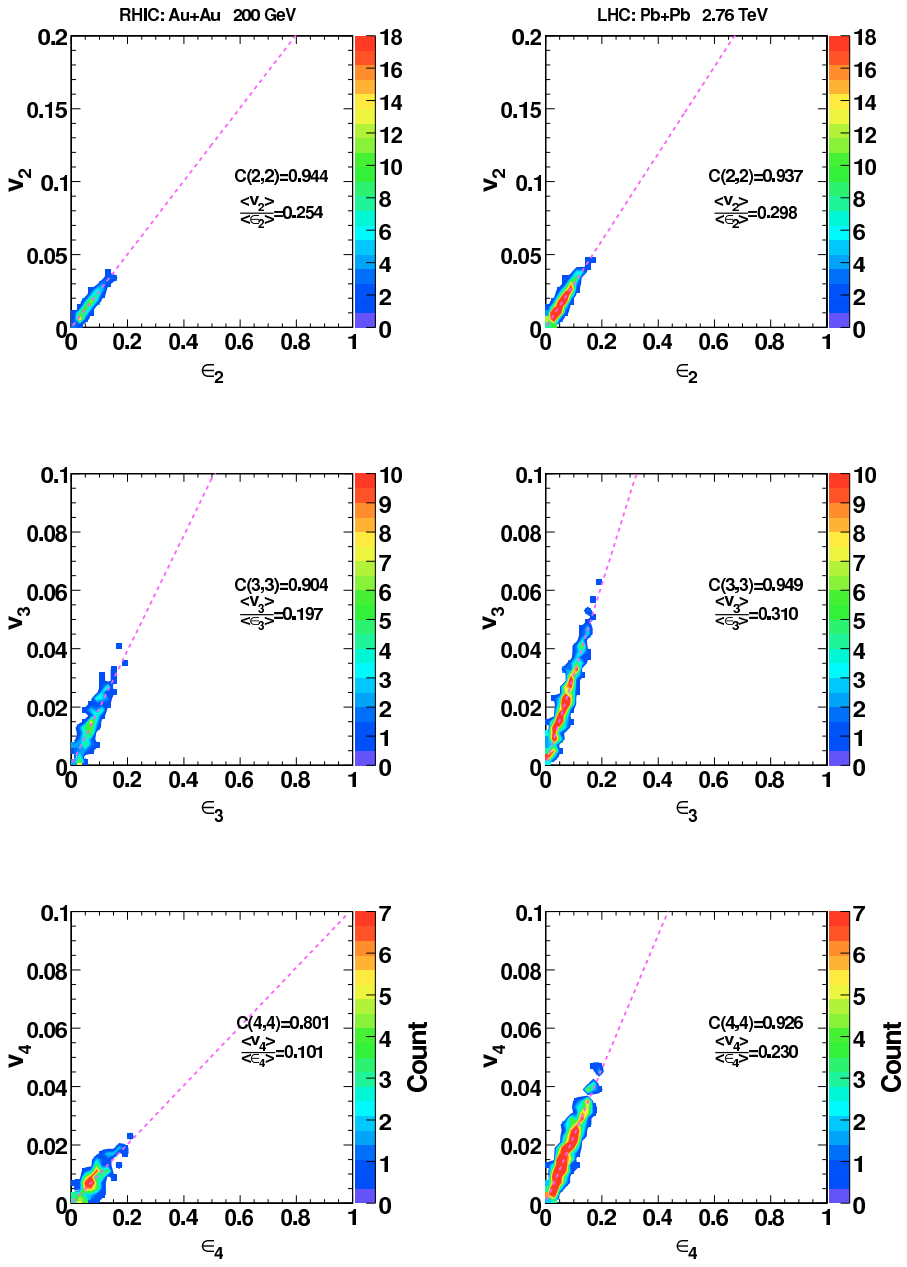

Figure 5.14: Cpmparison between the correlation plots v_n vs ϵ_n for ultra central collisions at different energies (RHIC in the left panels and LHC in the right ones) and for all $n = 2, 3, 4$ (from up to down, respectively).

Table 5.2: Linear correlation coefficient $C(n,n)$ for RHIC and LHC energies and for different temperature parametritazion of η/s. These results are for $(20-30)\%$ centrality class.

$C(n,n)$	n	$4\pi\eta/s = 1$	$4\pi\eta/s = 1$ + f.o.	$\eta/s \propto T$ + f.o.
RHIC	2	0.95	0.94	0.93
	3	0.70	0.58	0.65
	4	0.30	0.28	0.31
LHC	2	0.96	0.96	0.96
	3	0.78	0.78	0.74
	4	0.39	0.38	0.38

collisions.

In order to study the effect of the viscosity and its possible temperature dependence on the correlation we have studied how change the correlation coefficient with the different parametrizations for η/s. In Table 5.2 we show the results for $C(n,n)$ for the two energies RHIC and LHC for $(20-30)\%$ centrality class. In general for this centrality we observe that at LHC energies and for all the viscosities considered the degree of correlation between ϵ_n and v_n is greater than the one at RHIC energies. Moreover we obtain that in general the correlation coefficient is not sensitive to the change of the viscosity both at low and high temperature. An exception is found at RHIC energies for v_3 where the effect of the kinetic freeze out is to reduce the degree of correlation between the initial ϵ_n and the final v_n.

CONCLUSIONS

This thesis is focused on the study of the build up of the anisotropic collective flow created in ultra relativistic heavy ion collisions. Indeed the production of elliptic flow v_2 and high order harmonics v_n is one of the strongest evidence of the formation of a thermalized dense state of matter strongly interacting and at very high pressure ($P \approx 100\, Mev/fm^3$) and temperature ($T \approx 200\, MeV = 10^{12}\, K$): the Quark Gluon Plasma.
In the first part of this work we presented the main features of the QGP and the characteristics of the QCD phase diagram. We considered that the QGP is also present in the Early Universe and we have studied the possible impact of such a phase transition. With this aim we determined the precise time evolution of the thermodynamic parameters of the early Universe by solving the Friedmann equation for a realistic equation of state (EoS) coming from the heavy ion collision and lattice QCD data of Wuppertal-Budapest. A comparison with the result obtained with simple bag model EoS was made. We also included for a realistic EoS the impact of a strong primordial magnetic field.
The realistic equation of state describes a crossover rather than the first-order phase transition between the quark-gluon plasma and hadronic matter. Our numerical calculations of the energy density fluctuations

show that small inhomogeneities of strongly interacting matter in the early Universe are moderately damped during the crossover transition. This implies that there are small chances of inhomogeneities phenomena during the Big Bang nucleosynthesis.

In the second part of the thesis is described a primer of the collision dynamics in the ultra-relativistic heavy-ion reactions with a particular accent on the two beam energies of our interest for the successive analisys: RHIC for $Au + Au$ at $\sqrt{s} = 200\,GeV$ and LHC for $Pb + Pb$ at $\sqrt{s} = 2.76\,TeV$.

The principal probes of the formation of the QGP state were also described. In particular, in this work we focus the attention to the strong anisotropic collective flow measured in both central and non-central collision events. It has been presented the experimental problems, definitions and methods developed to study the anisotropies in the azimuthal distribution. Moreover, we pointed out that elliptic flow and high order harmonics are observables sensitive to the shear viscosity η/s. Furthermore, we reported the status of the art for both the experimental data and the hydrodynamic approach.

The aim of this work was to employ a Boltzmann-like transport code in order to study this anisotropic flows taking advantage from the use of a microscopic approach. So that, we have described the principal features of the kinetic theory and we have developed a code in which it is possible to estimate the viscosity of the plasma in a wider range of η/s and p_T. Moreover, in order to investigate the evolution of the initial collision geometry fluctuations we have implemented in the code an initial profile that changes event-by-event using a Monte-Carlo Glauber model.

As a first step we have tested the right computation of initial density and temperature fluctuations comparing with the analitical calculation of the density function. Moreover, for both the energy of our interest we were able to reproduce the initial fluctuating transverse density and local

temperature expected in a $Au + Au$ or $Pb + Pb$ collision.
Furthermore, with a fixed density profile calculated with the fluctuating Monte-Carlo Glauber approach, we have tested the convergency of our results for v_n with the lattice spacing grid and N_{test}. We have found the good compromise between the convergency and the computational time for $A_T = 0.12 fm^2$ of transverse area and $N_{test} = 2 \cdot 10^6$ total number of test particles.
The analysis of our results with the fluctuating method in comparison with the standard Glauber model indicate that the most important effect in the introduction of the event by event approach is in the evolution of the differential flow coefficients. More precisely the final spectra calculated for the two different approach are very similar in the transverse momentum range of our interest ($p_T \leq 3 GeV$) while the elliptic flow $v_2(p_T)$ shows a reduction of about 20% as a conseguence of the fluctuation in the initial geometry.
On the contrary, the introduction of fluctuations in r-space in the transverse plane generates the higher order harmonics and in particular the odd harmonics which were absent by symmetry in the averaged initial configuration. This effect was confirmed by our calculations in which we have observed an increasing in the final $v_4(p_T)$ of about 60% for the case with event by event fluctuations.
The main purpose of this work of thesis was to study the effect of the shear viscosity in the evolution of the differential flow coefficients $v_n(p_T)$ because of their sensibility to this quantity. In particular, we had been computed our code for three different cases of η/s: one with a constant $4\pi\eta/s = 1$ during all the evolution of the system; another one with $4\pi\eta/s = 1$ in the QGP phase and an increasing η/s in the cross over region towards the estimated value for hadronic matter $4\pi\eta/s \approx 6$ and the third one with an increase of η/s at higher temperature with a linear dependence and a minimum close to the critical temperature.

In this way we have found that at RHIC for $Au + Au$ at $\sqrt{s} = 200\,GeV$ the $v_n(p_T)$ are more sensitive to the value of η/s at low temperature and in particular this sensitivity increase with the order of the harmonics. At LHC for $Pb + Pb$ at $\sqrt{s} = 2.76\,TeV$ we get a different effect, the $v_n(p_T)$ are not so sensitive to the increase of η/s in the cross over region of the transition. More precisely, the difference sensitivity can be due to the different formation time of each harmonics amd this involve at RHIC a reduction of the elliptic flow of about 17%, 25% for the third harmonic and of about 30% in case of $v_4(p_T)$. At LHC, this reduction is negligible for elliptic flow and for $v_3(p_T)$ while is only about 10% for the fourth harmonic.

Finally we have also studied the correlation between v_n and ϵ_n for $n = 2, 3$ and 4. We have shown that the second and third harmonic flows are correlated to their initial eccentricities, a result similar to that has been obtained in the recent years in viscous hydrodynamics.

We have however pointed out that in ultra-central collision at LHC energy the correlation between v_n and ϵ_n stays above 0.9 (90%) for all the harmonics ($n = 2, 3, 4$) at variance with RHIC energy and more generally with respect to non central collision. Moreover we have found that the sensitivity of $v_n(p_T)$ to $\eta/s(T)$ is increased by a factor of two in ultra-central collisions. In addiction, studing the avaraged $\langle v_n \rangle$ as a function of n-order we pointed out that the inclusion of a realistic smooth freeze out in our simulation code leads to the presence of a peak in correspondence of $n = 3$ in agreement to the experimental results. This particular result is in contrast to what has been obtained in viscous hydrodynamical calculation where is not possible to include such a kinetic freeze out.

The results of our work can be a starting point for further investigations. In fact the transverse momentum spectra and the differential flow coefficients $v_n(p_T)$ calculated with the event by event fluctuation approach improved in this work can be implemented in a model based on a quark

coalescence mechanism in order to study the effect of hadronization and to compare the final result with experimental data.

ACKNOWLEDGEMENTS

Concluding my Ph.D. course there are many people that I would like to thank for giving me, in different ways, the support and the guidance necessary to go on in these years and to complete this work.
My first thanks goes to my tutor, Prof. Vincenzo Greco, that has guided and continuously supported me in these stimulating and for me new field of physics. Billions of thanks to Dr. Salvatore Plumari for his endless help and support and for having been close to me every day during this work. Special thank to Dr. Marco Ruggieri for the stimulating discussion and the useful suggestions. I would like to thank also the other members of my research group: Dr. Francesco Scardina, Dr. Armando Puglisi, Dr. Vincenzo Minissale and Dr. Lucia Oliva.
Particular and reserved thanks to Dr. Iolanda Indelicato and Dr. Mariangela Bondì who shared with me this journey. Special thanks also to Dr. Roberta Spartà, Dr. Diana Carbone, Dr. Giuseppe D'Agata for the pleasant time we spent together in our incubator office. Finally I want to thank all the people of the Laboratori Nazionali del Sud who helped me in different ways in these years: Prof. Claudio Spitaleri and all the people of AsFiN group especially Dr. Livio Lamia and Dr. Marco La Cognata.

There are many other people who were close to me throughout these years. The biggest thanks goes to my parents for all the love they give me every day and to my brother Roberto.
The most unique and lovely thank goes to my adored architect Marilena Lanzafame for always supporting me.
Last but not least I also thank all my friends who have always been close to me: Chiara, Billy, Rossella, Simone, Elisa, Michele, Giulia, Fabrizio, the "Bbelli", Martino and the other guys that I forget in this moment but not in my heart.

BIBLIOGRAPHY

[1] K. Nakamura et al., J.Phys. **G37**, 075021 (2010).

[2] Y. Nambu, *Preludes in Theoretical Physics in Honor of V. F. Weisskopf, ed. by A. De-Shalit, H. Feshbach, and L. Van Hove* (North-Hollan, Amsterdam, 1966).

[3] Chen-Ning Yang and Robert L. Mills, Phys.Rev. **96**, 191 (1954).

[4] D.J. Gross and Frank Wilczek, Phys.Rev. **D8**, 3633 (1973).

[5] H. David Politzer, Phys.Rev.Lett. **30**, 1346 (1973).

[6] Kenneth G. Wilson, Phys.Rev. **D10**, 2445 (1974).

[7] M. Herrero, arXiv **hep-ph/9812242**, (1998).

[8] K. Yagi, T. Hatsuda, and Y. Miake, *Quark-Gluon Plasma, From Big Bang to Little Bang* (Cambridge University Press, Cambridge, 2005).

[9] Sidney R. Coleman and David J. Gross, Phys.Rev.Lett. **31**, 851 (1973).

[10] Yoichiro Nambu and G. Jona-Lasinio, Phys.Rev. **122**, 345 (1961).

[11] M. E. Peskin and D. V. Schroeder, *An Introduction to Quantum Field Theory* (Addison-Wesley, Redwood City, 1995).

[12] Alfred H. Mueller, Phys.Rept. **73**, 237 (1981).

[13] John C. Collins, Davison E. Soper, and George F. Sterman, Nucl.Phys. **B261**, 104 (1985).

[14] V.N. Gribov and L.N. Lipatov, Sov.J.Nucl.Phys. **15**, 438 (1972).

[15] Yuri L. Dokshitzer, Sov.Phys.JETP **46**, 641 (1977).

[16] Guido Altarelli and G. Parisi, Nucl.Phys. **B126**, 298 (1977).

[17] A. Chodos, R.L. Jaffe, K. Johnson, Charles B. Thorn, and V.F. Weisskopf, Phys.Rev. **D9**, 3471 (1974).

[18] Cheuk-Yin Wong, *Introduction to High-Energy Heavy-Ion Collisions* (World Scientific, Singapore, 1994).

[19] Frithjof Karsch, Lect.Notes Phys. **583**, 209 (2002).

[20] Ulrich W. Heinz, 165 (2004).

[21] John B. Kogut and Leonard Susskind, Phys.Rev. **D11**, 395 (1975).

[22] David B. Kaplan, Phys.Lett. **B288**, 342 (1992).

[23] Szabolcs Borsanyi, Gergely Endrodi, Zoltan Fodor, Antal Jakovac, Sandor D. Katz, et al., JHEP **1011**, 077 (2010).

[24] A. Friedman, Z.Phys. **10**, 377 (1922).

[25] Edwin Hubble, Proc.Nat.Acad.Sci. **15**, 168 (1929).

[26] J.H. Applegate, C.J. Hogan, and R.J. Scherrer, Ap.J. **329**, 572 (1988).

[27] Toshitaka Kajino, Nucl.Phys. **A588**, 339c (1995).

[28] Leonardo Campanelli, Phys.Rev.Lett. **111**, 061301 (2013).

[29] T. Vachaspati, Phys.Lett. **B265**, 258 (1991).

[30] Raoul Gatto and Marco Ruggieri, Phys.Rev. **D83**, 034016 (2011).

[31] G.S. Bali, F. Bruckmann, G. Endrodi, Z. Fodor, S.D. Katz, et al., JHEP **1202**, 044 (2012).

[32] Jingyi Chao, Pengcheng Chu, and Mei Huang, Phys.Rev. **D88**, 054009 (2013).

[33] Toru Kojo and Nan Su, Phys.Lett. **B720**, 192 (2013).

[34] Christoph Schmid, Dominik J. Schwarz, and Peter Widerin, Phys.Rev.Lett. **78**, 791 (1997).

[35] Christoph Schmid, Dominik J. Schwarz, and Peter Widerin, Phys.Rev. **D59**, 043517 (1999).

[36] Wojciech Florkowski, Nucl.Phys. **A853**, 173 (2011).

[37] A. Hewish, S.J. Bell, J.D.H Pilkington, P.F. Scott, and R.A. Collins, Nature **217**, 709 (1968).

[38] J.R. Oppenheimer and G.M. Volkoff, Phys.Rev. **55**, 374 (1939).

[39] Torleif Erik Oskar Ericson, M. Jacob, H. Satz, and W. Willis, (1982).

[40] John W. Harris and Berndt Muller, Ann.Rev.Nucl.Part.Sci. **46**, 71 (1996).

[41] I. Arsene et al., Nucl.Phys. **A757**, 1 (2005).

[42] B.B. Back, M.D. Baker, M. Ballintijn, D.S. Barton, B. Becker, et al., Nucl.Phys. **A757**, 28 (2005).

[43] John Adams et al., Nucl.Phys. **A757**, 102 (2005).

[44] K. Adcox et al., Nucl.Phys. **A757**, 184 (2005).

[45] J.D. Bjorken, Lect.Notes Phys. **56**, 93 (1976).

[46] Ren-Chuan Wang and Cheuk-Yin Wong, Phys.Rev. **D44**, 679 (1991).

[47] Michael L. Miller, Klaus Reygers, Stephen J. Sanders, and Peter Steinberg, Ann.Rev.Nucl.Part.Sci. **57**, 205 (2007).

[48] C.Y. Wong, (1995).

[49] Zhe Xu and Carsten Greiner, Eur.Phys.J. **A29**, 33 (2006).

[50] F. Scardina, M. Colonna, S. Plumari, and V. Greco, Phys.Lett. **B724**, 296 (2013).

[51] V. Greco, C.M. Ko, and P. Levai, Phys.Rev.Lett. **90**, 202302 (2003).

[52] Johann Rafelski and Berndt Muller, Phys.Rev.Lett. **48**, 1066 (1982).

[53] T. Matsui and H. Satz, Phys.Lett. **B178**, 416 (1986).

[54] B. Alver, B.B. Back, M.D. Baker, M. Ballintijn, D.S. Barton, et al., Phys.Rev. **C77**, 014906 (2008).

[55] J. Adams et al., Phys.Rev. **C72**, 014904 (2005).

[56] Peter F. Kolb, Josef Sollfrank, and Ulrich W. Heinz, Phys.Rev. **C62**, 054909 (2000).

[57] Raimond Snellings, New J.Phys. **13**, 055008 (2011).

[58] S. Voloshin and Y. Zhang, Z.Phys. **C70**, 665 (1996).

[59] Rajeev S. Bhalerao and Jean-Yves Ollitrault, Phys.Lett. **B641**, 260 (2006).

[60] Mike Miller and Raimond Snellings, (2003).

[61] H. Sorge, Phys.Rev.Lett. **82**, 2048 (1999).

[62] J. Barrette et al., Phys.Rev. **C55**, 1420 (1997).

[63] Nicolas Borghini, Phuong Mai Dinh, and Jean-Yves Ollitrault, Phys.Rev. **C63**, 054906 (2001).

[64] Paul Romatschke and Ulrike Romatschke, Phys.Rev.Lett. **99**, 172301 (2007).

[65] P. Kovtun, Dan T. Son, and Andrei O. Starinets, Phys.Rev.Lett. **94**, 111601 (2005).

[66] Laszlo P. Csernai, Joseph.I. Kapusta, and Larry D. McLerran, Phys.Rev.Lett. **97**, 152303 (2006).

[67] Roy A. Lacey, N.N. Ajitanand, J.M. Alexander, P. Chung, W.G. Holzmann, et al., Phys.Rev.Lett. **98**, 092301 (2007).

[68] Salvatore Plumari, Wanda M. Alberico, Vincenzo Greco, and Claudia Ratti, Phys.Rev. **D84**, 094004 (2011).

[69] Peter Brockway Arnold, Guy D Moore, and Laurence G. Yaffe, JHEP **0305**, 051 (2003).

[70] Madappa Prakash, Manju Prakash, R. Venugopalan, and G. Welke, Phys.Rept. **227**, 321 (1993).

[71] Jiunn-Wei Chen, Yen-Han Li, Yen-Fu Liu, and Eiji Nakano, Phys.Rev. **D76**, 114011 (2007).

[72] Harvey B. Meyer, Phys.Rev. **D76**, 101701 (2007).

[73] Santosh K Das and Jan-e Alam, Phys.Rev. **D83**, 114011 (2011).

[74] Bjorn Schenke, Sangyong Jeon, and Charles Gale, Phys.Rev. **C85**, 024901 (2012).

[75] Charles Gale, Sangyong Jeon, Bjorn Schenke, Prithwish Tribedy, and Raju Venugopalan, Phys.Rev.Lett. **110**, 012302 (2013).

[76] Kerson Huang, *Statistical Mechanics* (John Wiley and Sons, New York, 1987).

[77] Laszlo P. Csernai, *Introduction to relativistic heavy ion collisions* (John Wiley and Sons, Hoboken, 2008).

[78] Hans-Thomas Elze, AIP Conf.Proc. **631**, 229 (2002).

[79] Zhe Xu and Carsten Greiner, Phys.Rev. **C71**, 064901 (2005).

[80] M. Gyulassy, H.T. Elze, A. Iwazaki, and D. Vasak, (1986).

[81] D. Vasak, M. Gyulassy, and H.T. Elze, Annals Phys. **173**, 462 (1987).

[82] H.T. Elze, M. Gyulassy, D. Vasak, H. Heinz, Horst Stoecker, et al., Mod.Phys.Lett. **A2**, 451 (1987).

[83] S. R. de Groot, W. A. van Leeuwen, and C. G. van Weert, *Relativistic Kinetic Theory* (North-Holland, Amsterdam, 1980).

[84] Remi Hakim, Riv.Nuovo Cim. **1N6**, 1 (1978).

[85] Bin Zhang, Miklos Gyulassy, and Che Ming Ko, Phys.Lett. **B455**, 45 (1999).

[86] Denes Molnar and Miklos Gyulassy, Nucl.Phys. **A697**, 495 (2002).

[87] G. Ferini, M. Colonna, M. Di Toro, and V. Greco, Phys.Lett. **B670**, 325 (2009).

[88] V. Greco, M. Colonna, M. Di Toro, and G. Ferini, Prog.Part.Nucl.Phys. **62**, 562 (2009).

[89] S. Plumari, V. Baran, M. Di Toro, G. Ferini, and V. Greco, Phys.Lett. **B689**, 18 (2010).

[90] Zhe Xu and Carsten Greiner, Phys.Rev. **C79**, 014904 (2009).

[91] Cheuk-Yin Wong, Phys.Rev. **C25**, 1460 (1982).

[92] G.F. Bertsch and S. Das Gupta, Phys.Rept. **160**, 189 (1988).

[93] W. Cassing, V. Metag, U. Mosel, and K. Niita, Phys.Rept. **188**, 363 (1990).

[94] H. Kruse, B.V. Jacak, and Horst Stoecker, Phys.Rev.Lett. **54**, 289 (1985).

[95] W. Liu and R.J. Fries, Phys.Rev. **C78**, 037902 (2008).

[96] W. Liu and R.J Fries, Phys.Rev. **C77**, 054902 (2008).

[97] P. Danielewicz and G.F. Bertsch, Nucl.Phys. **A533**, 712 (1991).

[98] Salvatore Plumari, Armando Puglisi, Maria Colonna, Francesco Scardina, and Vincenzo Greco, J.Phys.Conf.Ser. **420**, 012029 (2013).

[99] S. Plumari, V. Greco, and L.P. Csernai, (2013).

[100] Burak Han Alver, Clement Gombeaud, Matthew Luzum, and Jean-Yves Ollitrault, Phys.Rev. **C82**, 034913 (2010).

[101] Clement Gombeaud and Jean-Yves Ollitrault, Phys.Rev. **C77**, 054904 (2008).

[102] M. Ruggieri, F. Scardina, S. Plumari, and V. Greco, Phys.Lett. **B727**, 177 (2013).

[103] E. Richardson, PoS **QNP2012**, 146 (2012).

[104] Julia Velkovska, J.Phys. **G38**, 124011 (2011).

[105] Serguei Chatrchyan et al., Phys.Rev. **C89**, 044906 (2014).

[106] CMS Collaboration, (2012).

[107] Georges Aad et al., Phys.Rev. **C86**, 014907 (2012).

[108] H. Niemi, G.S. Denicol, H. Holopainen, and P. Huovinen, Phys.Rev. **C87**, 054901 (2013).

[109] A.K. Chaudhuri, Md. Rihan Haque, Victor Roy, and Bedangadas Mohanty, Phys.Rev. **C87**, 034907 (2013).

[110] Fernando G. Gardim, Frederique Grassi, Matthew Luzum, and Jean-Yves Ollitrault, Phys.Rev. **C85**, 024908 (2012).